THE OBLIQUE IMPACT RESPONSE OF COMPOSITES AND SANDWICH STRUCTURES

Thesis submitted in accordance with the requirement of

The University *of* Liverpool for the degree of

Doctor in Philosophy

by

Siti Hajar Sheikh Md Fadzullah

School of Engineering

October 2014

ACKNOWLEDGEMENTS

In the name of God, Most Beneficial, Most Merciful.

I would like to convey my gratitude to my primary supervisor, Professor Wesley Cantwell for his continuous support, guidance, words of wisdom and trust in me to complete this PhD studies. A special thanks to Dr Graham Schleyer for his feedback and motivations throughout this journey.

My sincere gratitude to members of the School of Engineering, including Mr Stephen Pennington, Mr Jijimon Matthews, Mr Dave Atkinson, Mrs Denise Bain as well as my colleagues including Dr Mohamed Zaki Hassan, Dr Mohd Ruzaimi Mat Rejab, Dr Muhammad Al-Tenaji, Mr Mohd Zuhri Yusoff, Miss Alia Ruzanna and acquaintances from the Malay Speaking Circle Liverpool (MSC Liverpool) for their kind assistance, friendship, care and support. My special thanks to Dr. Olawale F.Ifayefunmi, Dr Zaleha Mustafa, Dr Rafidah Hasan, Dr Massila Kamalrudin and Mrs Ruzy Haryati Hambali for their endless prayers, help, support and words of encouragement throughout the completion of this thesis.

A special dedication to my loving husband, Radin Suparman Joyo, my beloved son, Radin Amir Zikri, my dearest mother, Hamidah Abdul Wahab and my family who have showered me with their unconditional love, sacrifice, support, prayers and motivation throughout this long journey to success.

I would also like to thank the Universiti Teknikal Malaysia Melaka (UTeM) and the Government of Malaysia for sponsoring this PhD studies.

This thesis is dedicated to my late father, Sheikh Md. Fadzullah Sheikh Hassan who had loved, inspired and motivated me to reach this level of greatness in the field of knowledge.

LIST OF PUBLICATIONS

Sheikh Md Fadzullah, S.H., Cantwell, W.J., Damage Repair of Thermoplastic Composites. UK-Malaysia-Ireland Engineering & Science Conference 2010 (UMIES 2010). Queen's University of Belfast, Ireland, UK, 2010.

Sheikh Md Fadzullah, S.H., Cantwell, W.J., The effect of angle of obliquity on the damage characteristics of composite structures. International Conference on Humanities, Social Sciences & Science Technology (ICHSST'11). University of Manchester, UK, 2011.

Sheikh Md Fadzullah, S.H., Cantwell, W.J., The Interlaminar Fracture Properties of Fibre Reinforced Thermoplastic Composites: The Effect of Processing Temperature and Time. Journal of Mechanical Engineering and Technology (JMET). 2011; 3(2):13-25.

Sheikh Md Fadzullah, S.H., Cantwell, W.J., The effect of angle of incidence on the impact response of composites and sandwich structures. 15th European Conference on Composite Materials (ECCM15). Venice, Italy, 2012.

ABSTRACT

This research project focussed on the low-velocity oblique impact response of glass fibre-reinforced epoxy laminates and sandwich structures with a range of polymeric cores of linear PVC and PET with nominal densities in the range of 90-140 kg/m^3, conducted at normal (0°), 10° and 20° inclination angles, at energies up to 40 J. For the laminated composites and the linear PVC sandwich structures, at maximum impact energies, the damage area reduced whilst the energy absorbed increased with increasing inclination angle. Damage took the form of matrix cracking, due to bending and shear, combining with fibre fracture due to tensile loading. In the case of the higher density foam-core sandwich structures (PVC and PET), the maximum damage area occurs at 10° and less severe damage occurs at 20°, suggesting an effect of the combination of tensile, compression and shear occurred at 10°. Interestingly, the absorbed energy reduced with increasing inclination angle for these structures. The threshold energy in which visible damage occurs was observed at 14 J and 10 J for the laminated composites and sandwich structures, respectively. At higher energy levels (40 J), full perforation occurred. Contrary to the observations at relatively low energies, the PET-based sandwich structures showed increased damage with increasing inclination angle. An energy-balance model was established and used to successfully predict the maximum impact force (P_{max}) values, showing good agreement with the experimental results up to the threshold energy. In addition, these findings also showed that core density has a great influence on the impact response of the sandwich structures, whereby the contact stiffness, C, and the maximum impact force (P_{max}), increased with an increase in core density.

NOMENCLATURES

Symbols

t	Impact duration
h_c	Thickness of the core
E	Young's modulus of the composite
ρ	Density of the composite
R_p	Support span
ρ_1	Density of the facesheet
M	Target mass
m	Mass of the indenter
k	Constant stiffness; static force required to produce unit transverse deflection
V_o	Velocity of the indenter immediately before impact
U_o	Energy of the indenter before impact
U_i	Energy of the indenter at time, *t*
U_p	Strain energy stored by the plate at time, *t*
$F,\ P$	Contact force
F_{max}	Maximum load (force)
V	Velocity of the indenter
E_b	Energy absorbed in bending effects
E_s	Energy absorbed in shear effects
E_m	Energy stored due to membrane stiffness
E_c	Energy stored in the contact region during indentation

K_{bs}	Linear stiffness including bending and transverse shear deformation effects
K_m	Membrane stiffness
ω	Overall deformation of the plate (target)
ω_o	Maximum deflection of the plate
α_o	Maximum indentation of the plate
G	Shear modulus of the foam core
L	Span
D	Flexural rigidity of the skins
A	Geometrical parameter that depends on the thickness of the core and skin materials, as well as the beam width.
δ_{max}	Maximum displacement
P_{max}	Maximum contact force
C	Contact stiffness
α	Indentation
E	Young's modulus
E_1	Young's Modulus of the indenter
E_2	Young's Modulus of the target
R	Radius of the indenter
v	Poisson's ratio
δ	Displacement
n	Indentation exponent
P_{crit}	The critical impact load or threshold value
t	Laminate thickness
E	Flexural modulus

G_{IIc}	Critical value of the energy release rate for Mode II fracture
P_f	Indentation load at shear failure
K_c	Constraint factor
F_f	Maximum impact force
τ_{13d}	Dynamic transverse shear strength of the facesheet
q_d	Dynamic crushing strength
ε_{cr}	Tensile fracture strain
N_{cr}	Membrane fracture force
P_f	Damage initiation load for a circumferential crack
d	Damage length
R_e	Indenter radius of curvature
γ_f	Transverse shear fracture strain
G_{13}	Transverse shear modulus of the honeycomb
E_I	Imparted energy
V_S	Striking velocity
V_R	Rebound velocity
U_R	Strain energy due to the deflection of the guide rods
K	Transverse stiffness of the indenter and the guide rod assembly
F_H	Horizontal force in the guide rod assembly
F_N	Normal or reaction force
F_s	Striking force (measured by the force transducer during an impact test)
θ	Plate inclination angle
k	Indenter unit stiffness in horizontal direction

δx	Displacement in horizontal direction
F_T	Friction or tangential force
μ	Coefficient of friction
r	Radius of the right cylinder
R	Long radius of the elliptical oblique cylinder
I	Angle between the right cylinder and the elliptical oblique cylinder
D	Diameter of the damage

Abbreviations

SDOF	Single-degree of freedom
TDOF	Two degree of freedom
ILSS	Interlaminar shear strength
CSM	Chopped strand mat
ACG	Advanced Composites Group
UD	unidirectional
PVC	poly (vinyl chloride)
PET	poly (ethylene terephthalate)
BVID	barely visible impact damage

TABLE OF CONTENTS

LIST OF FIGURES

LIST OF TABLES

CHAPTER I: INTRODUCTION

This chapter gives a brief introduction to fibre reinforced polymer (FRP) composites and sandwich structures, together with some examples of their applications. In addition, the motivation for the study, the research scope, the aims and objectives of the study, as well as the thesis organization are also presented in this chapter.

1.0 Background

For more than fifty years, there has been a growing increase in the use of composites and sandwich structures in a wide range of applications. This includes aerospace, automotive, medical, construction, marine, domestic use as well as many other applications. This is associated with a continuing drive for improved performance; which includes lower weight, superior strength as well as low cost. An example of the significant contribution of the composites industry in the UK market in 2010 are illustrated in Tables 1.1 and 1.2, which show that the UK produces about £1.1 billion of composite components and structures, with the aerospace sector being the biggest user of composites and the principal driver of high value carbon fibre composites. In Figure 1.1, the next generation of military transport aircraft by Airbus, the A400M, is shown. Importantly, the wings of this aircraft are made of carbon fibre composites. It is anticipated that by using composites rather than metals, the overall strength to weight ratio of the structures used in the design of the aircraft will be improved by up to 20%.

With the continuous increase in the use of these materials, there is a growing concern regarding their impact resistance, since it is well-known that these materials exhibit a

poor resistance to transverse loading, such as that associated with impact. The majority of studies in this area have focused on normal impact, whilst in operational service; impact is often at an oblique angle. An example is a tool dropped on an aerospace component, hail damage or even a bird strike. Such scenarios can clearly involve a range of velocities and various types of target material. Therefore, this research aims to study the oblique impact response of composites and sandwich structures with a particular focus on low-velocity impact, a topic for which there remains very little information in the open literature. Much of the published work on oblique impact focuses on ballistic impact, undertaken at velocities up to a few km per second.

Table 1.1 UK production of composites by material, 2010 estimates [1].

Materials	**Metal matrix**	**Glass fibre**	**Carbon fibre**
Production value (£ million)	3	453	658
Production volume (tonnes)	35 t	87 kt	2.5 kt

Table 1.2 UK production of composites by sector, 2010 estimates [1].

Sector	**Marine, construction, other**	**Automotive**	**Aerospace**
Production (£ million)	374	63	675
Production volume (tonnes)	69 kt	9 kt	0.8 kt

Figure 1.1 Photograph of the Airbus A400M, the next generation of military aircraft [2].

1.1 Typical applications of fibre reinforced polymer (FRP) and sandwich structures

Composites and sandwich structures are finding increasing use in a wide spectrum of applications, including aerospace, automotive, civil engineering, marine as well as wind turbine blades, an important source of renewable energy generation. These include both structural and non-structural applications.

As an example, in the ship building industry, composite and sandwich structures, commonly based on glass and carbon composites structures have been used extensively over the past 25 years. In Table 1.3, the variables for the different materials and designs that are commonly assessed in the conceptual phase of sandwich structures for a naval ship are given.

The 72-metre Visby class corvette in Figure 1.2 is the largest and most advanced composite naval vessel or ship built so far. This massive superstructure is fabricated using stitched carbon fibre vinyl ester sandwich panels with a Divinycell core and glass fibre composites in other parts [3].

Figure 1.2 A side view of the Swedish 72-metre long Visby Class or YS 2000 corvette [4].

Table 1.3 Typical variables for materials in sandwich designs of naval ships [4].

Materials/design	**Variables or variants**
Core material	PVC, PEI, PMI, Balsa, etc. Density, thickness, temperature resistance, strength, stiffness, etc.
Resin, matrix	Epoxy, vinyl ester, polyester Viscosity, strength, stiffness, cure cycle, temperature resistance, etc.
Fibre	E-glass, aramid, carbon Modulus, ultimate strain, number of filaments, etc.
Reinforcement	Type of reinforcement (woven, non-crimp, random, combinations of different types) Surface weight, fibre orientations, etc.
Structural putty	Epoxy, polyester, polyurethane Viscosity, ultimate strain, cure cycle, temperature resistance, etc.
Laminate	Combination of matrix, fibre, reinforcement, reinforcement stacking, production method, etc.
Sandwich	Combination of laminate, core material, production method, etc.

Some of the main reasons for using composites and sandwich structures in the Visby Class Corvettes are [4]:-

- High stiffness and strength-to-weight ratio, therefore a lightweight design is possible.
- Good resistance to underwater explosions, such as mines.
- Built-in noise and vibration damping, giving a low hydro-acoustic signature.
- Low maintenance costs due to absence of corrosion (non-metallic).
- Less fuel consumption due to low structural weight, giving a low pressure signature in the water.
- Cost-efficient structure with the built-in thermal insulation.

Composite materials are becoming key elements in the development of rotor blades in the wind turbine industry, since they offer features, such as a low density, a high stiffness as well as potentially long lifetimes. In Figure 1.3, the shape of a rotor blade is illustrated, in which the aerodynamic contours are formed using relatively thin shells, supported by a longitudinal bream or webs. The beam carries a substantial part of the load on a blade, whereas in the longitudinal direction, the rotor blades are tapered and twisted [5]. In Figure 1.4, an example of a local wind farm in Liverpool Bay, United Kingdom is shown.

Figure 1.3 Cross-section of a rotor blade giving the nomenclature of the different elements of the blades [5].

This text box is where the unabridged thesis included the following third party copyright material:

http://www.thesundaytimes.co.uk/sto/news/uk_news/Environment/ article991336.ece Accessed on 27th August 2014.

Figure 1.4 The new Burbo Bank offshore wind farm in Liverpool Bay [6].

In the civil engineering industry, FRP have found rapid growth in applications for building and bridge construction. The main reasons for this is due to their advantageous properties, such as low-weight, high strength, free formability and substantial resistance to corrosion and fatigue. Moreover, these materials have low thermal conductivity and can be produced in translucent or transparent form [7]. Some examples of hybrid bridge constructions using FRP cables are given in Table 1.4. In Figure 1.5, cross-sections of glass fibre reinforced polymer (GFRP) elements used in civil engineering are given.

This text box is where the unabridged thesis included the following third party copyright material:

Keller, T. (2001). Recent all-composite and hybrid fibre-reinforced polymer bridges and buildings. Progress in Structural Engineering and Materials, 3(2), 132-140.

Figure 1.5 Cross-sections of GFRP elements [7].

Table 1.4 Hybrid bridge constructions with FRP cables [7].

Bridge	**Location**	**Year**	**Elements**
Kleine Emme Pedestrian Bridge	Luzern, Switzerland	1998	Post-tensioning cables, integrated FOS
Dintelhaven Road Bridge	Rotterdam, Holland	1999	External post-tensioning cables
Passerelle des Neigles Pedestrian Bridge	Fribourg, Switzerland	1999	Suspension bridge cables
Herning Pedestrian Bridge	Herning, Denmark	1999	Stay cables

Figure 1.6 shows an example of a hybrid composite bridge, which is the 25-metre Pontresina Bridge in Switzerland. This bridge, weighing 300 kg with a load capacity of 500 kg/m^2, consisting of two sections each 12.5 metres long, was built for pedestrians and skiers. Some of the attractive features of this composite bridge include low weight, high strength, easy handling and quick installation, weather resistance as well as flexibility in dimensions and design to meet customer requirements. In addition, during spring time, the bridge is easily disassembled to avoid damming and flooding when the melting water carries stones and gravel through the riverbed [8].

Figure 1.6 Pontresina bridge in Switzerland [8].

In the transportation industry, composites and sandwich structures are found in high speed trains. For example, Divinycell cores with GRP skins are used in the manufacture of train components for China's new generation of high speed trains, together with wood or aluminium skins. Amongst the attractive features of these components are a higher peel strength, improved stiffness and impact properties, in addition to being lightweight. For train interiors, this Divinycell sandwich composite offers low water absorption, excellent thermal and acoustic insulation and an improved fatigue life [9]. An example of China's new generation of high speed-train is given in Figure 1.7.

Figure 1.7 New Generation' high-speed train [9].

Another example is a train nose structure for Kuala Lumpur's Monorail, as shown in Figure 1.8. This sandwich structure consists of skins made of an epoxy/glass prepreg system sandwich bonded to a core of DIAB Divinycell P150 foam. This reduces the weight of the structure by approximately 30% relative to a polyester-based component.

Figure 1.8 A lightweight structure for Kuala Lumpur's monorail system manufactured by DK Composites, Malacca, Malaysia [10].

In the automotive industry, the use of carbon fibre-reinforced plastics (CFRP) is still small, limited mostly to racing cars, supercars and high-end luxury vehicles [11]. An example of this is Australia FR-1, which is a two-seater roadster car made from composites and hybrid materials, as shown in Figure 1.9. This cockpit structure, with dimensions of 2 by 1.5 metres, was designed by the VCAMM/Boeing team and has a total weight of 80 kg. In spite of this lightweight design, this car still provides a high torsional rigidity.

Figure 1.9 The Australia FR-1, a two-seat roadster concept car [12].

1.2 Motivation and Scope of the Research Work

Given the limited knowledge on the oblique impact response of composites and sandwich structures, this research study aims to undertake an experimental and analytical investigation of such structures under low-velocity, dealing with damage initiation and progression, the prediction of the maximum contact force as well as identifying the failure mechanisms and energy absorption characteristics under normal and oblique impact in both plain laminates and sandwich structures.

1.3 Aims and Objectives of the study

The principal aims of this research study are to investigate the effect of non-normal loading on the low-velocity impact response of composites and sandwich structures. The research study focuses on glass fibre reinforced epoxy laminates as well as polymeric foam sandwich structures, over a range of impact angles.

The objectives of this research study are:-

i. To investigate changes in damage development with angle of obliquity
ii. To study the variation of the damage threshold energy as well as perforation behaviour with increasing impact angle
iii. To propose a suitable model to predict both the normal and non-normal impact response of laminates and sandwich structures
iv. To investigate the effect of varying core properties on the impact response of sandwich structures at normal and oblique impact angles

1.4 Organisation of the Thesis

This PhD thesis is comprised of a further four chapters as follows:-

- Chapter II. Literature Review : this chapter gives a general classification of impact response, impact dynamics, contact laws, impact damage in composites and sandwich structures, damage predictions, residual properties as well as a specific sub-topic on the oblique impact response of composite structures;
- Chapter III. Experimental Procedure: describes the experimental work involved in the research work as well as the specific theoretical model/ mathematical models. This chapter consists of materials preparation, experimental testing (static and dynamic), the analytical model (Energy-Balance Model) considered in the study, damage characteristics including visual observations, measurement of the maximum permanent indentation, as well as an optical microscopy analysis on the cross-sectional area of the impacted samples.
- Chapter IV. Results and Discussion: presents and discusses the results from the experimental and analytical work elaborated in Chapter III.
- Chapter V Conclusions and Recommendations for Future Work: summarises the overall findings and discussions. In addition, suggestions for continuing the work outlined in this study are presented.

1.5 References

[1] http://www.compositesuk.co.uk/LinkClick.aspx?fileticket=Wm0WJ7RfFY0%3D&tabid=104&mid=532 Accessed on 27th August 2014.

[2] Composite Materials Revolutionise Aerospace Engineering. (2008). Ingenia, (36), 25-28.

[3] Zenkert, D., Shipsha, A., Bull, P., & Hayman, B. (2005). Damage tolerance assessment of composite sandwich panels with localised damage. Composites science and technology, 65(15), 2597-2611.

[4] Vallbo, S. (2005). Material selection considerations for polymer composite structures in naval ship applications. Journal of Sandwich Structures and Materials, 7(5), 413-429.

[5] Brøndsted, P., Lilholt, H., & Lystrup, A. (2005). Composite materials for wind power turbine blades. Annu. Rev. Mater. Res., 35, 505-538.

[6] http://www.thesundaytimes.co.uk/sto/news/uk_news/Environment/article991336.ece Accessed on 27th August 2014.

[7] Keller, T. (2001). Recent all-composite and hybrid fibre-reinforced polymer bridges and buildings. Progress in Structural Engineering and Materials, 3(2), 132-140.

[8] http://www.fiberline.com/structures/profiles-and-decks-bridges/profiles-footbridges-and-cycle-bridges/case-stories-footbridge/pontresina-bridge-switzerla Accessed on 27th August 2014.

[9] http://www.diabgroup.com/Cases/Transport/Chinas-New-Generation-high-speed-trains-use-Divinycell-H-and-P Accessed on 27th August 2014.

[10] http://www.diabgroup.com/en-GB/Cases/Transport/Decreased-monorail-weight-means-dual-success-for-DK-Composites-and-DIAB Accessed on 27th August 2014.

[11] http://www.compositesworld.com/articles/automotive-cfrp-repair-or-replace Accessed on 27th August 2014.

[12] http://www.compositesworld.com/articles/out-of-autoclave-prepreg-enables-concept-sports-car Accessed on 27th August 2014.

CHAPTER II: LITERATURE REVIEW

This chapter presents a review of relevant past and current research work on composites and sandwich structures subjected to normal and oblique impact, with the focus on low-velocity impact. A brief overview of the impact response classifications as well as some of the available impact models relating to impact dynamics is given. Other important aspects included in this review are contact mechanics, impact damage in composites and sandwich structures, damage prediction, perforation behaviour and residual properties of the composites and sandwich structures. In addition, relevant studies on oblique impact in composites and sandwich structures are discussed with examples of published experimental and numerical work.

2.0 Introduction

A large number of research studies have focused on the impact response of composite laminates [1-52] and sandwich structures [18, 46, 53-94], since it is well established that impact events affect the mechanical performance of composite materials, e.g. by precipitating a reduction in the strength of the structure, which can lead to catastrophic failure. Under low-velocity impact, damage is frequently barely visible (BVID) and often cannot be detected by Non-Destructive Testing (NDT). Impact events can occur during the manufacturing process, in-service operation as well as during the life of a structure or component. In addition, it should be noted that most impact events are non-normal or oblique in nature [42, 95, and 96]. In addition, depending on the angle of incidence of the indenter with respect to the target, rebounding or ricocheting can occur [42, 96]. To date, a limited number of

studies have focused on the oblique impact response of composites [51, 52, 87, 93, 95-99]. Moreover, most of these works are dedicated to ballistic impact [51, 52, 96-98, 99].

2.1 Classifications of Impact Response

In simple terms, a general classification of impact considers low-velocity impact and high-velocity impact scenarios. Cantwell and Morton [5] classified low-velocity impact to include velocities up to 10 m/s. They also concluded that under low-velocity impact, the energy absorption capability is dependent on the size and shape of the target, whilst under high-velocity impact, which involves a localized form of target response; damage is independent of target geometry [2]. This classification has been adopted for this research project, which is dedicated to a study on the normal and oblique impact response of composites and sandwich structures for velocities less than 10 m/s.

Chai and Zhu [58] outlined two criteria in order to classify the impact response of composite laminates and sandwich structures. These criteria are based on structural deformation and damage, with low-velocity impact causing localised plastic deformation around the area of contact, whilst high velocity impact results in a large area of delamination or damage around the contact area; and a structural response. The latter criteria are based on the earlier work by Stronge [44] and Olsson [17], where it was argued that the impact response and resulting damage may be different for impacts having the same velocity but different impact masses. According to this criteria, in addition to impact velocity and mass, the impact duration, t, also represents a key parameter in differentiating between low and high velocity impact.

On the basis of impact duration, *t*, three classifications of impact response has been outlined as follows [58]:-

i. When the impact duration, $t \sim \frac{h_c}{\sqrt{E/\rho}}$, is of the order of the transition time for the stress wave to travel through the thickness of the target. Here, response is dominated by three dimensional wave propagation. This response is commonly governed by stress wave propagation.

ii. When the impact duration, $t \sim \frac{R_p}{E/\rho_1}$ is significantly longer than the time taken for the flexural and shear stress waves to travel to the boundary. This response is usually analysed using Modal Superposition Method [8-11].

iii. When the impact duration, $t \gg \frac{R_p}{\sqrt{E/\rho_1}}$ is much larger than the time required for the stress waves to reach the boundary, the impact response is governed by the lowest vibration mode of the indenter-plate system. This type of response can be modelled using a quasi-static analysis and an energy-balance model is commonly employed to predict this type of impact response whereby:-

$\sqrt{E/\rho_1}$ is the stress wave velocity;

E_f is the elastic modulus of the facesheet;

ρ_1 is the density of the face sheet;

h_c is the height of the core ; and

μ_{ij} is the Poisson's ratio of the facesheet.

2.2 Impact Dynamics (Impact Models)

In understanding the impact of foreign objects on a composite or sandwich structure, it is crucial to develop a suitable model to predict the contact force history as well as the overall response of such a structure. To-date, many different models have been proposed in the literature. Amongst these are the energy-balance models [40], in which the target is considered to behave quasi-statically and a maximum contact force is predicted using this model; and secondly, the spring-mass model. The spring mass model is a simple and accurate solution for impact on a small size specimen [11, 53].

Both models are briefly discussed in this section. In addition, it should be noted that impact on composites and sandwich structures is a three-dimensional problem, and for a full understanding of the complete impact problem, a more appropriate comprehensive model is needed. Amongst the possible solutions is the use of a numerical model using one of the finite element analysis (FEA) software packages available in the market today.

2.2.1 Spring-mass model

In the spring-mass model, two approaches are frequently considered, the single-degree of freedom (SDOF) and the two degree of freedom (TDOF) models, as shown in Figure 2.1.

Figure 2.1 (a) The single-degree-of-freedom model, where M= mass of the target, K = spring stiffness and X = indentation ; (b) the two-degree-of-freedom model, where M_1= the mass of the indenter, M_2 = effective mass of the target, K_b = bending stiffness, K_s = shear stiffness, K_m = membrane stiffness, x_1 = indentation of the indenter, x_2 = indentation of the target [11].

Caprino *et al*. [6] used the single-degree-of-freedom (SDOF) model and showed that one of two situations is likely to occur, depending on the ratio, *M*, of the target mass, *m*, to the mass of the indenter. At high values of *M*, a significant percentage of the total energy in the system is converted into vibrations, requiring vibrational effects to be taken into account.

In contrast, when the value of *M* is very small, i.e. for impact of a heavy indenter on a light structure, vibrational effects are negligible. In such cases, the plate mass can be neglected and the two-degree-of-freedom model can be reduced to a single-degree-of-freedom model.

The transverse collision of a rigid indenter with a uniform, linearly elastic plate can be modelled by replacing the plate by a linear spring with a constant stiffness, *k*, which represents the static force required to produce a unit transverse deflection of the plate.

If the mass of the plate is negligible compared to the mass of the indenter, the model is reduced to a one degree of freedom problem. As illustrated in Figure 2.2, the model shows the condition where V_o, is the velocity of the indenter immediately before impact, which has a mass of *m*.

Figure 2.2 Linear spring of constant, *k*, impacted by a striker having a mass,*m*, and initial velocity, V_o [6].

With the assumption that the energy losses are negligible, an energy-balance for the system at an instant in time, *t*, is given as:-

$$U_0 = U_i + U_p \tag{2.1}$$

where U_o, U_i and U_p are the energy of the indenter before impact, its energy at time, *t*, and the strain energy stored by the plate at time, *t*, respectively.

The contact force expressed as a function of time is:-

$$F = F_{max} \sin \pi \frac{t}{t_c} \tag{2.2}$$

where:

$$F_{max} = \sqrt{2U_o k} \; = \; V_o \sqrt{mk} \tag{2.3}$$

and

$$t_c = \pi\sqrt{\frac{\mathrm{m}}{k}} \tag{2.4}$$

where F_{max} , t_c , V_o and k is the maximum load, contact time, impact velocity and constant which represents the static force required to produce unit transverse deflection, respectively.

2.2.2 Energy-balance model

Based on the conservation of energy in the indenter-structure system, the initial kinetic energy of the indenter is used to deform the structure during an impact. Assuming that the structure behaves quasi-statically, when it reaches its maximum deflection, the velocity of the indenter becomes zero and all of the initial kinetic energy has been used to deform the structure. Therefore, the energy-balance can be expressed by:

$$\frac{1}{2}\,MV^2 = E_b + E_s + E_m + E_c \tag{2.5}$$

where M is the total mass of the indenter, V is the velocity of the indenter, the subscripts b, s and m refer to the bending, shear and membrane components of the overall structural deformation. E_c is the energy stored in the contact region during indentation.

The maximum contact force and the contact duration are expressed by Equations 2.6 and 2.7 respectively, when the overall deflection of the structure is negligible compared to the local indentation.

$$P = \left(\frac{5}{4}\right)^{3/5} [M^3 V^6 k^2]^{1/5} \quad 2.6$$

$$T_c = 3.2145 \left[\frac{[M^2]}{{V_k}^2}\right]^{1/5} \quad 2.7$$

The relationship between the contact force, *P*, and the overall deformation of the plate is given by [11]:-

$$P = K_{bs}\delta + K_m\delta^3 \quad 2.8$$

where P is the contact force, K_{bs} is the linear stiffness including bending and transverse shear deformation effects, K_m is the membrane stiffness and δ is the overall deformation.

The energy absorbed in membrane and bending/shear is given by:-

$$E_m = \frac{1}{4} K_m {\delta_o}^4; \quad E_{bs} = \frac{1}{2} K_{bs} {\delta_o}^2 \quad 2.9$$

Substituting Equations (2.8) into (2.9) gives:

$$2M{V_o}^2 = 2K_{bs}\delta^2 + K_m {\delta_o}^4 + 4\chi \int_0^{\alpha_0} \sqrt{\alpha(t) + \beta\alpha^{3(t)} d\alpha} \quad 2.10$$

where δ_o and α_o are the maximum deflection and indentation of the panel, [60].

The elastic response of a sandwich beam structure has been modelled using the following expression [54]:-

$$\frac{1}{2} m v^2 = E_{bs} + E_c \quad 2.11$$

The force-displacement relationship for a sandwich beam is given as:-

$$\delta = P\left[\frac{L^3}{48D} + \frac{L}{4AG}\right] \tag{2.12}$$

where G is the shear modulus of the foam core, L is the span, D is the flexural rigidity of the skins and A is a geometrical parameter that depends on the thickness of the core and skin materials, as well as the beam width.

It was shown that the energy absorbed in bending and shear effects at maximum displacement, δ_{max}, is equal to:-

$$E_{bs} = \frac{{P_{max}}^2}{2}\left(\frac{L^3}{48D} + \frac{L}{4AG}\right) \tag{2.13}$$

By modelling the contact response using Meyer's contact law, the energy absorbed in contact effects can be expressed as follows :-

$$E_c = \int_0^{\delta_{max}} P\, d\alpha = \frac{C\left({P_{max}}/{C}\right)^{\frac{(n+1)}{n}}}{n+1} \tag{2.14}$$

Therefore, the energy-balance model for the sandwich structures is:-

$$\frac{1}{2}mv^2 = \frac{{P_{max}}^2}{2}\left(\frac{L^3}{48D} + \frac{L}{4AG}\right) + \frac{C\left({P_{max}}/{C}\right)^{\frac{n+1}{n}}}{n+1} \tag{2.15}$$

2.3 Contact Mechanics

In studying the dynamic response during an impact of a indenter on a target, it is important to identify the contact law that relates the contact force and the resulting indentation. The contact law is defined as the relative displacement between the indenter and the target, including the effect of permanent indentation and local damage that is introduced during the process. This is usually found to be non-linear.

Contact laws for the indentation behaviour of a sandwich structure greatly differ from that for monolithic laminates, with the local deformation in the contact zone due to the local indentation of the top face sheet and in a large part of deformation of the core material under the face sheet. For example, in sandwich structures, the indentation response is dominated by the behaviour of the core [53].

2.3.1 Indentation of laminates

Sutherland and Soares [45] studied the contact indentation response of woven E-glass laminates. With the assumptions that contact occurs between two smooth elastic, homogeneous, isotropic solid bodies of revolution, the contact force, *P*, was related to the indentation, α, by an expression as given in Equation 2.16, which is also commonly known as the Hertz Contact Law as follows:-

$$P = C\alpha^{3/2} \tag{2.16}$$

Where

$$C = \frac{4E\sqrt{R}}{3} \tag{2.17}$$

and

$$\frac{1}{E} = \frac{1-{v_1}^2}{E_1} + \frac{1-{v_2}^2}{E_2}; \frac{1}{R} = \frac{1}{R_1} + \frac{1}{R_2} \quad 2.18$$

where C is the contact stiffness, the subscripts 1 and 2 refer to the indenter and target respectively, E refers to Young's Modulus, R is the radius of the indenter and v is the Poisson's ratio. Here, the value of indentation exponent, n, is taken as 3/2, as in Equation 2.16. An illustration showing the relationship between the parameters are shown in Figure 2.3.

This text box is where the unabridged thesis included the following third party copyright material:

Sutherland, L. S., & Soares, C. G. (2005). Contact indentation of marine composites. Composite structures, 70(3), 287-294.

Figure 2.3 Schematic of a static indentation test showing impact force (P), displacement, (δ), indentation, (α) and deflection (w) [45].

2.3.2 Indentation response of sandwich structures

One of the shortcomings of sandwich structures is the reduction in load-carrying capacity, which is attributed to the occurrence of indentation damage [85]. Therefore, it is crucial to understand the indentation response of these structures.

Shuaeib and Soden [85] reported that skin thickness and core densities affect the indentation failure load in the sandwich panels. However, the core thickness has only a marginal effect on the failure load, whereas indenter size showed no significant effect on the failure load.

Figure 2.4 (a) is an example of an indentation test set-up, while in Figure 2.4(b), the experimental and the simulated static indentation responses are given. It is apparent that good agreement between the simulated load–indentation curve and the experimental results is observed, particularly in the initial elastic region. However, at increasing values of deflection, the numerical model tends to over-predict the experimental stiffness. Rizov *et al*. [80] argued that the reason for this is because in the numerical study, no damage initiation and growth was assumed in the facesheet model, whereas the experiments showed remained damage onset in the facesheet.

Figure 2.4 (a) Indentation test set-up, and in (b) Comparison between load–indentation curves deduced from finite element modelling and indentation test testing [80].

Figure 2.5 shows a typical stress-strain curve following a compression test on polyurethane foam [74]. Here, it is highlighted that there are three important regions occurring on a stress-strain plot, which are (i) elastic behaviour; (ii) crushing of the foam; and (iii) densification of the foam.

Figure 2.5 Typical stress–strain curve for the compression of a polyurethane foam (80 kg/m^3) [74].

In addition, a schematic diagram showing the condition of the sandwich foam structure during such loading condition is given in Figure 2.6. It is apparent here that the indentation force, *P*, resulted in a localised crushed zone normal to the indentation load, with the radius labelled as *l*, whilst the rest of the structure remained undamaged.

Figure 2.6 A schematic of a sandwich beam during indentation [74]. (Note: z = longitudinal direction, x = transverse direction, P = applied load, l = half length of crushed foam).

In addition, a schematic diagram showing the condition of the sandwich foam structure during such loading condition is given in Figure 2.6. It is apparent here that the indentation force, *P*, resulted in a localised crushed zone normal to the indentation load, with the radius labelled as *l*, whilst the rest of the structure remain undamaged.

In another study, Hassan and Cantwell [62] argued that, following a series of quasi-static and impact tests on sandwich structures using six different polymer foams, the indentation behaviour of a sandwich structure is greatly influenced by the properties of the core material. In addition, using the Meyer indentation law in which the contact force, *P*, is related to the indentation as given in Equation 2.19 below:-

$$P = C\alpha^n \qquad 2.19$$

It was found that the contact stiffness, *C*, increased significantly from quasi-static to dynamic rates, whereas the values of the indentation exponent, *n*, are relatively close under both strain rates, as shown in Figure 2.7.

Figure 2.7 (a) Comparison of the quasi-static and dynamic values of (a) the contact stiffness parameter, *C*; and (b) indentation exponent '*n*'[62].

2.4 Impact Damage in Composites and Sandwich Structures

Frantziskonis [100] defined damage as "the effect of micro-failure events on the material behaviour, or as a collection of permanent (irreversible) microstructural changes brought about in the material by a physical process, resulting from the application of loads".

Due to the anisotropic behaviour of composite materials, damage development in composite laminates is more complex than in conventional structural materials, such as steel and aluminium. Abrate [8] argued that significant damage in composite

laminates, in the form of delamination, matrix cracking, or fibre breakage can be present, leading to a significant reduction in strength. However, sometimes this may not be detectable under visual inspection. Hence, it is crucial to understand the impact phenomenon and the damage mechanisms in developing new materials with an improved impact resistance.

2.4.1 Failure mode in composite laminates

Typically, for a non-penetrating impact in a laminated composite system, damage occurs in the form of delamination (debonding between adjacent plies), matrix cracking, and fibre failures. Debonding is of major concern, since it has been reported that this type of damage leads to a serious reduction in the strength of a laminate, with the location of delamination being at the interface between plies of different fibre orientation. Two types of matrix cracking are identified, as illustrated in Figure 2.8, these being tensile cracking and shear cracking. Tensile cracks occur when the in-plane normal stresses exceed the transverse tensile strength of the ply, whilst the shear cracks propagate at an angle from the mid-surface, due to transverse shear stresses. When a laminate is impacted at the top surface, an oblong or "peanut" shaped form of damage is induced, with the major axis being in the fibre direction of the lower ply at that interface [11].

Figure 2.8 Types of matrix cracking including (a) tensile cracking and (b) shear cracking [11].

Cantwell and Morton [2] studied perforation in the low and high-velocity impact behaviour of CFRP laminates with varying thicknesses. From the optical micrographs of the impacted surfaces, three fracture mechanisms were identified; these being matrix cracking, delamination and fibre fracture. Fracture initiated at the upper surface in thicker laminates, whilst the thinner laminates showed initial failure at the lowermost ply, directly under the impact point. The fracture zone had a conical shape at impact energies above the damage initiation threshold. During low-velocity impact on CFRP laminates, three major energy-absorbing mechanisms were identified; these being elastic deformation, delamination and shear-out, depending on the laminate type, thickness and support conditions.

Richardson and Wisheart [19], in their review of low-velocity impact properties of composites, listed four major modes of failure for a fibre-reinforced plastic (FRP); these being matrix mode, delamination mode, fibre mode and penetration. The matrix mode develops when cracking occurs parallel to fibres due to tension, compression or shear. The delamination mode is produced by interlaminar stresses; whilst the fibre mode is associated with in-plane tension fibre breakage and in-plane compression fibre buckling. Lastly, penetration occurs when the indenter completely perforates the target.

Shyr and Pan [41] studied the damage characteristics and fracture behaviour of three types of glass fibre reinforced laminate, based on a non-crimp fabric, a woven fabric and a non-woven mat at energies up to 24 J. They reported that fibre breakage occurred prior to major damage. With an increase in impact energy above the threshold limit, matrix cracking, delamination, and fibre breakage were observed at

the back surface, as a result of bending stresses, as presented in the schematic diagram in Figure 2.9.

Figure 2.9 Schematic representations showing a typical impact damage mode for a composite laminate [41].

2.4.2 Failure mode in sandwich structures

Chai and Zhu [58] listed five competing failure modes following impact on sandwich composites with a honeycomb core, these being core buckling and debonding, core shear and cracking, delamination in the top facesheet, facesheet matrix cracking and fibre breakage in the facings. They stated that damage in the core is often due to an excessive contact pressure, whilst damage in the top facesheet is mainly due to localised deformation around the contact area, similar to that observed in laminates. In most cases, the bottom facesheet remains intact following low-velocity impact loading.

In addition, it was also argued that based on the experimental observations on impact response of sandwich structures, the response of the impact force, *P*, with the displacement of the indenter, *u*, may be divided into three stages, as illustrated in

Figure 2.10 [58]. These are stage I, called the elastic region/ elastic stage, in which no visible damage occurs in the sandwich structures, and the response is essentially linear elastic and ends at an initial threshold load P_1 at displacement u_1.

Following this, in stage II, once the impact force exceeds P_1, the curve becomes non-linear with a sudden drop in structural stiffness indicating the onset of initial damage that may include core bucking and localized damage in the facesheet. The impact force increases significantly in this stage mainly due to the membrane effect of the top facesheet. In quasi-static tests, this drop in the load is obvious and is observed to occur together with a cracking sound. This stage ends with a maximum force P_m at displacement u_f. This maximum force P_m is usually much larger than the initial threshold force.

Finally, in stage III, if the top facesheet is perforated, the stiffness and load-carrying capacity of the impacted sandwich panel will drop dramatically.

Figure 2.10 Typical stages of load-displacement curve for a composite sandwich panel subjected to normal impact loading [58].

2.4.3 Damage Prediction

It is crucial to predict the resulting damage following impact since it is a true indication of the component structural integrity and safety requirement, particularly for engineering structures. Over the years, extensive research has been dedicated in understanding damage initiation and progression in composites and sandwich structures. However, since the dynamic properties and failure behaviour of these structures are complex and, in most cases a 3D problem, continuous efforts using computational methods are sought.

2.4.3.1 Damage predictions in composite laminates

Past research on composite laminates have shown that the impact force required to initiate damage, P_{crit}, varies linearly with $t^{3/2}$, in which t is the target thickness [7].

Davies and Zhan [28] conducted a series of experimental tests on quasi-isotropic laminated plates with three different thicknesses. From the plot of damage area versus impact load, they argued that a threshold value for the onset of damage could be identified, with the damage size increasing rapidly beyond the threshold value. It has been shown that the critical impact load or threshold value, P_{crit}, can be given as:-

$$P_c^{\,2} = \frac{8\pi^2 E t^3 G_{IIc}}{9(1-\upsilon^2)} \qquad 2.19$$

where t is the laminate thickness, E the flexural modulus, υ is the Poisson's ratio and G_{IIc} is the critical value of the energy release rate for Mode II fracture.

Impact tests on low fibre volume glass polyester laminates have shown that these materials delaminated at very low impact forces. The reasons for these include (i) shear stresses due to global deflections or due to local contact force induced shear stresses, or, (ii) to an interaction between both mechanisms. Based on this understanding, Sutherland and Soares [45] conducted a series of quasi-static indentation tests on E-glass/polyester laminates, with the focus on studying the delamination due to local contact forces.

With the assumption that delamination occurs as the interlaminar shear strength (ILSS) is exceeded, it has been found that the critical load at which delamination occurs, P_{crit}, is given as below:-

$$P_{crit}{}^{2} = \left(\frac{6ILSS^{3}\pi^{3}t^{3}}{E}\right)R \qquad 2.20$$

Where t is the material thickness, R is the indenter radius and E is the Young's Modulus of the composite. In addition, the interlaminar shear strength (ILSS) can be determined experimentally under both static and dynamic loading on a small composite beam.

Using a similar expression as in Equation 2.20, Yang and Cantwell [7] showed that the value increased with both the target thickness as well as indenter diameter, as shown in Figure 2.10.

Figure 2.10 The variation of the damage initiation force with indenter radius based on a GFRP plate [7].

2.4.3.2 Damage predictions in sandwich structures

Damage initiation in composite sandwich panels depends primarily on the panel support conditions, the indenter nose-shape and the facesheet thickness [58, 66]. As an example, rigidly-supported panels undergo only top facesheet fracture under the indenter and core shear failure; for the simply supported and clamped conditions, tensile failure of the bottom or back facesheet may happen in addition to top facesheet fracture and core shear failure. Impact damage in the top facesheet is similar to that observed in monolithic composites; however, the core in the sandwich panel causes facesheet damage is more localized to the point of impact, under the indenter [66]. Based on these criteria, damage initiation can be characterized by three modes as follows:-

a) Top facesheet failure:

Two failure criteria are proposed for top facesheet damage initiation including:-

i. Shear Failure:

Shear failure of the top facesheet occurs when the shear stress in the facesheet equals the shear fracture stress, τ_{13}. This is more likely to take place when the facesheets are relatively thick and do not undergo very large indentation. It has been shown that the indentation load at shear failure, P_f, is given by:

$$P_f = 2\pi Rh\tau_{13} + K_c\pi R^2 q \qquad 2.21$$

where K_c is a constraint factor, R is the radius of the indenter and h is the thickness of the facesheet.

At damage initiation, by replacing the failure load with the maximum impact force and considering the dynamic material properties, it can be shown that

$$F_f = 2\pi R\tau_{13d}h + K_c\pi R^2 q_d \qquad 2.22$$

where τ_{13d} is the dynamic transverse shear strength of the facesheet and q_d is the dynamic crushing strength.

ii. Tensile Failure:

This type of failure occurs when the strains are equal to the tensile fracture strain, ε_{cr} or when the corresponding membrane forces reach the membrane fracture force, N_{cr}. This mostly takes place when the facesheet are thin and deflections are large so that high tensile forces are developed in the facesheet. Hemispherical-shaped indenter having a large radius of curvature usually results in circumferential cracks. For a

smaller radius of curvature values as well as cylindro-conical indenters, the cracks tend to develop in the form of radial cracks.

The damage initiation load for a circumferential crack is proven by:-

$$P_f = 2\pi R_e N_{cr} w'_{cr} + K_c \pi q {R_e}^2 \quad 2.23$$

Where R_e is effective radius of the indenter, and N_{cr} is tensile membrane forces and w'_{cr} is the critical top facesheet deflection.

If the radial crack length is small, it can be assumed that $N_{cr} w'_{cr}$ is roughly uniform.

Therefore, for a total damage length, *d*, the total failure load is proven as follows:-

$$P_f = d N_{cr} w'_{cr} + K_c \pi q {R_e}^2 \quad 2.24$$

If the top facesheet is modelled as a membrane and by neglecting the in-plane deformation, the facesheet strains are proven as follows:-

$$\varepsilon = \frac{1}{2}(w')^2 \quad 2.25$$

By equating this to the tensile fracture strain, the following expression is sought:-

$$w'_{cr} = \sqrt{2\varepsilon_{cr}} \quad 2.26$$

Also, the tensile membrane forces at failure are approximated as below:-

$$N_{cr} \approx A_{11}\varepsilon_{cr} \quad 2.27$$

Where A_{11} is laminate extensional stiffness.

The damage initiation load due to circumferential cracking equals:-

$$P_f = 2\pi R_e A_{11}\varepsilon_{cr}\sqrt{2\varepsilon_{cr}} + K_c\pi q {R_e}^2 \quad 2.28$$

Also, for the radial cracking, the damage initiation load is expressed as below:-

$$P_f = dA_{11}\varepsilon_{cr}\sqrt{2\varepsilon_{cr}} + K_c\pi q {R_e}^2 \quad 2.29$$

In addition, it has been shown that the dynamic tensile failure criterion (F_f) for impact damage (for circumferential cracks) can be expressed as below:-

$$F_f = 2\pi R_e A_{11d}\varepsilon_{crd}\sqrt{2\varepsilon_{crd}} + K_c\pi q_d {R_e}^2 \quad 2.30$$

Also, for radial cracks,

$$F_f = dA_{11d}\varepsilon_{crd}\sqrt{2\varepsilon_{crd}} + K_c\pi q_d {R_e}^2 \quad 2.31$$

b) Core shear failure

It has been shown that the transverse shear fracture strain can be calculated from the shear strength as follows:-

$$\gamma_f = \frac{\tau_f}{G_{13}} \quad 2.32$$

where G_{13} is the transverse shear modulus of the honeycomb. Core shear failure occurs when the actual transverse shearing strain in the honeycomb equals to γ_f.

c) Bottom facesheet failure:

Bottom facesheet failure can happen in clamped panels if the core crushing resistance is high enough to resist local deformation or top facesheet indentation.

The entire panel deforms in a shear-bending mode and failure may take place when the maximum tensile strains in the bottom facesheet are at the critical fracture strain. The maximum tensile strain occurs right under the indenter or middle of the plate, where the bending moment is a maximum.

2.5 Perforation behaviour of composite laminates and sandwich structures

Numerous works have been dedicated to studying the perforation behaviour of composites and sandwich structures, particularly in the low-velocity impact regime under normal impact conditions [3, 32, 59, 63, 69, 70, 73, 78] as well as in the high velocity range [13, 18, 22, 39, 66]. Moreover, several research papers have also considered both quasi-static perforation in comparison to dynamic loading conditions [22, 47, 71, 89] since some composite materials, such as glass-fibre reinforced composites, are strain-rate sensitive [22, 62]. Hence, they behave differently under both loading conditions [79].

2.5.1 Perforation behaviour of composite laminates subjected to normal impact

Cantwell and Morton [3] studied the perforation behaviour of carbon fibre-reinforced composite laminates with thicknesses between 0.5 and 2.0 mm , subjected to both

low and high velocity impact, using a 6-mm diameter hemispherical indenter at up to 2 m of release height. For the low-velocity impact case, the *perforation threshold energy*, defined as the lowest energy required in perforating the composite target, was predicted using the principle of conservation of energy. Close examinations of the optical micrographs revealed that there are three fracture mechanism associated with the perforation under this impact loading; these being matrix cracking, delamination and fibre fracture. In addition, it was observed that for thicker composite laminates, failure tends to initiate at the upper surface of the target, while the thinner laminates showed failure initiation directly under the point of impact. At energies above the damage initiation threshold, the fracture zone was generally conical in shape, with the overall area of damage increasing towards the lower surface of the composite laminates. A large number of matrix cracks were also apparent at this energy level, extending away from the point of contact. Lastly, at the perforation threshold energy, regardless of whether the target was subjected to low or high velocity impact, similar observation was found; that is the steel sphere removed a conical-shaped shear plug as it penetrated the target.

From these findings, it was proposed that for the case of low-velocity impact response, the areal dimensions of the target determine the perforation energy. In contrast, under high velocity impact condition, the perforation energy was found to be independent of the areal geometry of the structure [3].

2.5.2 Perforation behaviour of sandwich structures subjected to normal impact

Wen *et al*. [79] highlighted three important steps of panel failure during deformation in a sandwich structure. These are (i) initial failure where one of the skins of the

panel is fractured, with or without considerable deformation of the core; (ii) penetration of the indenter through the thickness of the panel; and (iii) perforation of the panel when the whole of the indenter has emerged through the panel.

In addition, there are three different failure modes associated with the initial failure; these being (i) indentation failure; (ii) core shear failure and (iii) panel bending failure. Indentation failure usually occurs in panels with soft cores and flexible skins, and associated with small diameter indenter; whereas the core shear failure occurs when the core is stronger, and failure takes the form of shear plugging of the top skin, along with simultaneous development of conical, shear cracks in the core, mainly with a flat-faced indenter. With panel bending failure, the bottom skin of the panel failed due to tensile stresses caused by bending. Up to this point, there was little or no deformation of the core or of the top skin.

Figure 2.11 gives typical load-displacement traces following low-velocity impact on GRP skin sandwich panels using three types of indenter; these being (a) flat-faced (9.5 m/s), (b) hemispherical-ended (7.38 m/s) and (c) conical-nosed indenters (7.38 m/s). Also, the load-displacement traces following a series of static indentation tests using similar parameters are also included for correlation. Less severe damage was observed in the panels subjected to drop-weight impact than was observed in the corresponding quasi-static panels, although higher impact energies were imposed on the panels. However, the extent of debonding between the lower skin and the core was larger in the impact tested panels. In addition, the dynamic load required to cause a given deflection was higher than the load required causing the same deformation under quasi-static loading conditions. Two main reasons were given for

this observation; (i) enhanced strength and stiffness of the components due to rate-dependent material properties, (ii) inertia effects [79].

Figure 2.11 Comparison between quasi-static and impact load-displacement characteristics for 0.9 m square sandwich panels with 3.25-mm GRP skins and 25 mm thick H130 foam core loaded by 50 mm diameter indenters.
(a) Flat-faced (b) hemispherical-ended; (c) conical-nosed [79].

Hassan and Cantwell [63, 64] studied the effect of core density on the perforation resistance of sandwich structures using nine different foam cores, based on cross-linked PVC foams, linear PVC foams and PET foams. Examples of typical load-displacement traces following drop weight normal impact test on the sandwich structures of the (a) linear PVC and (b) the PET foams are shown in Figure 2.13. From this investigation, the perforation resistance was found to be greatly dependent on the Mode II work of fracture of the foam materials. Examples of the failure mode

in the different sandwich panels following perforation of the hemispherical indenter are shown in Figure 2.14. For the linear PVC sandwich panels, as in Figure 2.14 (a) it is apparent that the sandwich panels exhibit presence of a foam plug close to the rear surface of the sandwich structures, since the area had been compressed by the indenter during the perforation process. In Figure 2.14 (b), for the PET sandwich panels (lowest density foam core), the presence of both cylindrical shear zone as well as tensile cone cracking are clearly evident.

This text box is where the unabridged thesis included the following third party copyright material:

Hassan, M. Z. (2012). The low velocity impact response of sandwich structures (Doctoral dissertation, The University of Liverpool).

Figure 2.12 Typical load-displacement traces following drop weight normal impact test on the sandwich structures of the (a) linear PVC and (b) the PET foams [64].

This text box is where the unabridged thesis included the following third party copyright material:

Hassan, M. Z., & Cantwell, W. J. (2012). The influence of core properties on the perforation resistance of sandwich structures–An experimental study. Composites Part B: Engineering, 43(8), 3231-3238.

Figure 2.13 Cross-sections of perforated sandwich panels (a) linear PVC (140 kg/m^3) and (b) PET (105 kg/m^3) [63].

2.6 Oblique (Non-normal) impact on composites and sandwich structures

In general terms, oblique impact involves an object travelling at an angle other than 90° to the surface on which impact occurs. Stronge [44] described an oblique collision whereby the relative velocity between the points of contact has a component that is tangential to the common tangent plane.

2.6.1 Background

Preliminary studies on oblique impact dates back as early as the 1950's, mainly using theoretical and/or analytical approaches [103-113]. An example in this subject area is the work by Zaid and Paul [103] in 1959, whereby a kinematic model in studying the oblique penetration of thin plates by a truncated conical indenter was proposed. Here, the classifications of the perforation process were made by considering several important aspects. These being (i) impact obliquity, which can be classified into three; that is low obliquity, high obliquity and very high obliquity , and (ii) the degree of perforation, which consist of four phases (Figure 2.15), as listed below:-

i. "Phase I (slug formation starts, petal elements begin to form) ;
ii. Phase II (slug has been completely formed, petals conform to the conical profile around entire periphery) ;
iii. Phase III (slug is partially or completely formed, petal formation continues, petal separation and possible petal rupture (spall) starts and ;
iv. Phase IV (petal formation has ended, petal separation and spall formation are well under way)".

Using this model, a complete velocity-displacement history was successfully generated.

Figure 2.14 Four phases of the degree of perforation [103].

2.6.2 Oblique impact at the low-velocity

In order to understand the effect of obliquity on damage development in composite structures; a number of researchers have carried out experimental studies at different energy levels under both low and high velocity impact, as highlighted in Table 2.1. Based on this study, only a single work is dedicated to studying the oblique impact response of composite structures at low-velocity; that is the work by Madjidi *et al*. [94].

In this study, the normal and oblique impact response of chopped strand mat (CSM) reinforced polyester laminates were studied at velocities up to 5.4 m/s. A simple expression was proposed to measure the imparted energy for the case of both normal and oblique impact, as illustrated in Figure 2.16.

Figure 2.15 (a) A schematic illustration of an impact event and; in (b) the associated system of forces [94].

For the case of a normal impact, where the specimen is impacted at 90° to its surface, the imparted energy, E_I is expressed by:-

$$E_I = \frac{1}{2} m\left(V_S{}^2 - V_R{}^2\right) \qquad 2.34$$

Table 2.1 Examples of experimental work on oblique impact response of composites.

Author(s)	**Year**	**Apparatus used to generate impact**	**Indenter materials & diameter**	**Target material**	**Inclination angle (°)**	**Velocity**
Madjidi *et al*. [94]	1996	Drop-tower	Steel (25.4mm)	CSM reinforced polyester laminates	0/5/10/15/20/ 25/30	0 - 5.42 m/s
Wiese *et al*. [86]	1998	Drop-tower	Steel	GFRP sandwich panels with PVC and balsa wood cores	30, 35 and 43	Up to 14.8 m/s
Ghaffari *et al*. [95]	1990	Gas gun	Aluminium alloy ball (12.7mm)	Carbon-epoxy laminate	10 - 60	30 – 73 m/s
Bouadi *et al*. [96]	1992	Gas gun	Aluminium alloy ball (12.7mm)	Carbon-epoxy laminate	0/15/30/ 45/60	38.10 – 69.28 m/s
López-Puente *et al*. [52]	2008	Gas gun	Tempered steel sphere (7.5 mm)	CFRP laminate	0 and 45	70 - 550 m/s
Hazell *et*.al [97]	2008	Gas-gun	Stainless steel (11.97)	CFRP laminate	0 and 45	170 – 374 m/s
Lamontagne *et al*. [113]	2001	Gas gun (Hyper-velocity)	Aluminium -(1.5mm) -(2.0mm)	Carbon fibre/ PEEK laminate	0/30/45	3,4,5 and 6 km/s

In contrast, for an oblique impact, the energy imparted to the test plate is given by:-

$$E_I = \frac{1}{2} m \left({V_S}^2 - {V_R}^2 \right) - U_R \qquad 2.35$$

Where E_I is the imparted energy, V_s is the striking velocity, V_R is the rebound velocity and U_R is the strain energy due to the deflection of the guide rods, as given in Equation 2.36.

$$U_R = \frac{1}{2K} (F_H)^2 \qquad 2.36$$

Where K is the transverse stiffness of the indenter and the guide rod assembly, which was measured experimentally and F_H is the horizontal force in the guide rod assembly. The values are plotted as a function of plate inclination, as shown in Figure 2.16.

This text box is where the unabridged thesis included the following third party copyright material:

Madjidi, S., Arnold, W. S., & Marshall, I. H. (1996). Damage tolerance of CSM laminates subject to low velocity oblique impacts. Composite Structures, 34 (1), 101-116.

Figure 2.16 Calculated strain (absorbed by guide rods) vs plate inclination angle following normal and oblique impact on chopped strand mat (CSM) reinforced polyester laminates [94].

Referring to Figure 2.16, assuming that all the kinetic energy travels in the vertical direction after impact, as in Equation 2.35, there is a significant force reaction horizontally. This horizontal force (transverse force) produces a horizontal deflection in the guide rod assembly. This absorbed strain energy has to be determined to establish the imparted energy during the impact event.

Therefore, assuming that the system of forces is in equilibrium,

$$\sum F_x = F_H - F_N \sin(\theta) + F_T \cos(\theta) = 0 \qquad 2.37$$

$$\sum F_y = F_s - F_T \sin(\theta) - F_N \cos(\theta) = 0 \qquad 2.38$$

Where F_s= striking force (measured by the force transducer during an impact test),

F_H = horizontal force in guide rod assembly = $(k_1 + k_2)\delta x = k\delta x$

F_N= normal or reaction force

F_T= friction or tangential force

θ = plate inclination angle

k =impacter unit stiffness in horizontal direction (measured experimentally)

δx= displacement in horizontal direction

Rewriting Equation 2.37 and substituting $F_T = \mu F_N$, i.e., it was assumed that F_T is a maximum at the point of slip:-

$$\therefore F_N = \frac{F_H}{\sin(\theta) - \mu \cos\theta} \quad 2.39$$

Here, the value of the coefficient of friction, μ, was taken as 0.30. Based on Equation 2.39, the calculated normal force for each inclination angle was plotted against the measured maximum depth of permanent indentation, as shown in Figure 2.17, showing a linear increase in the normal force with maximum depth of permanent indentation, up to approximately 0.2 mm, beyond which the value of the calculated normal force plateaued at approximately 2 kN, regardless of whether the panels were subjected to low or high obliquity, up to 30°.

Figure 2.17 Normal force vs maximum permanent indentation following normal and oblique impact on chopped strand mat (CSM) reinforced polyester laminates [94].

In addition, it was shown that the horizontal force is expressed as in Equation 2.40 below:-

$$F_H = F_S \tan(\theta) \quad 2.40$$

Madjidi *et al*. [94] also reported that the CSM reinforced polyester laminates impacted at a normal angle (θ = 0°) suffered much greater damage than obliquely-impacted laminates, at impact velocities up to 5.4 m/s. Over the range of impact energies and inclination angles considered in the study, it was observed that the damage area reduced with increasing angle of obliquity, as given in Figure 2.18.

This text box is where the unabridged thesis included the following third party copyright material:

Madjidi, S., Arnold, W. S., & Marshall, I. H. (1996). Damage tolerance of CSM laminates subject to low velocity oblique impacts. Composite Structures, 34 (1), 101-116.

Figure 2.18 Maximum gross damage area vs plate inclination angle following normal and oblique impact on chopped strand mat (CSM) reinforced polyester laminates [94].

2.6.3 Oblique impact response at high velocity

Wiese *et* al. [86] studied oblique impact damage in glass fibre-reinforced sandwich panels at 30°, 35° and 43° angles up to 6 kJ. A significant decrease in the critical impact energy (the energy level mid-way between the maximum and minimum

energy levels where penetration occurs) was observed, with increasing angle as shown in Figure 2.19 (a). However, a plot of normal velocity component versus impact angle suggests that the critical impact energy is almost independent of the impact angle and the tangential component of the velocity only has a small effect, as shown in Figure 2.19(b).

Figure 2.19 Experimental results showing (a) the variation of the critical impact energy vs. impact angle and (b) the impact energy associated with the normal impact velocity component vs. impact angle [86].

Ghaffari *et al*. [95] conducted an experimental and analytical investigation into the oblique impact response of carbon-epoxy laminates over a range of velocities from 30 to 73 m/s at various inclination angles, including 0°, 10°, 30° and 45°. At a given velocity, the damage area decreased with increasing angle of obliquity. Damage was most severe under normal impact. They concluded that for the range of impact velocities that cause non-visual damage, the normal component of the impact velocity was the principal factor in creating impact damage, whilst the tangential component only has a small effect.

In the study by Bouadi *et al*. [96], the normal and oblique impact response of carbon-epoxy laminates of differing thicknesses were investigated under low and high velocity impact. For oblique impact, the authors considered 15°, 30°, 45° and 60°

inclination angles using a gas gun apparatus, whilst normal impact tests were conducted using a drop-hammer apparatus. Two specimens each, with the same nominal thickness of 6.35 mm, were considered for these tests at different energy levels.

At low impact energies, an inverse linear relationship was observed between the inclination angle and the resulting damage area, while at medium and high impact energies, the response was more complex, as shown in Figure 2.21.

From 0° to 15°, there was a slow reduction in the damage area for a given impact energy. However, between 15° and 45°, the damage area rapidly increased with inclination angle. Between 45° and 60°, there was a reduction in the rate of decrease of damage area with increasing angle. Above 60°, it was assumed that the damage area tended asymptotically to zero, for the intermediate energy cases. From these findings, it was concluded that the damage area is linearly dependent on impact energy, even for oblique impact cases.

Lamontagne *et al*. [51] studied the effect of indenter density, impact angle and energy on the hypervelocity oblique impact response of carbon fibre/PEEK composite laminates for impact velocities between 2.71 to 7.14 km/s and impact angles of 0°, 30° and 45°. Here, a gas-gun facility was employed to conduct a series of hypervelocity impact tests. Based on the test results, it was reported that the entry and exit craters were approximately circular in shape, with some traces of fibres and matrix fracture in the region of the impact crater. Overall, it was concluded that damage is independent of indenter density, but greatly depends on the diameter of the indenter. In addition, the entry crater diameter was more dependent upon the

impact velocity than impact angle. For the case of normal impacts, the crater diameter increased with increasing velocity, as well as the corresponding energy. However, no clear trend was apparent with oblique incidence impacts. Examples of the images showing an impact and exit crater for 24-ply laminates using a 2-mm indenter is as shown in Figure 2.22.

This text box is where the unabridged thesis included the following third party copyright material:

Bouadi, H., Marple Jr, L. R., & Marshall, A. P. (1992). Normal and oblique impact damage on thick-section composite laminate. Recent Advances in the Structural Dynamic Modelling of Composite Rotor Blades and Thick Composites. ASME, 30, 157-169.

Figure 2.20 Damage area vs. incidence angle at low, intermediate and high energy levels, using 6.35-mm thick specimens [96].

This text box is where the unabridged thesis included the following third party copyright material:

Lamontagne, C. G., Manuelpillai, G. N., Taylor, E. A., & Tennyson, R. C. (1999). Normal and oblique hypervelocity impacts on carbon fibre/PEEK composites. International Journal of Impact Engineering, 23(1), 519-532.

Figure 2.21 Impact and exit craters for 24-ply carbon fibre/PEEK composite laminates, using 2-mm Al indenter [51].

2.6.4 Perforation of composite laminates and sandwich structures subjected to oblique impact

Hazell *et al*. [97] conducted a series of normal and oblique impact experiments on up to perforation on woven CFRP laminates using a steel sphere. The test-set-up is illustrated in Figure 2.23. It this study, they considered panels with nominal thicknesses of 3 mm and 6 mm. It was found that both the energy absorbed per unit thickness as well as the level of damage, in which perforation under both normal and oblique impact incidences was similar. These observations are presented in Figure 2.23 to Figure 2.25, for normal and oblique impact angles cases.

Figure 2.22 Schematic diagram of the normal and oblique impact test set-up [97].

Figure 2.23 The change in kinetic energy due to perforation of normal and oblique impact on carbon fibre reinforced epoxy laminates of different thicknesses [97].

his text box is where the unabridged thesis included the following third party copyright material:

Hazell, P. J., Kister, G., Stennett, C., Bourque, P., & Cooper, G. (2008). Normal and oblique penetration of woven CFRP laminates by a high velocity steel sphere. Composites Part A: applied science and manufacturing, 39 (5), 866-874.

Figure 2.24 Evaluation of the effective linear thickness offered to the indenter during normal and oblique penetration on carbon fibre reinforced epoxy laminates [97].

This text box is where the unabridged thesis included the following third party copyright material:

Hazell, P. J., Kister, G., Stennett, C., Bourque, P., & Cooper, G. (2008). Normal and oblique penetration of woven CFRP laminates by a high velocity steel sphere. Composites Part A: applied science and manufacturing, 39(5), 866-874.

Figure 2.25 Damage area measured by ultrasonic C-scan vs. impact energy for each of the impacted carbon fibre reinforced epoxy laminates [97].

Hazell *et al*. [50] extended the earlier work to study the response when using relatively thick woven CFRP laminates, with a nominal thickness of 12 mm formed by bonding together two 6-mm thick laminates, subjected to high velocity impact between 187 m/s and 1219 m/s. For the range of impact velocities used, it was reported that the obliquely- impacted panels did not show any significant difference in terms of the resistance to penetration, as shown in Figure 2.26 and Figure 2.27. For the case of the perforated panels, an ultrasonic C-Scan analysis showed similar damage pattern with the normally-impacted panels, for both the front and rear plates. In addition, the ballistic performance improved with increasing laminate thickness.

During oblique penetration, the rear plate showed deformation perpendicular to the plane of the laminate; as a result, this induced circular delamination pattern, whereas the front plate exhibited asymmetric damage.

Figure 2.26 Damage area as a function of impact energy following high velocity impact on woven CFRP laminates at normal incidence [50] .

Figure 2.27 Damage area as a function of impact energy following oblique impact on woven CFRP laminates [50].

Lopez-Puente *et al*.[52] studied the normal and oblique ballistic impact response of carbon/epoxy laminates at high velocity and impact angles of 0° and 45° using both experimental as well as numerical techniques. Examples of the damage observed for

both normal and oblique impact cases are given in Figure 2.29, which shows the cross-sections of the panels after impact) and secondly in Figure 2.30, images of bottom view of the panels following both normal and 45° impact loading are shown.

In addition, several conclusions were made and these include the following:-

i. below the ballistic limit: Normal and oblique impacts resulted in an increase in the damage with the indenter initial velocity. Above this limit, there was a reduction in damage with increasing impact velocity;
ii. normal impact resulted in the largest damage area at the ballistic limit; A rhomboidal failure pattern was observed in the laminate;
iii. above the ballistic limit, oblique impact resulted in larger areas of damage, due to a change in damage mechanisms;
iv. as an effect of the fibres at oblique angles, there was an increase in the ballistic limit. Also, above this limit, the residual velocity is unaffected by the impact obliquity.

Figure 2.28 Images of cross-sections of woven laminates impacted below the ballistic limit with an impact velocity of 92 m/s at (a) 0° and (b) 45° [52].

Figure 2.29 Bottom views of woven laminates impacted close to the ballistic limit, at different angles; (a) 0° and (b) 45° [52].

More recently, a finite element analysis, using ABAQUS/Explicit, was used to predict the response of the foam core panels and sandwich panels during impact by a steel indenter, and then to predict the effect of oblique impact on the perforation resistance of the sandwich panels [92]. Figure 2.31 shows the predicted load-displacement traces following normal and oblique impact on two types of polymer foam sandwich panels, fabricated using a cross-linked PVC (C130) and a rigid PET (T92.100). Here, the effect of foam core density on the resulting load-displacement traces of the panels is apparent, showing higher density foam sandwich panels with higher load values. For a given type of sandwich panel, the normal impact exhibits the highest maximum impact force. The corresponding perforation energy was found to increase with impact angle, (Figure 2.31).

This text box is where the unabridged thesis included the following third party copyright material:

Zhou, J., Hassan, M. Z., Guan, Z., & Cantwell, W. J. (2012). The low velocity impact response of foam-based sandwich panels. Composites Science and Technology, 72(14), 1781-1790.

Figure 2.30 Predicted load-displacement traces for sandwich panels fabricated using cross-linked PVC (C70.130) as well as PET (T92.100) subjected to oblique impact at angles of 0°, 10°, 20° and 30°[92].

This text box is where the unabridged thesis included the following third party copyright material:

Zhou, J., Hassan, M. Z., Guan, Z., & Cantwell, W. J. (2012). The low velocity impact response of foam-based sandwich panels. Composites Science and Technology, 72(14), 1781-1790.

Figure 2.31 The variation of perforation energy with impact angle for three sandwich structures [92].

In addition, further investigation was made of the damage evolution, with the focus on the perforated panels made with C70.130 cross-linked PVC and PET T92.105 PVC subjected to oblique impact at incident angles of 0°, 10°, 20° and 30°, respectively. The cross-sections shown in

Figure 2.32 revealed that impact occurring at the highest angle of inclination resulted in greater surface area using a simple geometric analysis. Here, it was assumed that

the indenter creates an elliptic entrance hole on the top surface of the target. Therefore, to quantify for the changes in terms of surface area as well as volume increased from normal impact perforation to oblique impact perforation, the ratio of the surface area of an elliptic oblique cylinder to that of a normal cylinder is expressed as in Equation 2.41 below:-

$$\frac{\sqrt{\frac{1}{2}}(r^2 + R^2)}{\mathrm{r}\cos(I)} \qquad 2.41$$

Where r is the radius of the right cylinder, R is the long radius of the elliptical oblique cylinder and I is the angle between the normal cylinder and the elliptical oblique cylinder.

Also, the ratio of the volume of an elliptic oblique cylinder to that of a normal cylinder is expressed as in Equation 2.42 below:-

$$\frac{1}{\cos(I)} - 1 \qquad 2.42$$

Based on this approach, with the assumptions that energy is dissipated in shearing both the composite and the foam around the perimeter of the indenter, as well as crushing the foam ahead of the indenter, they argued that the change in perforation energy associated with increasing impact angle is a combination of both equations as above. Therefore, the calculated increase in surface area was found to be approximately 25% passing from normal to 30° impact. Similarly, the volume of the total area also increased 16%, passing from normal impact (0°) to 30° [92].

Figure 2.32 Predicted cross-sections of sandwich panels made with C70.130 cross-linked PVC and PET T92.105 PVC subjected to oblique impact at incident angles of 0°, 10°, 20° and 30°, respectively [92].

2.7 Summary of Literature Review

In this chapter, a review of relevant past and current research work on composites and sandwich structures subjected to normal and oblique impact has been discussed, with the focus on low-velocity impact. A brief overview of the impact response classifications, impact generations as well as some of the available impact models relating to impact dynamics are given. Other important aspects such as contact mechanics, impact damage in composites and sandwich structures, damage

prediction, residual properties as well as perforation behaviour of the composites and sandwich structures have been reviewed, with some relevant examples. Lastly, the oblique impact response of composites and sandwich structures has been discussed, with examples of published experimental and numerical work. To-date, limited information is available in the literature on this subject area, particularly in studying the low-velocity oblique impact response of composites and sandwich structures.

Hence, this research work aims to contribute to the understanding of the oblique impact response of laminated composites and foam-based sandwich structures in the low velocity range, from damage initiation up to full perforation, for selected number of structures. A suitable model is sought to predict the response dynamically, with a comparison of the static behaviour of the structures at various impact angles.

2.8 References

[1] Cantwell, W. J., Curtis, P. T., & Morton, J. (1986). An assessment of the impact performance of CFRP reinforced with high-strain carbon fibres. Composites Science and Technology, 25(2), 133-148.

[2] Cantwell, W. J., & Morton, J. (1989). Comparison of the low and high velocity impact response of CFRP. Composites, 20(6), 545-551.

[3] Cantwell, W. J., & Morton, J. (1990). Impact perforation of carbon fibre reinforced plastic. Composites Science and technology, 38(2), 119-141.

[4] Cantwell, W. J., & Morton, J. (1989). The influence of varying indenter mass on the impact response of CFRP. Composite Structures, 13(2), 101-114.

[5] Cantwell, W. J., & Morton, J. (1991). The impact resistance of composite materials—A review. Composites, 22(5), 347-362.

[6] Caprino, G., Crivelli Visconti, I., & Di Ilio, A. (1984). Elastic behaviour of composite structures under low velocity impact. Composites, 15(3), 231-234.

[7] Yang, F. J., & Cantwell, W. J. (2010). Impact damage initiation in composite materials. Composites Science and Technology, 70(2), 336-342.

[8] Abrate, S. (1991). Impact on laminated composite materials. Applied Mechanics Reviews, 44(4), 155-190.

[9] Abrate, S. (1994). Impact on laminated composites: recent advances. Applied Mechanics Reviews, 47(11), 517-544.

[10] Abrate, S. (2001). Modelling of impacts on composite structures. Composite Structures, 51(2), 129-138.

[11] Abrate, S. (2005). Impact on composite structures. Cambridge University Press.

[12] Lee, S. M., & Zahuta, P. (1991). Instrumented impact and static indentation of composites. Journal of Composite Materials, 25(2), 204-222.

[13] Lee, S. W., & Sun, C. T. (1993). Dynamic penetration of graphite/epoxy laminates impacted by a blunt-ended indenter. Composites Science and Technology, 49(4), 369-380.

[14] Mitrevski, T., Marshall, I. H., Thomson, R., Jones, R., & Whittingham, B. (2005). The effect of indenter shape on the impact response of composite laminates. Composite Structures, 67(2), 139-148.

[15] Morita, H., Adachi, T., Tateishi, Y., & Matsumot, H. (1997). Characterization of impact damage resistance of CF/PEEK and CF/toughened epoxy laminates under low and high velocity impact tests. Journal of Reinforced Plastics and Composites, 16(2), 131-143.

[16] Naik, N. K., Chandra Sekher, Y., & Meduri, S. (2000). Damage in woven-fabric composites subjected to low-velocity impact. Composites Science and Technology, 60(5), 731-744.

[17] Olsson, R. (2000). Mass criterion for wave controlled impact response of composite plates. Composites Part A: Applied Science and Manufacturing, 31(8), 879-887.

[18] Reyes Villanueva, G., & Cantwell, W. J. (2004). The high velocity impact response of composite and FML-reinforced sandwich structures. Composites Science and Technology, 64(1), 35-54.

[19] Richardson, M. O. W., & Wisheart, M. J. (1996). Review of low-velocity impact properties of composite materials. Composites Part A: Applied Science and Manufacturing, 27(12), 1123-1131.

[20] Robinson, P., & Davies, G. A. O. (1992). Indenter mass and specimen geometry effects in low velocity impact of laminated composites. International Journal of Impact Engineering, 12(2), 189-207.

[21] Abdullah, M. R., & Cantwell, W. J. (2006). The impact resistance of polypropylene-based fibre–metal laminates. Composites Science and Technology, 66(11), 1682-1693.

[22] Buitrago, B. L., García-Castillo, S. K., & Barbero, E. (2010). Experimental analysis of perforation of glass/polyester structures subjected to high-velocity impact. Materials Letters, 64(9), 1052-1054.

[23] Cantwell, W. J. (2007). Geometrical effects in the low velocity impact response of GFRP. Composites Science and Technology, 67(9), 1900-1908.

[24] Chenghong, H., Yubin, L., Zuoguang, Z., & Zhijie, S. (2008). Impact damage modes and residual flexural properties of composites beam. Journal of Reinforced Plastics and Composites.

[25] Choi, H. Y., Downs, R. J., & Chang, F. K. (1991). A new approach toward understanding damage mechanisms and mechanics of laminated composites due to low-velocity impact: Part I—Experiments. Journal of Composite Materials, 25(8), 992-1011.

[26] Christoforou, A. P., & Yigit, A. S. (2009). Scaling of low-velocity impact response in composite structures. Composite Structures, 91(3), 358-365.

[27] Christoforou, A. P., Yigit, A. S., Cantwell, W. J., & Yang, F. (2010). Impact response characterization in composite plates—experimental validation. Applied Composite Materials, 17(5), 463-472.

[28] Davies, G. A. O., & Zhang, X. (1995). Impact damage prediction in carbon composite structures. International Journal of Impact Engineering, 16(1), 149-170.

[29] Evci, C., & Gülgeç, M. (2012). An experimental investigation on the impact response of composite materials. International Journal of Impact Engineering, 43, 40-51.

[30] Fan, J., Cantwell, W. J., & Guan, Z. W. (2011). The low-velocity impact response of fiber-metal laminates. Journal of Reinforced Plastics and Composites, 30(1), 26-35.

[31] Fan, J., Guan, Z., & Cantwell, W. J. (2011). Modelling perforation in glass fiber reinforced composites subjected to low velocity impact loading. Polymer Composites, 32(9), 1380-1388.

[32] He, T., Wen, H. M., & Qin, Y. (2007). Penetration and perforation of FRP laminates struck transversely by conical-nosed indenters. Composite Structures, 81(2), 243-252.

[33] Hitchen, S. A., & Kemp, R. M. J. (1995). The effect of stacking sequence on impact damage in a carbon fibre/epoxy composite. Composites, 26(3), 207-214.

[34] Icten, B. M., Kıral, B. G., & Deniz, M. E. (2013). Indenter diameter effect on low velocity impact response of woven glass epoxy composite plates. Composites Part B: Engineering, 50, 325-332.

[35] Im, K. H., Cha, C. S., Kim, S. K., & Yang, I. Y. (2001). Effects of temperature on impact damages in CFRP composite laminates. Composites Part B: Engineering, 32(8), 669-682.

[36] Kumar, P., & Rai, B. (1991). Impact damage on single interface GFRP laminates—an experimental study. Composite Structures, 18(1), 1-10.

[37] Liu, D. (1990). Delamination resistance in stitched and unstitched composite plates subjected to impact loading. Journal of Reinforced Plastics and Composites, 9(1), 59-69.

[38] Lopes, C. S., Seresta, O., Coquet, Y., Gürdal, Z., Camanho, P. P., & Thuis, B. (2009). Low-velocity impact damage on dispersed stacking sequence laminates. Part I: Experiments. Composites Science and Technology, 69(7), 926-936.

[39] Mines, R. A. W., Roach, A. M., & Jones, N. (1999). High velocity perforation behaviour of polymer composite laminates. International Journal of Impact Engineering, 22(6), 561-588.

[40] Shivakumar, K. N., Elber, W., & Illg, W. (1985). Prediction of impact force and duration due to low-velocity impact on circular composite laminates. Journal of Applied Mechanics, 52(3), 674-680.

[41] Shyr, T. W., & Pan, Y. H. (2003). Impact resistance and damage characteristics of composite laminates. Composite Structures, 62(2), 193-203.

[42] Sierakowski, R. L., & Chaturvedi, S. K. (1997). Dynamic loading and characterization of fiber-reinforced composites. Wiley-VCH, February 1997.

[43] Strait, L. H., Karasek, M. L., & Amateau, M. F. (1992). Effects of stacking sequence on the impact resistance of carbon fiber reinforced thermoplastic toughened epoxy laminates. Journal of Composite Materials, 26(12), 1725-1740.

[44] Stronge, W. J. (2004). Impact mechanics. Cambridge University Press.

[45] Sutherland, L. S., & Soares, C. G. (2005). Contact indentation of marine composites. Composite structures, 70(3), 287-294.

[46] Tan, C. Y., & Akil, H. M. (2012). Impact response of fiber metal laminate sandwich composite structure with polypropylene honeycomb core. Composites Part B: Engineering, 43(3), 1433-1438.

[47] Wen, H. M. (2000). Predicting the penetration and perforation of FRP laminates struck normally by indenters with different nose shapes. Composite Structures, 49(3), 321-329.

[48] Whisler, D., & Kim, H. (2012). Effect of indenter radius on low-velocity impact damage of glass/epoxy composites. Journal of Composite Materials, 46(25), 3137-3149.

[49] Wu, E., & Shyu, K. (1993). Response of composite laminates to contact loads and relationship to low-velocity impact. Journal of Composite Materials, 27(15), 1443-1464.

[50] Hazell, P. J., Appleby-Thomas, G. J., & Kister, G. (2010). Impact, penetration, and perforation of a bonded carbon-fibre-reinforced plastic composite panel by a high-velocity steel sphere: an experimental study. The Journal of Strain Analysis for Engineering Design, 45(6), 439-450.

[51] Lamontagne, C. G., Manuelpillai, G. N., Taylor, E. A., & Tennyson, R. C. (1999). Normal and oblique hypervelocity impacts on carbon fibre/PEEK composites. International Journal of Impact Engineering, 23(1), 519-532.

[52] López-Puente, J., Zaera, R., & Navarro, C. (2008). Experimental and numerical analysis of normal and oblique ballistic impacts on thin carbon/epoxy woven laminates. Composites Part A: Applied Science and Manufacturing, 39(2), 374-387.

[53] Abrate, S. (1997). Localized impact on sandwich structures with laminated facings. Applied Mechanics Reviews, 50(2), 69-82.

[54] Akil Hazizan, M., & Cantwell, W. J. (2002). The low velocity impact response of foam-based sandwich structures. Composites Part B: Engineering, 33(3), 193-204.

[55] Aktay, L., Johnson, A. F., & Holzapfel, M. (2005). Prediction of impact damage on sandwich composite panels. Computational Materials Science, 32(3), 252-260.

[56] Anderson, T., & Madenci, E. (2000). Experimental investigation of low-velocity impact characteristics of sandwich composites. Composite Structures, 50(3), 239-247.

[57] Atas, C., & Sevim, C. (2010). On the impact response of sandwich composites with cores of balsa wood and PVC foam. Composite Structures, 93(1), 40-48.

[58] Chai, G. B., & Zhu, S. (2011). A review of low-velocity impact on sandwich structures. Proceedings of the Institution of Mechanical Engineers, Part L: Journal of Materials Design and Applications, 225(4), 207-230.

[59] Fatt, H., & Park, K. S. (2000). Perforation of honeycomb sandwich plates by indenters. Composites Part A: Applied Science and Manufacturing, 31(8), 889-899.

[60] Foo, C. C., Chai, G. B., & Seah, L. K. (2008). A model to predict low-velocity impact response and damage in sandwich composites. Composites Science and Technology, 68(6), 1348-1356.

[61] Gustin, J., Joneson, A., Mahinfalah, M., & Stone, J. (2005). Low velocity impact of combination Kevlar/carbon fiber sandwich composites. Composite Structures, 69(4), 396-406.

[62] Hassan, M., & Cantwell, W. J. (2011). Strain rate effects in the indentation behaviour of foam-based sandwich structures. Journal of Composite Materials, 46(10):1191-1199.

[63] Hassan, M. Z., & Cantwell, W. J. (2012). The influence of core properties on the perforation resistance of sandwich structures–An experimental study. Composites Part B: Engineering, 43(8), 3231-3238.

[64] Hassan, M. Z. (2012). The low velocity impact response of sandwich structures (Doctoral dissertation, The University of Liverpool).

[65] Hazizan, M. A., & Cantwell, W. J. (2003). The low velocity impact response of an aluminium honeycomb sandwich structure. Composites Part B: Engineering, 34(8), 679-687.

[66] Fatt, H., & Park, K. S. (2001). Dynamic models for low-velocity impact damage of composite sandwich panels-Part B: Damage initiation. Composite Structures, 52(3), 353-364.

[67] Hou, W., Zhu, F., Lu, G., & Fang, D. N. (2010). Ballistic impact experiments of metallic sandwich panels with aluminium foam core. International Journal of Impact Engineering, 37(10), 1045-1055.

[68] Kanny, K., Mahfuz, H., Carlsson, L. A., Thomas, T., & Jeelani, S. (2002). Dynamic mechanical analyses and flexural fatigue of PVC foams. Composite Structures, 58(2), 175-183.

[69] Kepler, J. (2004). Impact Penetration of Sandwich Panels at Different Velocities-An Experimental Parameter Study: Part I-Parameters and Results. Journal of Sandwich Structures and Materials, 6(4), 357-374.

[70] Lin, C., & Fatt, M. S. H. (2005). Perforation of sandwich panels with honeycomb cores by hemispherical nose indenters. Journal of Sandwich Structures and Materials, 7(2), 133-172.

[71] Lin, C., & Fatt, M. S. H. (2006). Perforation of composite plates and sandwich panels under quasi-static and indenter loading. Journal of Composite Materials, 40(20), 1801-1840.

[72] Hoo Fatt, M. S., & Park, K. S. (2001). Dynamic models for low-velocity impact damage of composite sandwich panels–Part A: Deformation. Composite structures, 52(3), 335-351.

[73] Mines, R. A. W., Worrall, C. M., & Gibson, A. G. (1998). Low velocity perforation behaviour of polymer composite sandwich panels. International Journal of Impact Engineering, 21(10), 855-879.

[74] Navarro, P., Abrate, S., Aubry, J., Marguet, S., & Ferrero, J. F. (2013). Analytical modelling of indentation of composite sandwich beam. Composite Structures, 100, 79-88.

[75] Nemes, J. A., & Simmonds, K. E. (1992). Low-velocity impact response of foam-core sandwich composites. Journal of Composite Materials, 26(4), 500-519.

[76] Othman, A. R., & Barton, D. C. (2008). Failure initiation and propagation characteristics of honeycomb sandwich composites. Composite Structures, 85(2), 126-138.

[77] Raju, K. S., Smith, B. L., Tomblin, J. S., Liew, K. H., & Guarddon, J. C. (2008). Impact damage resistance and tolerance of honeycomb core sandwich panels. Journal of Composite Materials, 42(4), 385-412.

[78] Reddy, T. Y., Wen, H. M., Reid, S. R., & Soden, P. D. (1998). Penetration and perforation of composite sandwich panels by hemispherical and conical indenters. Journal of Pressure Vessel Technology, 120(2), 186-194.

[79] Wen, H. M., Reddy, T. Y., Reid, S. R., & Soden, P. D. (1997). Indentation, penetration and perforation of composite laminate and sandwich panels under quasi-static and indenter loading. Key Engineering Materials, 141, 501-552.

[80] Rizov, V., Shipsha, A., & Zenkert, D. (2005). Indentation study of foam core sandwich composite panels. Composite Structures, 69(1), 95-102.

[81] Schubel, P. M., Luo, J. J., & Daniel, I. M. (2005). Low velocity impact behaviour of composite sandwich panels. Composites Part A: Applied Science and Manufacturing, 36(10), 1389-1396.

[82] Schubel, P. M., Luo, J. J., & Daniel, I. M. (2007). Impact and post impact behaviour of composite sandwich panels. Composites Part A: Applied Science and Manufacturing, 38(3), 1051-1057.

[83] Shipsha, A., Hallström, S., & Zenkert, D. (2003). Failure mechanisms and modelling of impact damage in sandwich beams-a 2D approach: part I-experimental investigation. Journal of Sandwich Structures and Materials, 5(1), 7-31.

[84] Shipsha, A., & Zenkert, D. (2005). Compression-after-impact strength of sandwich panels with core crushing damage. Applied Composite Materials, 12(3-4), 149-164.

[85] Shuaeib, F. M., & Soden, P. D. (1997). Indentation failure of composite sandwich beams. Composites Science and Technology, 57(9), 1249-1259.

[86] Wiese, M., & Hayman, B. (1998). Evaluation of oblique impact damage on sandwich panels with PVC and balsa core materials. In Fourth International Conference on Sandwich Construction. (pp. 807-18). Stockholm, Sweden.

[87] Xia, F., & Wu, X. Q. (2010). Work on impact properties of foam sandwich composites with different structure. Journal of Sandwich Structures and Materials, 12(1), 47-62.

[88] Yang, F. J., Hassan, M. Z., Cantwell, W. J., & Jones, N. (2013). Scaling effects in the low velocity impact response of sandwich structures. Composite Structures, 99, 97-104.

[89] Zhao, H., Elnasri, I., & Girard, Y. (2007). Perforation of aluminium foam core sandwich panels under impact loading—An experimental study. International Journal of Impact Engineering, 34(7), 1246-1257.

[90] Zhou, J., Guan, Z. W., & Cantwell, W. J. (2012). The perforation resistance of sandwich structures subjected to low velocity indenter impact loading. Aeronautical Journal, 116(1186), 1247-1262.

[91] Zhou, J., Guan, Z. W., & Cantwell, W. J. (2013). The impact response of graded foam sandwich structures. Composite Structures, 97, 370-377.

[92] Zhou, J., Hassan, M. Z., Guan, Z., & Cantwell, W. J. (2012). The low velocity impact response of foam-based sandwich panels. Composites Science and Technology, 72(14), 1781-1790.

[93] Zhu, S., & Chai, G. B. (2013). Damage and failure mode maps of composite sandwich panel subjected to quasi-static indentation and low velocity impact. Composite Structures, 101, 204-214.

[94] Madjidi, S., Arnold, W. S., & Marshall, I. H. (1996). Damage tolerance of CSM laminates subject to low velocity oblique impacts. Composite Structures, 34(1), 101-116.

[95] Ghaffari, S., Tan, T. M., & Awerbuch, J. (1990, November). An experimental and analytical investigation on the oblique impact of graphite/epoxy laminates. In 22nd International SAMPE Technical Conference, November.

[96] Bouadi, H., Marple Jr, L. R., & Marshall, A. P. (1992). Normal and oblique impact damage on thick-section composite laminate. Recent Advances in the Structural Dynamic Modelling of Composite Rotor Blades and Thick Composites. ASME, 30, 157-169.

[97] Hazell, P. J., Kister, G., Stennett, C., Bourque, P., & Cooper, G. (2008). Normal and oblique penetration of woven CFRP laminates by a high velocity steel sphere. Composites Part A: applied science and manufacturing, 39(5), 866-874.

[98] Zaera, R., & Sánchez-Gálvez, V. (1998). Analytical modelling of normal and oblique ballistic impact on ceramic/metal lightweight armours. International Journal of Impact Engineering, 21(3), 133-148.

[99] Zhou, D. W., & Stronge, W. J. (2008). Ballistic limit for oblique impact of thin sandwich panels and spaced plates. International journal of impact engineering, 35(11), 1339-1354.

[100] Frantziskonis, G. (1988). Distributed damage in composites, theory and verification. Composite Structures, 10(2), 165-184.

[101] Gunnink, J. W. (1988). Damage tolerance and supportability aspects of ARALL laminate aircraft structures. Composite Structures, 10(1), 83-104.

[102] Bull, P. H., & Edgren, F. (2004). Compressive strength after impact of CFRP-foam core sandwich panels in marine applications. Composites Part B: Engineering, 35(6), 535-541.

[103] Zaid, M., & Paul, B. (1959). Oblique perforation of a thin plate by a truncated conical indenter. Journal of the Franklin Institute, 268(1), 24-45.

[104] Davids, N., & Lawhead, W. (1965). Transient analysis of oblique impact on plates. Journal of the Mechanics and Physics of Solids, 13(4), 199-212.

[105] Maw, N., Barber, J. R., & Fawcett, J. N. (1976). The oblique impact of elastic spheres. Wear, 38(1), 101-114.

[106] Maw, N. J. R. J. N., Barber, J. R., & Fawcett, J. N. (1977). The rebound of elastic bodies in oblique impact. Mechanics Research Communications, 4(1), 17-22.

[107] Awerbuch, J., & Bodner, S. R. (1977). An investigation of oblique perforation of metallic plates by indenters. Experimental Mechanics, 17(4), 147-153.

[108] Jonas, G. H., & Zukas, J. A. (1978). Mechanics of penetration: analysis and experiment. International Journal of Engineering Science, 16(11), 879-903.

[109] Virostek, S. P., Dual, J., & Goldsmith, W. (1987). Direct force measurement in normal and oblique impact of plates by indenters. International Journal of Impact Engineering, 6(4), 247-269.

[110] Lewis, A. D., & Rogers, R. J. (1988). Experimental and numerical study of forces during oblique impact. Journal of Sound and Vibration, 125(3), 403-412.

[111] Rogers, R. J., & Lewis, A. D. (1990). Further numerical studies of oblique elastic impact. Journal of Sound and Vibration, 141(3), 507-510.

[112] Sundararajan, G. (1990). The energy absorbed during the oblique impact of a hard ball against ductile target materials. International Journal of Impact Engineering, 9(3), 343-358.

[113] Lamontagne, C. G., Manuelpillai, G. N., Kerr, J. H., Taylor, E. A., Tennyson, R. C., & Burchell, M. J. (2001). Indenter density, impact angle and energy effects on hypervelocity impact damage to carbon fibre/peek composites. International Journal of Impact Engineering, 26(1), 381-398.

CHAPTER III: EXPERIMENTAL PROCEDURE

This chapter describes the material properties and specimen preparation as well as the experimental testing involved in studying the dynamic and static response of laminated composites and sandwich foam structures. The material properties are those quoted in the materials supplier's data sheets. The experimental testing program considered in this study includes both dynamic and static testing. In addition, to characterize the mechanisms of damage initiation and propagation in the fibre-reinforced epoxy laminates and the sandwich foam panels, visual observations and optical microscopy of the impacted panels were carried out.

3.0 Experimental Procedure

3.1 Skin Materials

Plain composites, as well as the top and bottom facings of the sandwich foam panels, were fabricated using SE84 unidirectional (E-glass) fibre reinforced epoxy resin prepreg supplied by Umeco Plc (formerly known as Advanced Composites Group (ACG) Ltd). This material can be cured at temperatures between 80°C and 120°C. Among the main features of this material are its excellent controllable flow and tack characteristics. Table 3.1 lists the mechanical properties of this material in the form of a prepreg.

Table 3.1 Mechanical Properties of UD SE84 glass fibre-reinforced prepreg [1]

Mechanical Properties	**Value**
Tensile Strength	1257 MPa
Tensile Modulus	47 GPa
Interlaminar Shear Strength	83 MPa
Compressive Strength	1258 MPa
Compressive Modulus	56 GPa
Cured Ply Thickness	0.18 mm
Fibre Weight	300 g/m^2
Prepreg Areal Weight	476 g/m^2

3.2 Core Materials

In this study, the sandwich panels were constructed using two types of polymeric foam, that is linear PVC foams (AIREX®R63.80 and R63.140); and two PET polymer foams (AIREX®T92.100 and T92.130). This yielded sandwich panels based on core materials with four different densities.

3.2.1 Foam materials

3.2.1.1 Linear PVC foams

AIREX®R63, supplied by Alcan Composites, is a closed-cell, linear, thermoplastic foam with an extremely high damage tolerance. This rigid polymeric foam is based on poly (vinyl chloride) (PVC), co-polymerized with methyl methacrylate and foamed using non-ozone depleting blowing agents [2]. The physical and chemical properties of AIREX®63 are as shown in Table 3.2, whilst the general properties are tabulated in Table 3.3.

Table 3.2 Physical and chemical properties of the AIREX®R63 foams [2].

Physical state/form	**Polymer foam sheet with a visible cell structure**
Colour	Yellow
Glass transition temperature	55 to 60°C
Apparent nominal density (kg/m^3)	60
Decomposition temperature	>180°C
Flash ignition temperature	310°C
Density	50-160kg/m^3
Solubility: Insoluble in Soluble in	 Water, sea water, acids, alkalis, aliphatic hydrocarbons Organic solvents such as aromatic hydrocarbons, ketones, chlorinated hydrocarbons

Table 3.3 Selected properties of the AIREX®R63 foams [2].

Typical properties for AIREX®R63	**R63.80**	**R63.140**
Nominal apparent density (kg/m^3)	90	140
Compressive strength perpendicular to the plane (MPa)	0.90	1.6
Compressive modulus perpendicular to plane (MPa)	56	110
Tensile strength in the plane (MPa)	1.4	2.4
Tensile modulus in the plane (MPa)	50	90
Shear strength (MPa)	1.0	1.85
Shear modulus (MPa)	21	37
Shear elongation at break (%)	75	80
Impact strength (kJ/m^2)	5.0	6.5
Thermal conductivity at room temperature (W/m.K.)	0.037	0.039
Colour	Brownish Yellow	Brownish Yellow

3.2.1.2 PET Foams

AIREX®T92 is rigid polymeric foam based on poly (ethylene terephthalate) (PET). It is closed-cell thermoplastic, polymer foam with very good mechanical properties. This material is suitable as a core material for a variety of lightweight sandwich structures that are subjected to static and dynamic loads. The foam can be exposed to elevated temperatures during the manufacturing process. Selected physical and chemical properties, as well as mechanical properties of the AIREX® T92.100 and T92.130, are listed in Table 3.4 and Table 3.5 respectively.

Table 3.4 Physical and chemical properties of AIREX®T92.100 and T92.130 foams [3].

Physical state/form	**Polymer foam sheet with a visible cell structures**
Colour	White
Melting temperature	250°C
Decomposition temperature	>340°C
Flash ignition temperature	370°C
Density	100-320 kg/m^3
Solubility: Insoluble in Soluble in	 Water, sea water, acids, alkali and aliphatic hydrocarbons aromatic hydrocarbons, ketones, chlorinated hydrocarbons

Table 3.5 Selected mechanical properties of AIREX®T92.100 and T92.130 [3].

Typical properties for AIREX®T92	**T92.100**	**T92.130**
Nominal apparent density (kg/m^3)	115	135
Compressive strength perpendicular to the plane (N/mm^2)	1.8	2.4
Compressive modulus perpendicular to plane (N/mm^2)	110	140
Tensile strength in the plane (N/mm^2)	2.9	3.3
Tensile modulus in the plane (N/mm^2)	145	175
Shear strength (N/mm^2)	1.05	1.3
Shear modulus (N/mm^2)	23	30
Shear elongation at break (%)	15	12
Thermal conductivity at room temperature (W/m.K.)	0.035	0.036

3.3 Materials Preparation

3.3.1 Preparation of the composite plates and skin materials

Individual plies of the glass fibre reinforced epoxy prepreg, with dimensions of 300 mm x 300 mm, were cut using a sharp razor blade. The plies were then stacked with a stacking sequence of $[0/90/0/90]_s$ in a picture mould frame with an opening of 300 mm x 300 mm, as illustrated in Figure 3.1. The top surfaces of the picture frame mould were covered with a layer of Teflon tape for ease of demoulding after curing. The laminates were then cured in a hot press at a curing temperature, T_s of 125±5 °C, with a dwell time of 60 minutes, before cooling down to room temperature, T_R at a cooling rate of less than 10°C per minute as illustrated in Figure 3.2. The nominal thickness of the cured panels was 2.0 ± 0.1 mm for the 8-ply laminate.

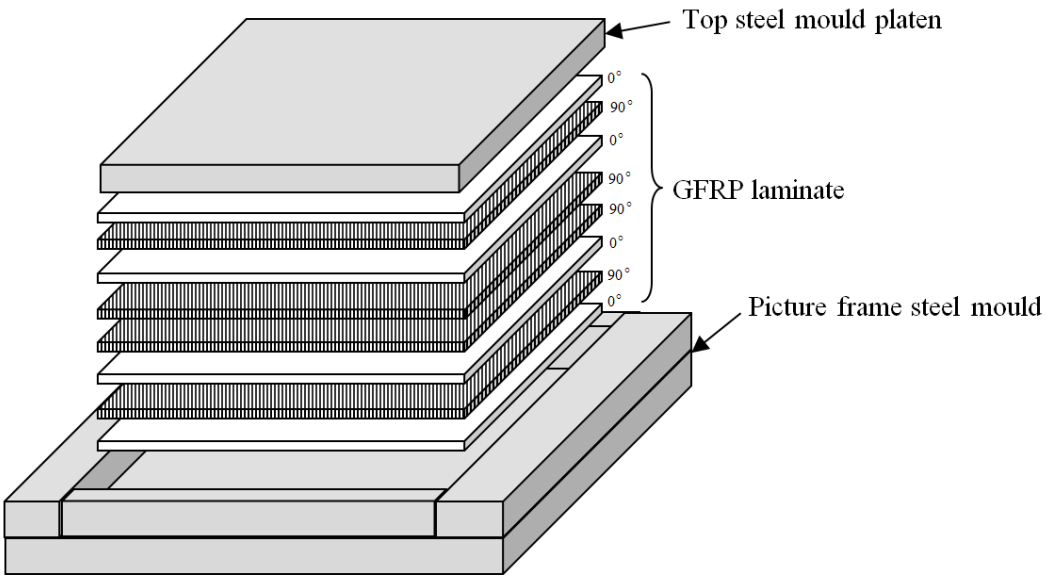

Figure 3.1 Illustration of the stacking sequence for an 8-ply composite laminate.

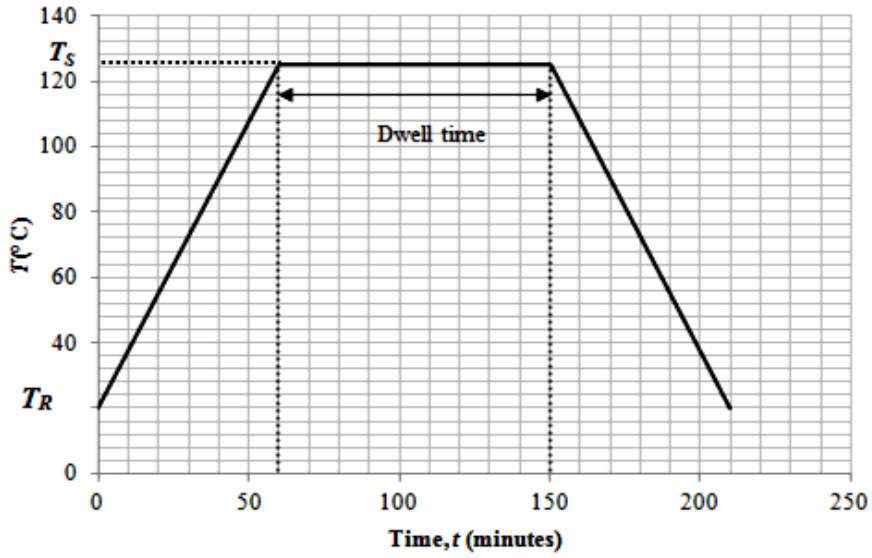

Figure 3.2 Curing profile for the glass fibre-reinforced composites (SE84).

3.3.2 Preparation of the core materials

The four foams described in Section 3.2 were cut to the same dimensions as the facing skins using a circular saw. Care was taken when cutting the brittle core materials in order to avoid introducing damage to the edges of the panels. The final dimensions of the core materials were 150 mm x 150 mm, with nominal thicknesses of 20 ± 0.1 mm, as shown in Figure 3.3.

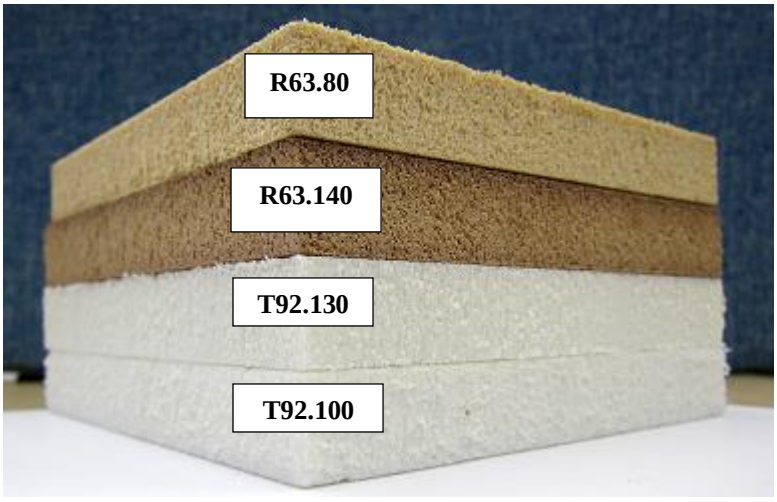

Figure 3.3 Polymeric foam core materials used in the sandwich constructions.

3.3.3 Fabrication of the foam-core sandwich panels

The facings of the sandwich structures were manufactured using four plies of glass-fibre reinforced epoxy with a stacking sequence of $[0/90]_s$ giving a cured thickness of 1.0 ± 0.05 mm for both the upper and lower facings. The laminates were then placed on either side of the foam core, as illustrated in Figure 3.4 without the use of an adhesive film. The uncured sandwich assembly was then placed between two steel plates before curing under a pressure of 1.25 bars in a hot press. The hot press was then set to a temperature, T_s of 80° ± 5°C for a dwell time of 90 minutes before slow cooling to room temperature. The nominal cured thickness of the sandwich panels were approximately 20 mm.

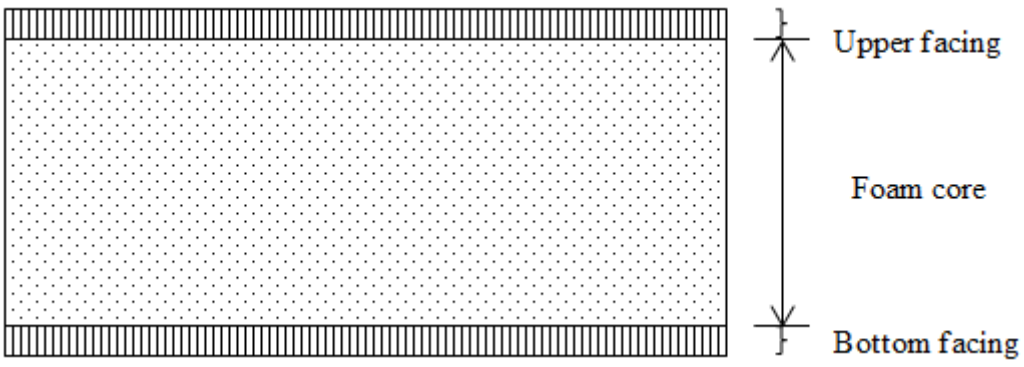

Figure 3.4 Schematic of a sandwich foam structure assembly.

3.4 Low Velocity Impact Testing

The impact response of the composite panels and sandwich structures were assessed using an instrumented drop-weight impact rig as illustrated in Figure 3.5. A 5.6 kg-carriage of impact was used in order to yield range energies to characterize the impact response of the structures at normal and oblique angles. A 12-mm diameter steel hemispherical indenter was used to strike the panels.

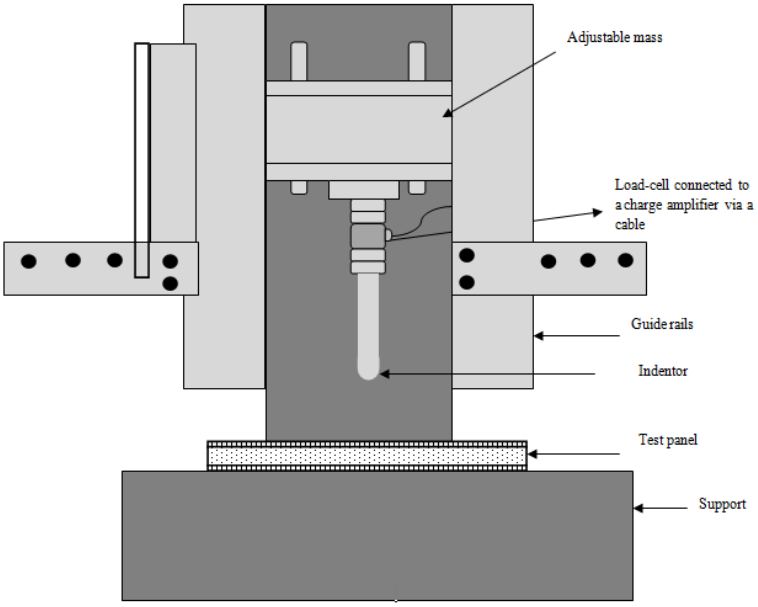

Figure 3.5 A schematic diagram illustrating the instrumented drop-weight test assembly, showing the indenter connected to the load-cell and the mass between two guide rails.

To capture the load-time traces during the impact event, a piezoelectric load-cell, supplied by Kistler (type 9321A), was connected to a Kistler charge-amplifier (type 5011) using an insulated coaxial cable. The load-cell was placed under the impact carriage. The signals from the load-cell were amplified and filtered using a Kistler charge amplifier. This was connected to a data logger that is connected to a workstation, where the data were captured and stored. A photograph showing an oblique impact test set-up is given in Figure 3.6. The original output was in volts,

which was then converted to load (N) using the calibration factor supplied by the manufacturer, and given in Table 3.6.

Figure 3.6 The Instrumented drop-weight impact test set-up for oblique impact testing (20° inclination).

Table 3.6 Important settings for the Kistler charge amplifier

Transducer sensitivity	3.97 ρC/N
Scaling	3.97 E+03
Maximum load	10 kN

A high-speed camera, with details as given in Table 3.7, was used to capture the displacement-time traces during each impact test. The original video files were analysed using the ProAnalyst software, where it was calibrated and processed, from the information in pixels to the desired parameter required, such as distance, y-displacement, x-displacement, x-velocity and y-velocity of the indenter. This study considered the displacement of the indenter in the y-direction for normal impact, whereas for non-normal impact events, the x-displacement was also considered to

account for the indenter movement due to the reaction forces in the horizontal direction. An example of the interface in the ProAnalyst software is shown in Figure 3.7.

Table 3.7 Details of the high-speed camera system.

Part	**Feature**
Camera- Motion Pro X4	Make: Integrated Design Tools, Inc. M/N: X4C-U-4
ProAnalyst Software	Make: Xcitex
	Edition: Professional
	Version: Workstation
	Registration Code: 13146-7689-930

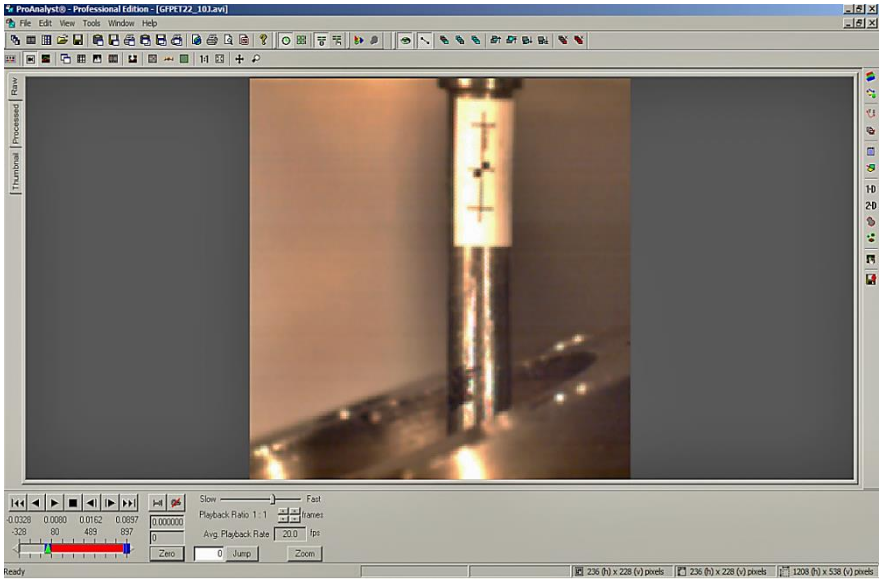

Figure 3.7 An example of a ProAnalyst software interface of a 20° impact on a thin laminate.

For oblique impact testing, a customized jig was designed and fabricated to study impact events at both 10° and 20° inclination angles, as shown in Figure 3.8, for a closer view. These low-velocity impact tests at inclined angles were carried out on fully-clamped plates using a 100 mm inner diameter ring support. Details of the

experimental set-up for the drop-weight impact tests on the laminated composites and the sandwich foam structures are given in Table 3.8.

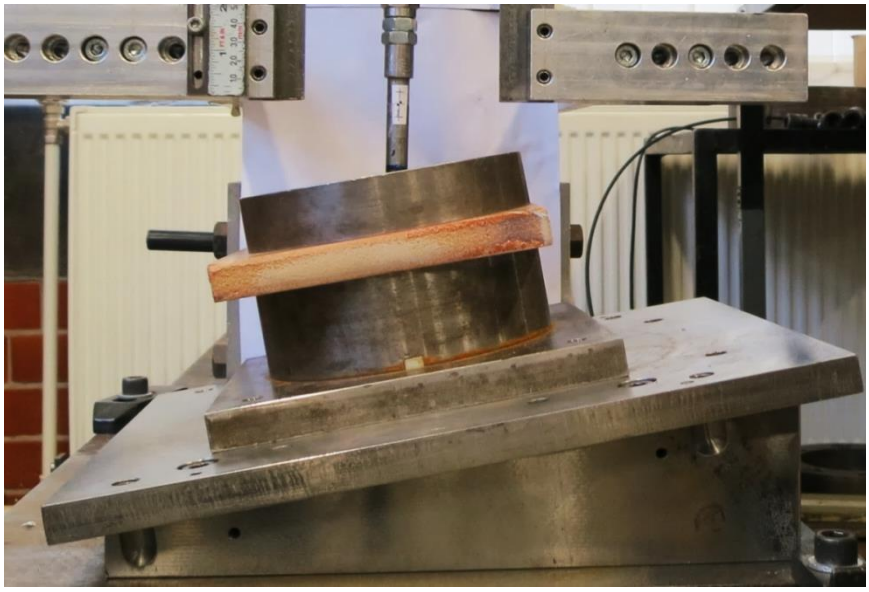

Figure 3.8 A closer view of the test-setup for a drop-weight impact test, with the use of a customized jig with 20° inclination angle.

Table 3.8 Impact test parameters for tests at normal (θ: 0°) and inclined angles on laminated composites and sandwich foam structures.

Type	**Inclination angle (°)**	**Release height (mm)**	**Impact energy (J)**	**Diameter of hemispherical indenter (mm)**
Laminated composites (GFRP)	0,10,20	36-550	2,5.6,8.5,14, 20, 25,28,31	12
R63.80 sandwich foam panels	0,10,20	45 – 357	2.5,5,10,15, 20	12
R63.140 sandwich foam panels	0,10,20	45- 357	2.5,5,10,15, 20	12
T92.100 sandwich foam panels	0,10,20	45-357	2.5,5,10,15, 20	12
T92.130 sandwich foam panels	0,10,20	45-357	2.5,5,10,15, 20	12

3.4.1 Indentation tests

A series of indentation tests were carried out using an Instron 4505 test machine at a crosshead displacement rate of 1 mm/minutes. Plain GFRP laminates, as well as sandwich structures with dimensions of 150 mm x 150 mm, were loaded up to a maximum force of 1 kN. The indentation tests were conducted by placing the fully-clamped test panels between circular steel ring supports, with an inner diameter of 100 mm. For tests at inclined angles, a customized jig was used, as shown in Figure 3.9. Using this test set-up, the bending/shear stiffness values of the materials tested were measured from the load (P) - deflection (δ) traces using Equation 3.1 below:

$$P = K_{bs}\delta + K_m\delta^3 \qquad 3.1$$

Where P is the applied load; K_{bs} is the bending/shear stiffness; δ is the deflection, and K_m is the membrane stiffness.

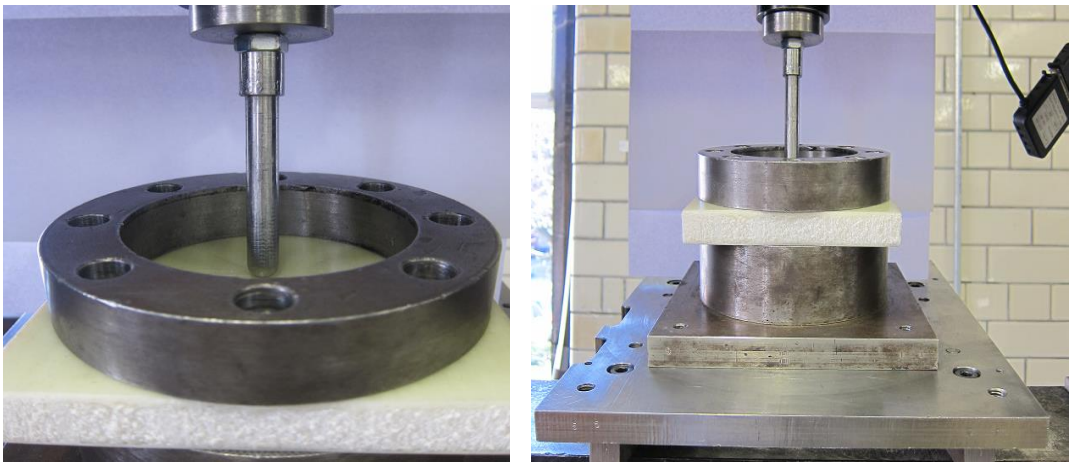

Figure 3.9 A static indentation test set-up using the oblique impact test rig, showing (a) front view of the sandwich panels loaded at 10° of inclination; (b) A closer view showing contact between the hemispherical indenter and the inner surface of the sandwich panel.

To determine the indentation response of the composite circular plate, a solid steel base was used to suppress the out-of-plane flexural effects of the circular plate. The test panels were loaded at a cross-head displacement rate of 1 mm / min up to a force similar to that recorded in the drop-weight impact tests. The resulting load-indentation plots were then forced to fit a generalized contact law, as shown in Equation 3.2 below:-

$$P = C\alpha^n \tag{3.2}$$

Where P and α are the force and the contact displacement respectively, whilst C and n are the contact parameters. It must be noted here that the contact parameters differ for each inclination angle. In contrast to earlier work where n =1.5, in this study, the value of n, was determined experimentally, from the slope of the plot between log P vs. log α, whereas the log of contact stiffness, C, was determined from the y-intercept of the plot using the following relationship in Equation 3.3.

$$\log P = \log C + n \log \alpha \tag{3.3}$$

3.5 Surface Analysis

3.5.1 Visual observation

After impact, the test panels were inspected to identify any form of delamination or damage on the impacted surface and the rear surface of the impacted panels (for the laminated composites). Measurements of the gross damage area, the diameter of the damage, termed the damage size, D, were also undertaken. Images of the test panels were taken using a digital camera, while the damage profile, in terms of the

maximum gross damage area, as well as the damage size, and were measured using a digital calliper, with a rated accuracy of 0.02 mm and a resolution of 0.01mm.

3.5.2 Measurement of the maximum permanent indentation

A Mitutoyo dial gauge was used to measure the maximum permanent indentation after impact. The gauge has an accuracy of 0.001 mm. Readings were made across the impacted surface of the test panels to determine the maximum permanent indentation.

3.5.3 Optical microscopy of the damaged panels

The impacted surfaces were sectioned and polished to a 1200 μm finish using SiC paper. The panels were then viewed at a microscopic level to investigate the failure mechanisms at varying inclination angles and selected impact energies.

For the thin laminates, a Zeiss stereomicroscope, equipped with a Lumenera Infinity-2 camera was used to capture the images of the impacted surfaces for the test panels, as shown in Figure 3.10. The stereomicroscope generates three-dimensional, laterally precise images for microscopy analysis, featuring large object fields and allows extended working distances; whilst the Infinity-2 camera has a resolution in the range of 1.4 to 32 megapixels for excellent real-time viewing and capturing images.

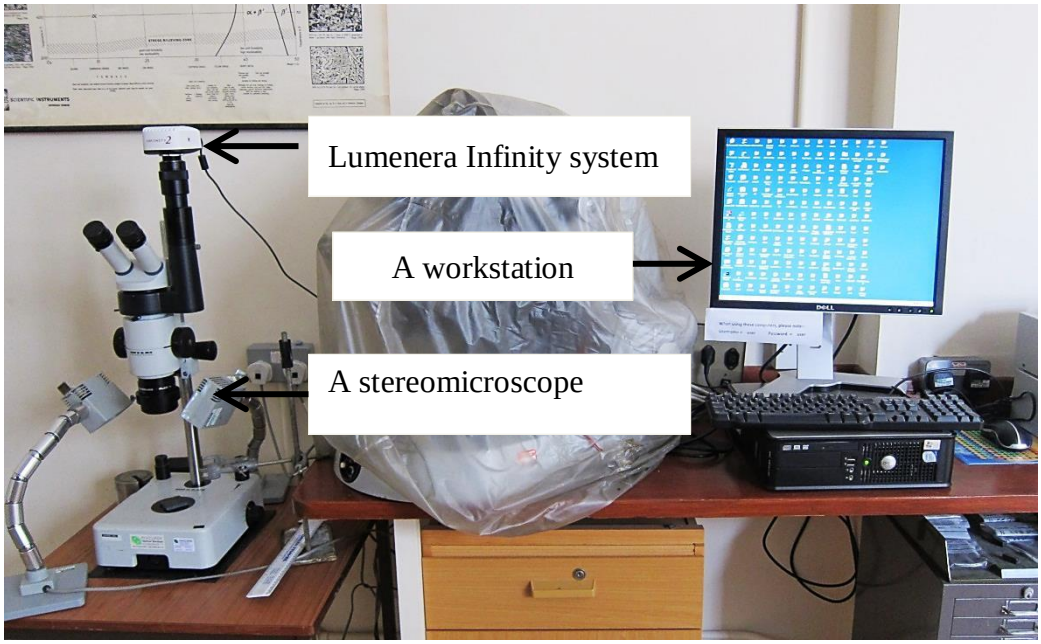

Figure 3.10 A stereomicroscope, connected to the Lumenera Infinity camera for real-time viewing and image capturing.

3.5.4 The energy-balance model

Based on the conservation of energy, predictions of the maximum contact force at varying inclination angles were made. Using the energy-balance model [4], the impact response of the laminated composites was modelled, where it is assumed that the kinetic energy of the target is absorbed in bending, shear and contact effect deformations, using Equation 3.4 as follows:

$$\frac{1}{2}mv^2 = E_{b/s} + E_m + E_c \qquad 3.4$$

Where m is the indenter mass, v is the velocity of the indenter, $E_{b/s}$ is the energy absorbed in bending and shear deformations, E_m is the energy absorbed in membrane deformations and E_c is the energy absorbed in contact deformations.

The energy associated with bending, shear and membrane deformations can be calculated by integrating the force-displacement relationship as shown in Equation 3.5 below:

$$E_{b/s} + E_m = \int_0^{\delta_{max}} P \, d\delta \tag{3.5}$$

Where, δ_{max} is the maximum displacement of the panel. In the case of a circular laminate, the relationship between the impact force, *P*, and the maximum displacement, δ_{max} is expressed as in Equation 3.6 below:

$$P = K_{b/s}\,\delta_{max} + K_m\delta^3 \tag{3.6}$$

Where $K_{b/s}$ is the effective bending/shear stiffness of the laminate and K_m is the membrane stiffness, to account for the membrane stretching. Therefore, rewriting Equation 3.5,

$$E_{b/s} + E_m = \frac{1}{2}K_{b/s}{\delta_{max}}^2 + \frac{1}{4}K_m{\delta_{max}}^4 \tag{3.7}$$

The energy absorbed in contact effects, E_c, can be modelled using a Hertzian contact law, as expressed in Equation 3.8 below:-

$$P = C\alpha^n \tag{3.8}$$

Whereby the *C* is the contact stiffness, α is the indentation and '*n*' is a contact parameter that is determined experimentally for each angle of inclination.

Therefore, the energy-balance Equation for a centrally-loaded circular plate can be expressed as:-

$$\frac{1}{2}mv^2 = \frac{1}{2}K_{b/s}{\delta_{max}}^2 + \frac{1}{4}K_m{\delta_{max}}^4 + \frac{C\left(\frac{P_{max}}{C}\right)^{\frac{n+1}{n}}}{n+1} \quad 3.9$$

Rewriting Equation 3.10,

$$mv^2 = K_{b/s}{\delta_{max}}^2 + \frac{1}{2}K_m{\delta_{max}}^4 + \frac{2C\left(\frac{P_{max}}{C}\right)^{\frac{n+1}{n}}}{n+1} \quad 3.10$$

Similarly, considering the impact response of circular plates, for a sandwich structures, the following expression applies for a centrally-loaded impact configurations [4]:

$$\frac{1}{2}mv^2 = \frac{{P_{max}}^2}{2}\left(\frac{1}{K_{b/s}}\right) + \frac{C\left(\frac{P_{max}}{C}\right)^{\frac{n+1}{n}}}{n+1} \quad 3.11$$

$$\therefore\ mv^2 = \frac{{P_{max}}^2}{K_{b/s}} + \frac{2\,C\left(\frac{P_{max}}{C}\right)^{\frac{n+1}{n}}}{n+1} \quad 3.12$$

For a sandwich plate, the load-deflection relationship is given by Equation 3.13 below:-

$$P = K_{b/s}\delta \quad 3.13$$

3.5.5 Prediction of the critical force to initiate damage in composite laminates

Recalling Equation 2.20 in Section 2.7.1 (Chapter II), P_{crit} is expressed as the following [5]:-

$$P_{crit}{}^{2} = \left(\frac{6ILSS^{3}\pi^{3}t^{3}}{E}\right)R \qquad 2.20$$

This Equation is applied to normal impact cases, whereby the inclination angle, $\theta = 0$.

In this study, the values obtained experimentally are compared with the theoretical values of $P_{crit,}$ using an equivalent expression for non-normal impact conditions (θ ≠0), with the following relationship as below:-

$$P_{crit_{(equivalent)}} = P_{crit}\ \cos(\theta) \qquad 3.14$$

$$\therefore P_{crit_{(equivalent)}} = \sqrt{\left(\left(\frac{6ILSS^{3}\pi^{3}t^{3}}{E}\right)R\ \right)}\cos(\theta) \qquad 3.15$$

Therefore, using the expression as in Equation 3.15, these theoretical values are compared with the experimental results and will be presented in Section 4.1.3.2 in Chapter IV.

3.6 Summary

In this chapter, description of the materials studied, including the raw materials used, relevant material properties, main equipment and processing route as well as an analytical model that were considered in this study has been presented, with selected examples of the typical plot and schematic diagram of the experimental set-up.

3.7 References

[1] SE84 Low Temperature Cure Resin Epoxy Prepreg System. Advanced Composites Group.

[2] http://www.corematerials.3acomposites.com/airex-r63-asia.html

[3] Composites A. AIREX® T92 - Easy Processing Structural Foam. 3A Composites; 2013.

[4] Hazizan, M. A., & Cantwell, W. J. (2003). The low velocity impact response of an aluminium honeycomb sandwich structure. Composites Part B: Engineering, 34(8), 679-687.

CHAPTER IV: RESULTS AND DISCUSSION

This chapter presents the results obtained from the experimental tests conducted in this research study, with selected results used to validate the theoretical models. More specifically, this chapter investigates the effect of varying inclination angles on the impact response of laminated composites and foam-based sandwich structures i.e. the maximum impact force, P_{max}, the damage area as well as the energy-absorption characteristics over a range of impact energies. In addition, at increasing energy, the perforation behaviour of sandwich structures (PET-based), subjected to normal and oblique inclination angles, under dynamic and quasi-static loading is presented to further investigate the impact response of these sandwich structures. Based on these findings, several conclusions are made to contribute to the understanding of the subject area.

4.0 Results and Discussion

To-date, there is still only limited experimental information on the oblique impact response of composites and sandwich structures, particularly in the low-velocity range [1-4]. Hence, it is the aim of this research study to conduct a series of experimental work including quasi-static tests, as well as drop weight impact on both structures.

4.1 Normal and Oblique Impact Response of GFRP Composite Laminate

In this section, the focus is to understand the impact response of laminated composites fabricated from an 8-ply unidirectional glass fibre reinforced epoxy laminate with a nominal thickness of 2 mm, at energies up to 28 J; from damage initiation (barely visible damage) up to perforation.

In addition, using an existing energy-balance model, the maximum impact force is predicted, using input data obtained experimentally, via static indentation tests with fully-clamped boundary conditions between two circular steel rings, using a hemispherical indenter of 12-mm diameter size.

In the next section, results obtained from a series of indentation tests on laminated composites are presented, showing the results in the form of load-indentation traces at inclination angles of 0°, 10° and 20° when subjected to a maximum load of 1 kN under quasi-static loading. Here, a solid steel support base is used to suppress the membrane effect.

From these experiments, the contact parameters are characterized; these include the contact stiffness, C, and the indentation exponent, n. Other important parameters obtained from the static test are the bending-shear stiffness, $K_{b/s}$, and the membrane stiffness, K_m, which was determined from the load-displacement plot, obtained from a static indentation test, whereby, for this test set-up, the test was conducted without a solid steel support. These parameters are used in the energy-balance model and the results will be discussed in Section 4.1.3.1.

In the last part, Section 4.1.3.2, the Sutherland and Soares model [5] used to predict the damage threshold load for damage initiation is presented and compared with the experimental values.

4.1.1 Theoretical predictions for impact response of the plain composites at normal and oblique angles using the energy-balance model

The contact response for laminated composites is known to be statically-determined using contact laws [6]. A general form of this equation was proposed by Meyer as $P = C\alpha^n$, in which the contact stiffness, *C*, and the indentation exponent, *n*, are considered as empirical constants, which must be determined experimentally from a quasi-static indentation test.

According to Hill *et al*. [7], the value of *n* reflects the material's behaviour as follows: (i) 1< *n* <1.5: for an ideally plastic material; (ii) *n* = 1.5: for a linearly elastic material. This is a typical assumption for a normal test condition (θ = 0°).

However, for this study, one of the approaches is to quantify the value of *n* from the static indentation test, hence $n \neq 1.5$. Details of these values for the three inclination angles are presented and discussed in the following section.

4.1.1.1 Determination of contact parameters

Figure 4.1 presents typical load-indentation traces following an indentation test on an 8-ply glass-fibre reinforced epoxy laminate, fully-clamped and centrally loaded up to 1 kN, for the three inclination angles; these being normal (0°), 10° and 20°. The load-indentation curve exhibits a typical force response associated with indentation on a laminated composite.

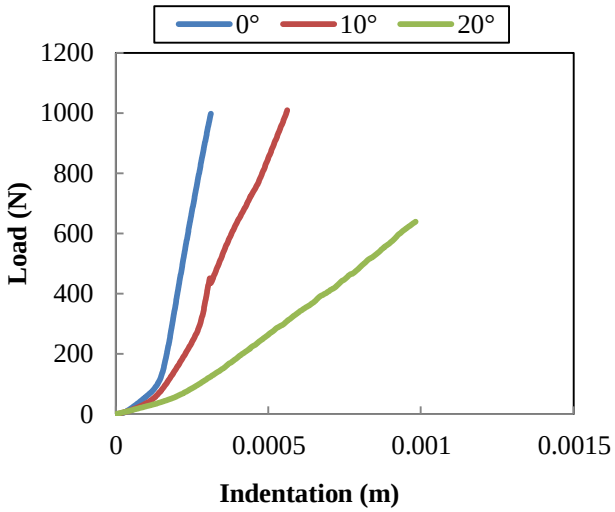

Figure 4.1 Typical load-indentation traces following an indentation test on an 8-ply glass fibre reinforced epoxy (GFRP) laminate, at a crosshead displacement rate of 1 mm/min using a 12-mm diameter hemispherical indenter.

For the normal angle case, the slope of the graph steadily increases up to 1000 N, with the maximum indentation reaching approximately 0.31 mm. The 10° inclination angle showed a slight load drop at 400 N, occurring at a higher indentation value and the load continued to increase until the maximum load was applied and the test automatically stopped.

With increasing inclination angle, i.e. at 20°, the structure exhibited a lower maximum load, corresponding to a larger indentation, suggesting a reduced stiffness at this angle.

In order to quantify the contact parameters, from the indentation law, $P = C\alpha^n$, a graph of log P versus log α yields the value of log C (from the intersection of the y-axis), while the value of the indentation exponent, n, is obtained from the slope of the traces. Based on this approach, the contact stiffness, C, and the indentation exponent, n, was determined for the three inclination angles, as presented in Figure 4.2.

From Figure 4.2 (a), the contact stiffness reduces in passing from 0° to 20°. This is expected, since at angles other than 0° there is a reduction in the slope of the graphs in passing from 0° to 20°. Hence, due to the effect of geometry, the corresponding contact stiffness decreases with an increase in inclination angle.

The indentation exponent, *n*, of the laminated composites, as presented in Figure 4.2 (b) also show similar trends to the contact stiffness with increasing inclination angle, where the average value of *n* is 1.18 ± 0.05 for 0°, 1.15 ± 0.05 for 10° and 1.08 ± 0.02 for the 20° inclination angle. However, these values do not show a significant difference between the three inclination angles. In addition, these values may reflect the type of material behaviour each exhibits. For example, Hill *et al*. [7], suggest that when *n* is between 1 and 1.5 (1<n<1.5), the material is said to be plastic.

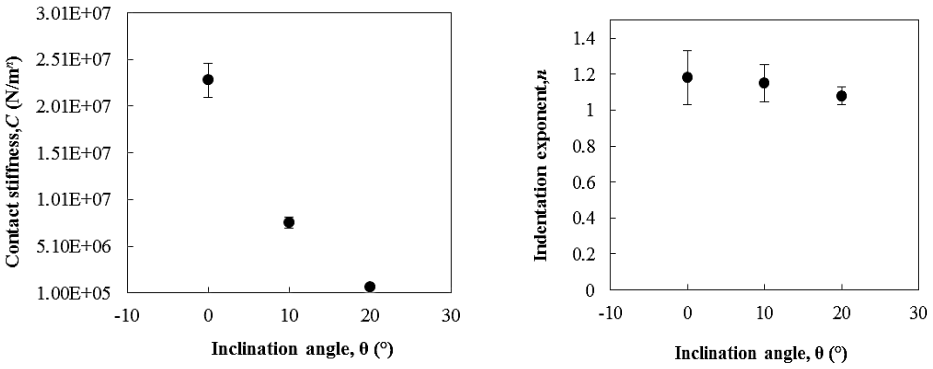

(a) (b)

Figure 4.2 (a) Contact stiffness, *C*, for an 8-ply GFRP laminate tested under static indentation loading at varying inclination angles, (b) Contact parameter '*n*' for an 8-ply GFRP laminate tested under static indentation loading at varying inclination angles.

4.1.2 Experimental results following normal and oblique impact on the GFRP laminate

To - date, there is still limited experimental information reported on the oblique impact response of composites and sandwich structures, particularly in the low-velocity range. Therefore, in this study, initially, one of the important parameters to consider is the impact force, which is measured directly using a force transducer. This parameter is termed the striking force, F_s, in the work by Madjidi *et al*. [1], which is similar to the impact force measured directly in this study.

The experimental results following normal and oblique impact tests on the laminated composites are presented in this section, as given in Table 4.1. As shown, the main findings of this study include the maximum impact force, the corresponding (calculated) maximum normal force, the damage area and the absorbed energy following impact at inclination angles of 0°, 10° and 20°.

Examples of typical load-time traces for the laminated composites following normal and oblique impact subjected to different energy levels, i.e. 5.6 J, 14 J, 20 J and 28 J, are presented in Figure 4.34 to Figure 4.6. At low energy levels, i.e. at 5.6 J, the curves are smooth, suggesting an elastic behaviour, as evident in the load-time traces. At this stage, the effect of obliquity is not apparent, particularly between 0° and 10° impact angles, as presented in Figure 4.3. From visual observations, it is seen that all of the test panels exhibit barely visible damage.

Table 4.1 Experimental results following a series of normal and oblique impact tests on the 8-ply GFRP laminates at normal and oblique angles.

Inclination angle (°)	**Impact energy (J)**	**P_{max} (N)**	**F_N (N)***	**Damage area (mm^2)**	**Absorbed energy (J)**	**Max depth of permanent indentation (mm)**
0	5.6	1976 ± 94	1976	40 ± 1	0.9 ± 0.1	0.14 ± 0.01
	8.5	2982 ± 239	2982	84 ± 5	2 ± 0.2	0.18 ± 0.01
	14	4379 ± 347	4379	184 ± 11	4.2 ± 0.4	0.26 ± 0.00
	20	5129 ± 390	5129	284 ± 29	7.5 ± 1.0	0.5 ± 0.00
	25	5202 ± 549	5202	828 ± 67	16± 2.5	1.64 ± 0.01
	28	5521± 552	5521	816 ± 65	17.5 ± 2.4	1.69 ± 0.01
10	5.6	2079 ± 99	2005	60 ± 2	1.7 ± 0.1	0.08 ± 0.01
	8.5	3109 ± 250	2998	120 ± 8	2.0 ± 0.2	0.11 ± 0.01
	14.1	3579 ± 284	3451	204 ± 15	5.7 ± 0.5	0.14 ± 0.00
	20	4667 ± 354	4501	408 ± 41	9.5 ± 1.3	0.86 ± 0.08
	25	4777 ± 504	4607	800 ± 100	16.3 ± 2.7	1.81 ± 0.16
	28	5000 ± 500	4822	776 ± 90	20.9 ± 3.5	1.43 ± 0.13
20	5.6	1487 ± 27	1427	72 ± 2	2.1 ± 0.2	0.04 ± 0.00
	8.5	2208 ± 52	2118	136 ± 9	7.5 ± 0.7	0.04 ± 0.00
	14	2620 ± 111	2514	206 ± 10	11.8 ± 0.3	0.06 ± 0.00
	20	2758 ± 251	2646	226 ± 30	14.1 ± 1.9	0.07 ± 0.00
	25	3348 ± 307	3212	296 ± 30	22.5 ± 3.9	0.08 ± 0.00
	28	3560 ± 326	3416	314 ± 25	24.6 ± 2.08	0.09 ± 0.00

(*Note: F_N is calculated from theory)

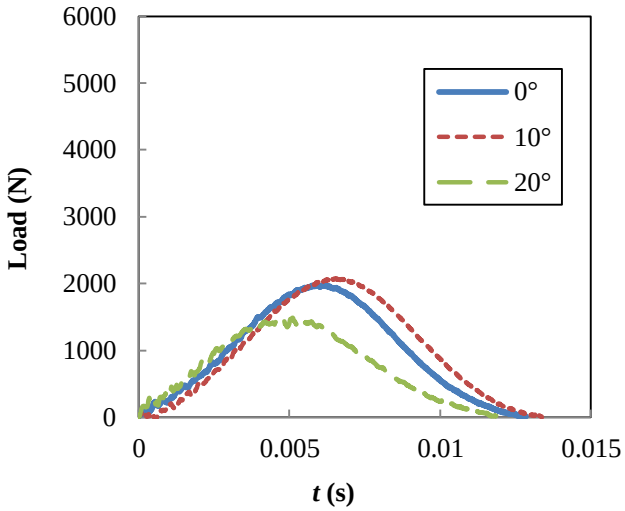

Figure 4.3 Typical load-time traces for an 8-ply GFRP laminate subjected to 5.6 J under normal and oblique impact.

For medium energies, i.e. 14 J, the load-time responses exhibit an almost smooth curve, suggesting a linear elastic response, for the three cases, as evident in Figure 4.4. Here, the force is almost two times greater than that for the response when subjected to 5.6 J (Figure 4.34). Interestingly, the normal impact response shows a peak force at much earlier contact time, less than 4 ms, whilst the non-normal impact reaches its peak force later, close to 6 ms, with much lower magnitudes than the normal impact case.

With increasing energy, i.e. at 20 J, it is apparent that impact at 0° and 10° exhibits a slight load drop, whereas the response remains elastic at the higher inclination angles, i.e. the 20° inclination angle, with the lowest maximum impact force, as shown in Figure 4.5. At this point, the effect of obliquity is more apparent, as observed in the difference in the force magnitude between the three inclination angles, with the 0° case exhibiting the highest maximum peak force in comparison to that of the non-normal impact cases.

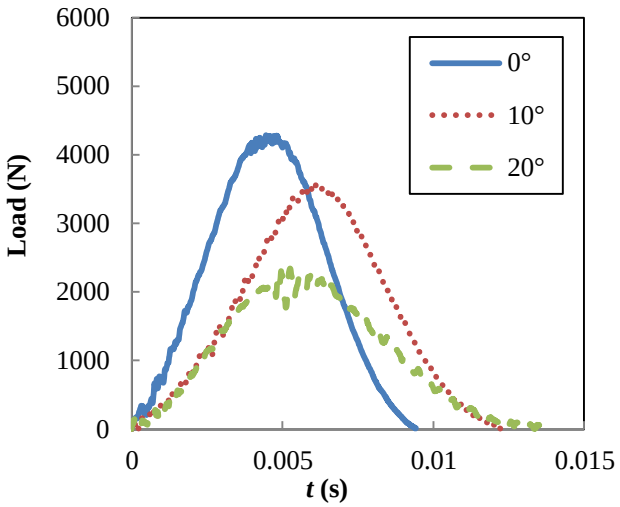

Figure 4.4 Typical load-time traces for an 8-ply GFRP laminate subjected to 14 J under normal and oblique impact.

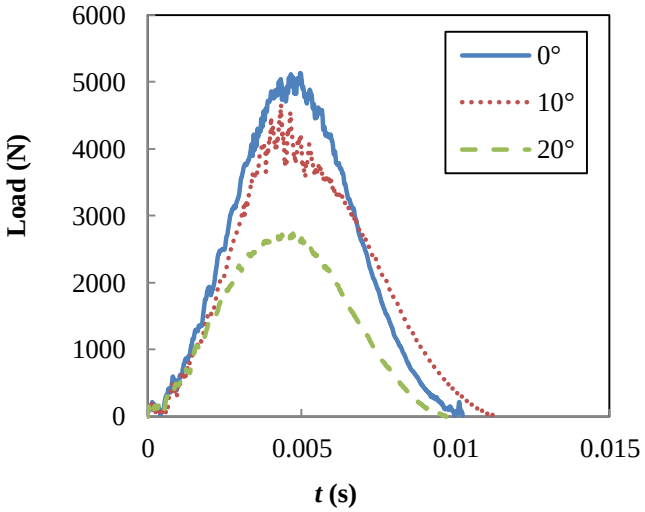

Figure 4.5 Typical load-time traces for an 8-ply GFRP laminate subjected to 20 J under normal and oblique impact.

With increasing energy, i.e. up to 28 J, both the 0° and 10° impact responses exhibit a sudden load drop, suggesting the presence of extensive fibre fracture or cracking in the composite (Figure 4.6). At this energy level, the 20° impact response started to show a slight load drop in the load-time traces, relative to the other impact cases.

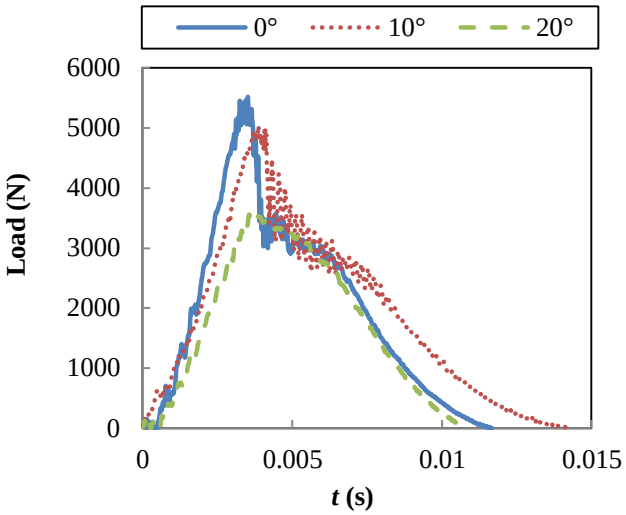

Figure 4.6 Typical load-time traces for an 8-ply GFRP laminate subjected to 28 J under normal and oblique impact.

Typical load-displacement traces and the corresponding energy-time traces following normal impact on the 8-ply GFRP laminate at selected impact energies are presented in Figure 4.7, Figure 4.8 and Figure 4.9.

At relatively low energies, i.e. at 5.6 J, in Figure 4.7, the force-displacement traces are clearly non-linear. This is due to membrane effects, since the maximum displacement is approximately 2.5 times the plate thickness. From this plot, a small residual displacement of approximately 0.2 mm is observed.

With increasing impact energy (i.e. at 14 J), the load-displacement traces becomes increasingly non-linear, again due to membrane effects. The maximum impact force at this energy level is nearly twice that following a 5.6 J impact. In addition, the residual displacement also increased with the value of 1.5 mm; the maximum displacement at this energy level is approximately 1.75 times greater than that at 5.6 J.

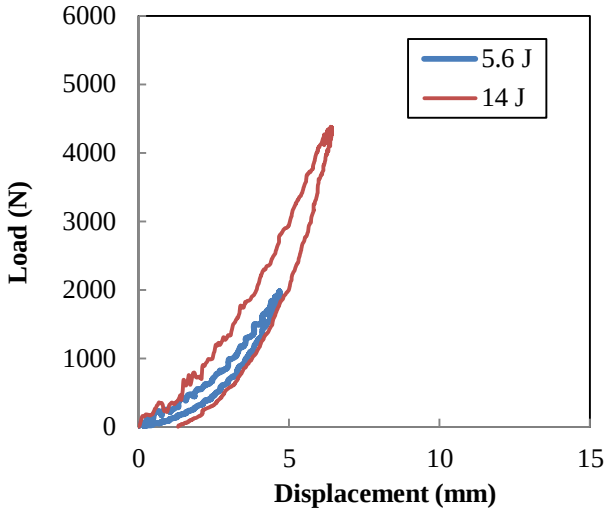

Figure 4.7 Typical load-displacement traces for an 8-ply GFRP laminate following normal impact at energies of 5.6 J and 14 J.

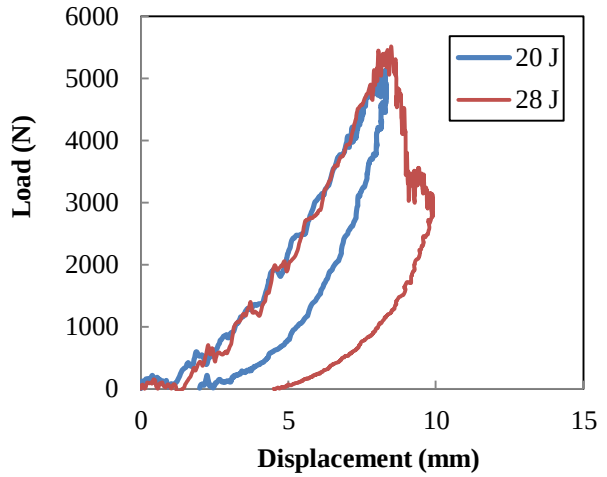

Figure 4.8 Typical load-displacement traces for an 8-ply GFRP laminate following normal impact at energies of 20 J and 28 J.

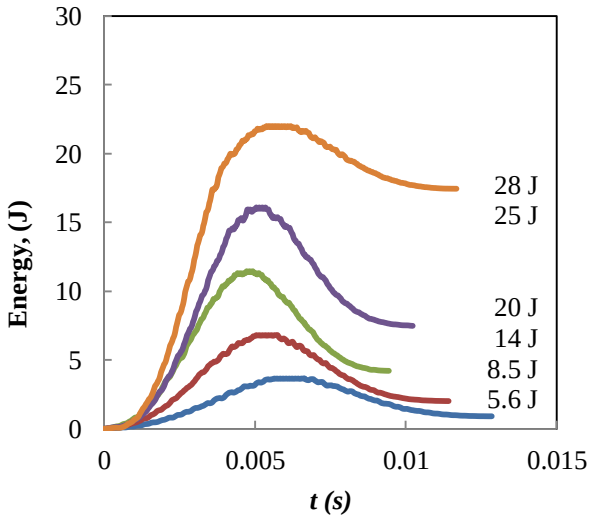

Figure 4.9 Typical energy-time traces for an 8-ply GFRP laminate following normal impact loading.

Following a 20 J impact, the load-displacement traces exhibits a small drop in load, as presented in Figure 4.8. This corresponds to the threshold where fibre fracture occurs in the composite system. At 28 J, it is clear that the maximum impact force does not increase further with impact energy, suggesting that this limit is determined by the maximum strength of the laminate; the maximum contact force is close to the response observed at 20 J. A sudden load drop occurred, indicating the development of extensive fibre fracture / cracking in the composite, resulting in a greater residual displacement following normal impact at energies of 20 J and 28 J.

According to the literature, "*depending on the impact energy level, three interaction modes could exist between the composite panel and the indenter following normal impact; these being (i) when the energy absorbed by the composite is very little, the indenter bounces back; (ii) when most of the energy is being absorbed by the composite through various modes of damage, thus no rebound occurs; and (iii) in the case of high energy level, perforation can be observed"* [8].

Based on this understanding, a schematic diagram is presented in Figure 4.10, to illustrate the three forms of energy: the impact energy, the resultant rebound energy and the absorbed energy [8]. The energy-time plot can be produced from an integration of the load-displacement data as a function of time.

According to Madjidi [1], increasing the inclination angle will results in significant force reaction in the horizontal direction, with the force components as illustrated in Figure 2.16, thereby, producing a horizontal deflection in the guide assembly which results in an increase in the residual displacement. Consequently, this result in an increase in the absorbed energy and a decrease in the rebound energy.

For this study, it has been observed that these forms of energies are essentially important in determining the energy absorption of the composite structures following normal and oblique impact since at low energy level, in the elastic regime, the rebound energy is more significant than that of the response at relatively higher energy levels.

These forms of energy are evident in the energy-time traces following normal impact on the GFRP laminate, as given in Figure 4.9, whereby at relatively low energy level, i.e. ≤ 20 J, only a small amount of energy is absorbed by the target. This is associated with rebounding of the indenter following a linear elastic response.

At higher impact energies, i.e. 28 J, where plastic deformation is in the form of indentation or perforation, most of the energy is absorbed by the target; hence, resulting in a marginal amount of energy in the form of a rebound, as demonstrated in the energy-time traces in Figure 4.9 and the calculated absorbed energy as given in Figure 4.17.

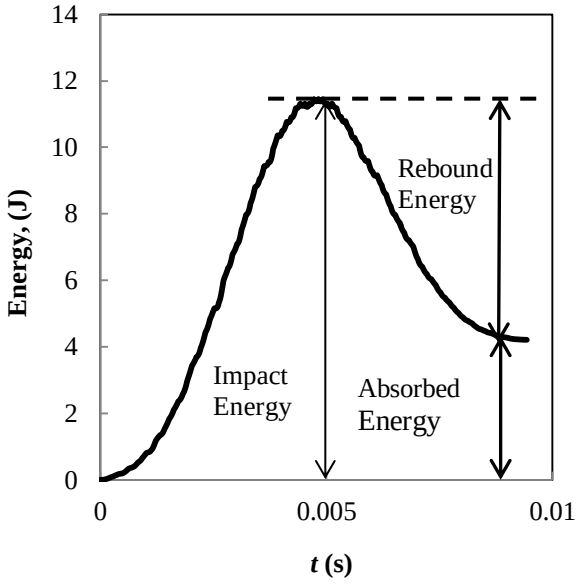

Figure 4.10 A schematic diagram showing a typical energy vs. time curve when rebound occurs [8].

Typical load-displacement traces and the corresponding energy-time traces following 10° impact on the 8-ply GFRP laminate at selected impact energies are presented in Figure 4.11, Figure 4.12 and Figure 4.13.

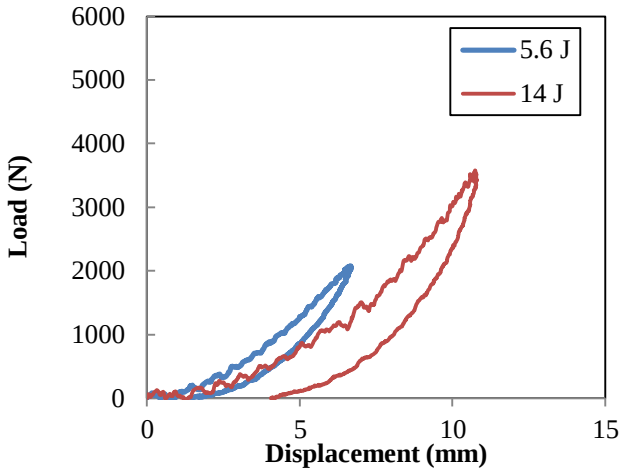

Figure 4.11 Typical load-displacement traces for an 8-ply GFRP laminate subjected to a 10° impact at energies of 5.6 J and 14 J.

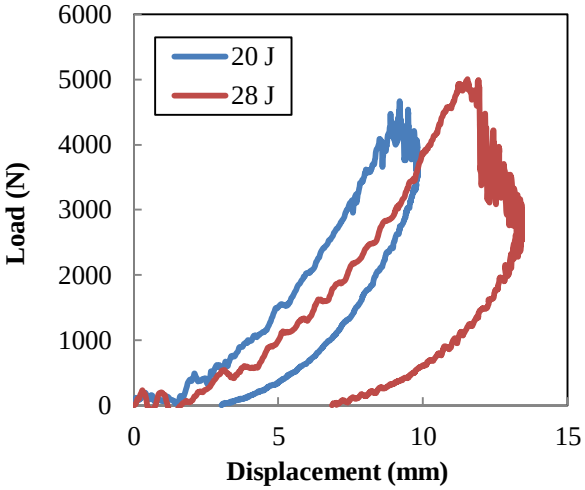

Figure 4.12 Typical load-displacement traces for an 8-ply GFRP laminate subjected to a 10° impact at energies of 20 J and 28 J.

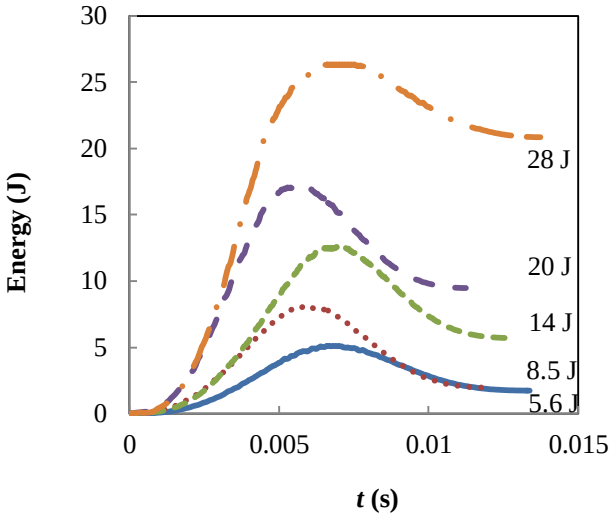

Figure 4.13 Typical energy-time traces for an 8-ply GFRP laminate following 10° impact loading.

At relatively low energies, i.e. at 5.6 J, in Figure 4.11, the load-displacement trace is clearly non-linear due to membrane effects. There is a small residual displacement of approximately 1.5 mm. With increasing impact energy (i.e. at 14 J), the load-displacement traces becomes increasingly non-linear, again due to membrane effects. The maximum impact force at this energy level is nearly twice that following a 5.6 J impact. In addition, the residual displacement also increased with the value of approximately 3.2 mm.

Following a 20 J impact, the load-displacement traces exhibits a small drop in load, as presented in Figure 4.12. This corresponds to the threshold where fibre fracture occurs in the composite system.

At relatively high energy, i.e. 28 J, it is clear that the maximum contact force does not increase further with impact energy, suggesting that this limit is determined by the maximum strength of the laminate; the maximum contact force is close to the response observed at 20 J. A sudden load drop occurred, indicating the development of extensive fibre fracture / cracking in the composite, resulting in a greater residual

displacement. At this point, a larger area under the load-displacement trace suggests an increase in the energy absorbed, which is evident from the plot of energy absorbed vs. impact energy, as shown in Figure 4.17 (page 115).

These observations are evident in the energy-time traces following a 10° impact on the GFRP laminate, as given in Figure 4.13, whereby at relatively low energy level, i.e. $\leq$ 20 J, only a small amount of energy is absorbed by the target. This is associated with rebounding of the indenter following a linear elastic response.

At higher impact energies, i.e. 28 J, where plastic deformation is in the form of perforation, most of the energy is absorbed by the target; hence, resulting in marginal amount of energy in the form of a rebound, as demonstrated in the energy-time traces in Figure 4.13 and the corresponding absorbed energy as given in Figure 4.17 (page 115).

The load-displacement traces and the corresponding energy-time traces following 20° impact at low and high impact energies are given in Figure 4.14, Figure 4.15 and Figure 4.16. At low energy, i.e. $\leq$ 14 J, the load-displacement traces show that there was a not large load drops for both the loading (up to peak force) and unloading curves. The residual displacements for the response subjected to a 5.6 J and 14 J are 3.8 mm and 9.7 mm, respectively.

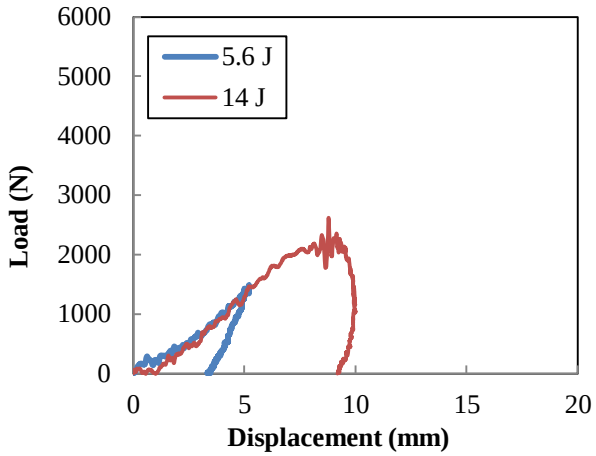

Figure 4.14 Typical load-displacement traces for an 8-ply GFRP laminate subjected to a 20° impact at 5.6 J and 14 J.

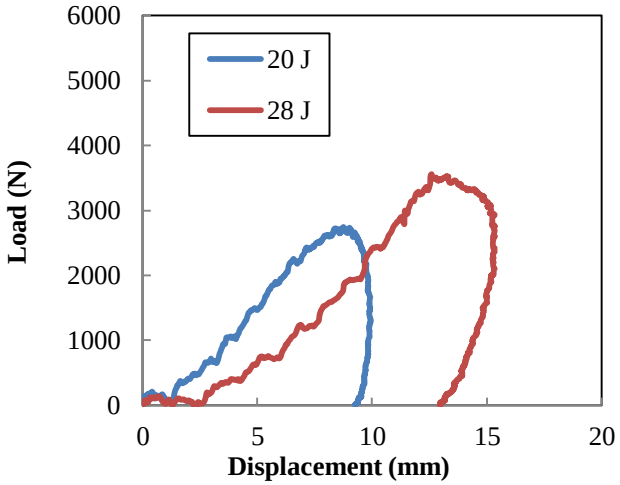

Figure 4.15 Typical load-displacement traces for an 8-ply GFRP laminate subjected to a 20° impact at energies of 20 J and 28 J.

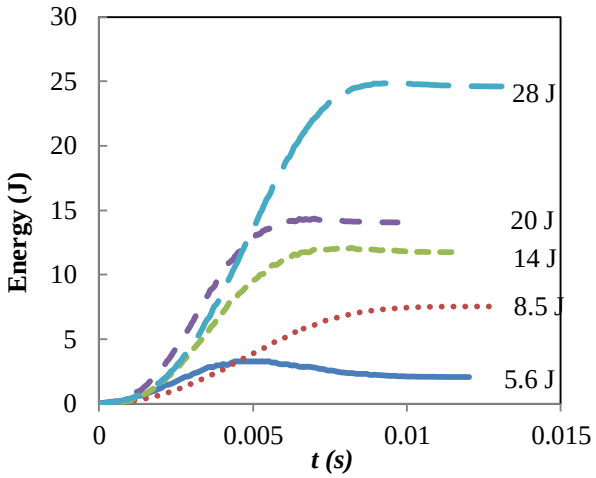

Figure 4.16 Typical energy-time traces for an 8-ply GFRP laminate following 20° impact loading.

At increasing impact energy, with the increase in the maximum impact force and the maximum displacement for both 20 J and 28 J impact cases, the area under the load-displacement also increases, suggesting an increase in the energy absorbed.

This is confirmed by the energy-time plots (Figure 4.16) following a 20° impact on the GRRP laminate and the corresponding plot of the absorbed energy vs. impact energy in Figure 4.17. Clearly, regardless of the level of impact energy, there is only a marginal amount of energy in the form of rebound energy. This shows that the majority of the impact energy is absorbed by the target, which may be attributed to the effect of geometry, which causes more kinetic energy to be transferred to the indenter during impact at a higher inclination angle [4].

Overall, it has been observed that the effect of obliquity on the indenter residual displacement is apparent on the indenter residual displacement, as a result of a force reaction in the horizontal direction. As an example, following a 14 J impact, this produces a residual displacement of 1.5 mm for the 0° impact, 4.6 mm for the 10° impact and 9.7 mm following a 20° impact case.

The absorbed energy plotted against impact energy is given in Figure 4.17 for impact at the three inclination angles. Clearly, the results suggest that the oblique impact case exhibits the highest energy absorption, whereas normal impact showed the lowest energy absorption capability. Similar observations have been reported by Hazell *et al*. [4], where it was argued that the reason is because more of the kinetic energy was transferred from the indenter to the target material in comparison to normal impact loading. They argued that this was merely due to a geometrical effect.

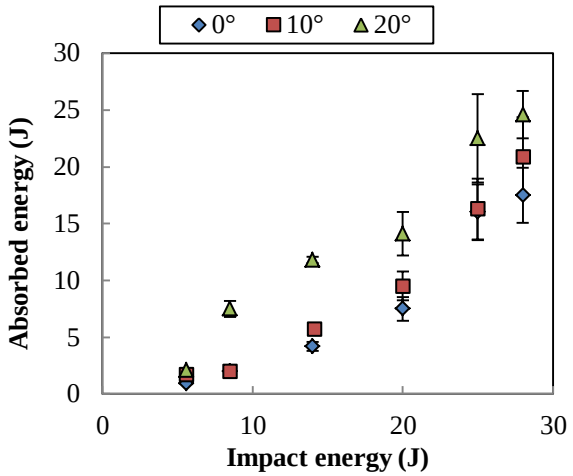

Figure 4.17 Absorbed energy against impact energy for an 8-ply GFRP laminate subjected to normal and oblique impact.

The maximum impact force (load), P_{max}, which is an average from a series of experimental tests, is given in Figure 4.18. From the data, it is apparent that in general, P_{max} increased with impact energy, up to 20 J, suggesting a threshold limit. Also, it is clear that the normal impact (0°) yielded the highest maximum impact force. One of the reasons for this is the higher contact stiffness at 0°, as evident in Figure 4.2(a).

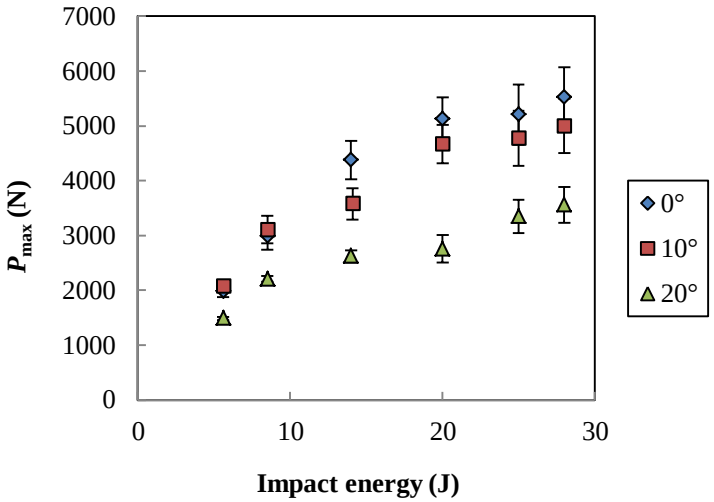

Figure 4.18 Maximum impact force against impact energy for an 8-ply GFRP laminate subjected to normal and oblique impact.

Beyond this, there is a plateau for both the 0° and 10° impact cases, whereas the 20° impact showed a continuous increase up to this point. These observations are expected, based on earlier work by Madjidi *et al*. [1], where it was reported that it was the normal impact condition (0°) that yields the highest maximum impact force (load) as compared to the oblique impact cases.

In addition, the corresponding normal force, F_N, which is acting on the impact surface, was calculated using Equation 2.39 in Chapter II. It should be noted that this value is crucial, since it is the normal force component that causes damage to the structure during a normal or oblique impact event [1]. The calculated values of this force component are presented in Figure 4.19, showing a similar trend as in those of the maximum impact force. Here, the non-normal impact, as expected, exhibits much lower forces in the normal direction.

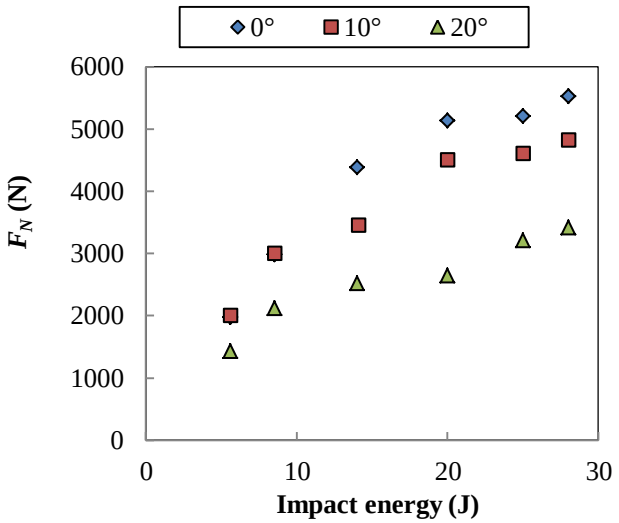

Figure 4.19 Calculated maximum normal force, F_N, for an 8-ply GFRP laminate against impact energy during normal and oblique impact.

The measured gross damage area of the composites is presented in Figure 4.20. Here, it is apparent that both the 0° and 10° impact cases exhibit a greater level of damage,

relative to the 20° impact case. This is expected, since the contact stiffness and the normal force at the 20° inclination is lower, therefore the resulting damage is less. Furthermore, similar observations were reported in earlier work on oblique impact, as mentioned in Section 2.7, where it was highlighted that the normal impact caused the more severe form of damage in comparison with the oblique impact [1- 3].

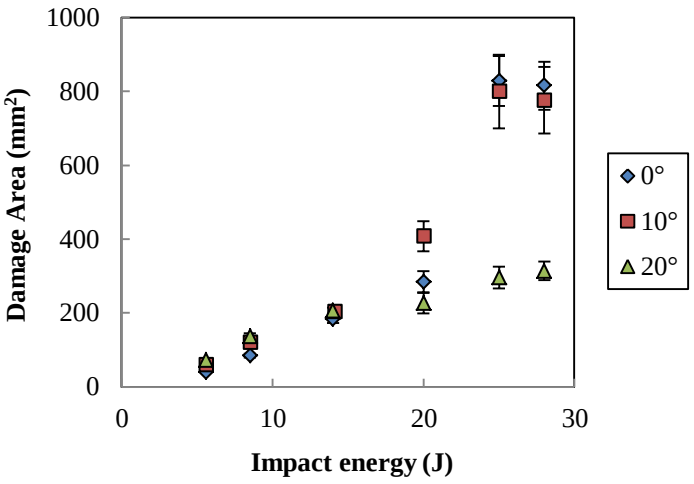

Figure 4.20 Damage area against impact energy for an 8-ply GFRP laminate subjected to normal and oblique impact.

Figure 4.21 shows a plot of the maximum depth of permanent indentation as a function of impact energy for an 8-GFRP laminate subjected to normal and oblique impact. It appears that, for the normal impact, maximum depth of permanent indentation increases gradually with impact energy up to 25 Joules. Beyond this, the value plateaued at approximately 28 J, with a maximum depth of permanent indentation of 1.69 mm.

For the 10° impact case, at energies up to 25 J, the maximum depth of the permanent indentation is approximately 1.81 mm. However, above this level, the value dropped to approximately 1.43 mm. Following a 20° impact, since there is barely any visible

damage in the composite structure, this results in a marginal increase in the maximum depth of permanent indentation. The maximum depth of permanent indentation is approximately 0.09 mm at 28 J.

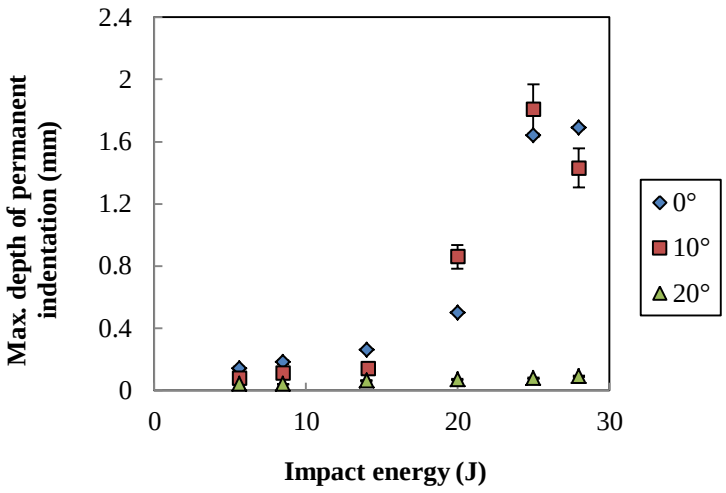

Figure 4.21 Maximum depth of permanent indentation vs. impact energy following normal and oblique impact on an 8-ply GFRP laminate.

In addition, visual observations on selected test panels, showing the impact surface of each of the impact cases, are presented in Figure 4.22 (a) 0° impact with total damage area measured as 816 mm^2 , (b) 10° impact with total damage area of 716 mm^2 and in (c) for 20° impact with total damage area of 314 mm^2. These images clearly show the damage pattern for the three impact conditions, whereby the normal impact resulted in the typical peanut-like shape. The damage size, *D*, which corresponds to delamination, for the panel subjected to normal impact is approximately 83.5 mm. The 10° impact exhibits an almost similar damage pattern to the normal impact, with slightly longer dimension of the damage size, of approximately 89 mm, suggesting additional prominent force in the form of shear loading presence when impacted at 10°.

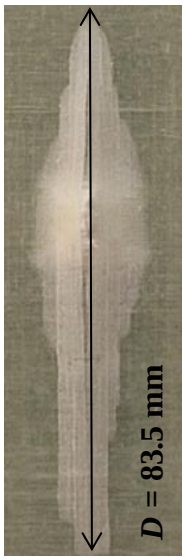

(a) 'Peanut' shaped damage on the rear surface of an 8-ply GFRP laminates following a 28 J normal impact, suggesting a combined effect of tension and compression loading. (D = 83.5 mm)

(b) 'Peanut' shaped damage on the rear surface of an 8-ply GFRP laminate following a 28 J 10° impact, suggesting an effect of tension and compression loading as well as shear effect, with the damage size being slightly greater than that of the normal impact case. (D = 89 mm)

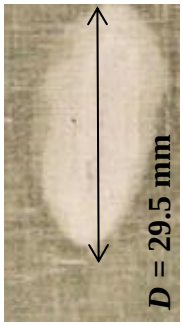

(c) Elliptical delamination on the rear surface of an 8-ply GFRP laminate following a 28 J impact at 20° of inclination, suggesting the effect of pure shearing with an elliptical contact surface during a 20° impact.
(D = 29.5 mm)

Figure 4.22 Photographs of the back surfaces of 8-ply GFRP laminate subjected to impact at 28 J at (a) a normal angle; (b) 10° and 20°.

Lastly, as for the 20° impact, it is apparent that visible damage took the form of an elliptical shape, which is possibly mainly attributed to shearing effect, as well as due to the elliptical contact surface that is formed during an oblique impact.

To further investigate these responses, cross-sections of selected panels following impact at 28 J are shown in Figure 4.23. Clearly, the composites that are subjected to normal impact, exhibit permanent indentation, with penetration of the indenter into the impact surface, consisting of matrix cracking and fibre fracture, due to compression at the impact surface as well as tensile cracking on the rear surface, as evident in Figure 4.23(a). The measured depth of permanent indentation is approximately 1.69 mm.

For the 10° impact case, as shown in Figure 4.23(b), it is evident that the composite structures exhibit a similar form of damage, as in the case for normal impact. In compression and tension, the crack grows through the thickness of the specimen; while in shearing, the crack propagates along the surface of the specimen [9]. Thus the combination of these affects lead to the damage pattern, as evident in Figure 4.23(b) (rear surface) and the corresponding cross-section in Figure 4.23(b). The measured depth of permanent indentation for this case is approximately 1.43 mm.

At increasing inclination angle, following a 20° impact, referring to Figure 4.23 (c), only barely visible impact damage (BVID) is evident at the cross-section, in the form of delamination. For this case, the measured depth of permanent indentation is minimal, which is approximately 0.09 mm. This is expected, since at this inclination angle, both the maximum impact force and the corresponding maximum normal force are the lowest of the three angles.

(a) Normal impact

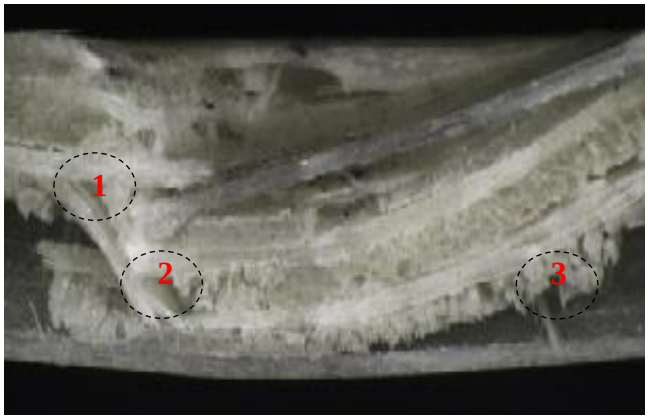

(b) 10° impact

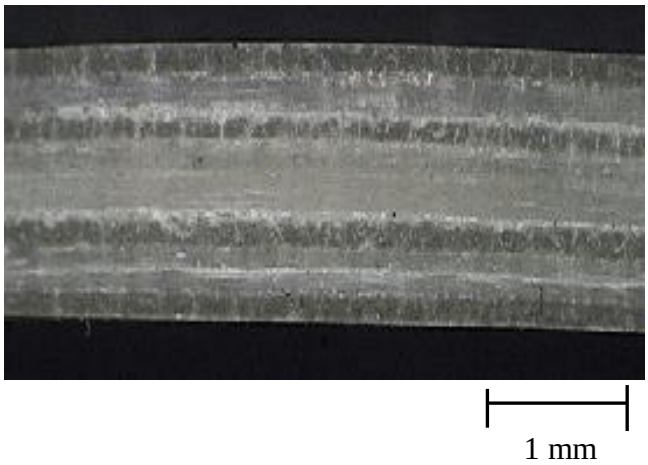

(c) 20° impact

Figure 4.23 Optical micrographs showing cross-sections of an 8-ply GFRP laminate subjected to impact loading at 28 J with inclination angles of (a) 0°; (b) 10° and (c) 20°. (Note: '1 & 2' ≡ failure at the interface and '3' ≡ ductile fibre fracture).

Here, there was no apparent evidence of fibre fracture, suggesting that the crack propagates along the interface between the matrix and the fibre. These observations are typical for shear-dominated failure. Therefore, it is possible that the main cause of damage is dominated by a shearing effect, rather than compression, leading to final fracture in the form of delamination of the lamina due to weak interfacial bonding between the fibre and the matrix. In addition, these findings also suggest the presence of shearing of the epoxy matrix chain-network.

In summary, for the case of laminated composites, it is evident that the normal impact, which has the highest maximum normal force, F_N, which caused more severe damage at energies up to 28 J. In addition, the 10° impact, exhibits an intermediate behaviour of the 0° and 20°, possibly due to the combination tensile, compression and shear, for impact loading at this inclination angle. At increasing inclination angle, i.e. 20°, the impact response is mainly governed by shear. In addition, since the normal force component, F_N, is greatly reduced with an increase in inclination angle, due to the effect of geometry, the resultant damage is minimal.

4.1.3 Comparison of experimental and theoretical results

4.1.3.1 Predictions of maximum contact force using an energy-balance model

An energy-balance model was employed in order to predict the maximum contact force at normal and oblique impact angles. Recalling Equation 3.10 in Chapter III, the maximum deflection, $\delta_{\max}$ was determined using the Microsoft Excel software package, where the value of $\delta_{\max}$ was systematically increased until the right hand side of Equation 3.10 equalled the left hand side (i.e. the input energy). Once the maximum displacement had been determined, the maximum contact force, P_{max} was calculated using Equation 3.9.

An example of how effective the energy-balance model is in predicting the impact response is presented in Figure 4.24, for normal and oblique impact cases on a fully-clamped GFRP laminate. From the plot, it is evident that the energy-balance model is in good agreement with the experimental data in the elastic regime (i.e. up to 14 J). This is particularly true for the 0° impact case, with a maximum difference of approximately 20% between the experimental results and the predicted values for impacts up to 14 J. However, the 10° impact shows a greater difference between the two values, increasing from 13% up to 40% with increasing impact energy. This is possibly due to the more complex response during impact at this inclination angle, where the damage profile in the composite structure shows evidence of the effect of tensile, compression and shear loading. For the case of a 20° impact, there is about a 20% difference between the experimental and the predicted maximum impact forces at energies up to 14 J.

Above this energy level, where severe damage occurs in the structure, the energy-balance model tends to over-predict the maximum contact force. Here, the maximum difference between the predicted and the experimental values is up to 60%, especially for the non-normal impact (i.e. 10° impact case). Above the damage threshold, the model tends to over-estimate the maximum contact force, due to the fact that it does not consider the initiation and propagation of damage in the structure, which is one of the limitations of this model that is reported by other researchers [10].

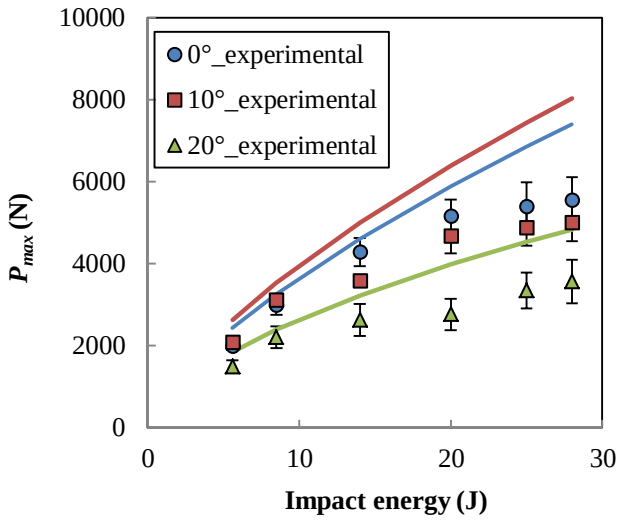

Figure 4.24 Experimental and predicted maximum contact force (lines) for an 8-ply GFRP laminate subjected to normal and oblique impact.

4.1.3.2 Damage initiation in an 8-ply GFRP laminate

Visual observations of the GFRP laminate following normal and oblique impact at relatively low impact energies up to 5 J have shown that damage initiation differs between normal, 10° and 20° impact angles, which occurred at approximately 2 J at 0°, 2.9 J at 10° and 4.7 J for a 20° impact. The corresponding forces at these threshold energies are tabulated in Table 4.2. This parameter is termed P_{crit}, which is the critical force at which delamination occurs [5]. Predictions of this parameter have been made using Equation 3.15 in Chapter III in Section 3.8, and compared with the experimental values, as given in Figure 4.25. The value of the interlaminar shear strength (ILSS) is taken as 147 MPa, from experimental data presented in [3].

In general, there is good agreement between the predicted and the experimental values, with a reduction in the critical force, P_{crit}, with increasing impact angle.

Figure 4.25 compares the experimental and predicted critical forces to cause damage in these laminate. From the figure, there is good agreement between the predicted

and the experimental values, with a reduction in the critical force with increasing impact angle.

Table 4.2 The average experimental and predicted values for P_{crit} for an 8-ply GFRP laminate.

Impact angle (°)	P_{crit} **(Experimental*) (N)**	P_{crit} **(Prediction) (N)**
0	1387 ± 23	1298
10	1280 ± 6	1278
20	1219 ± 4	1220

Note (*): The experimental values listed are the normal forces.

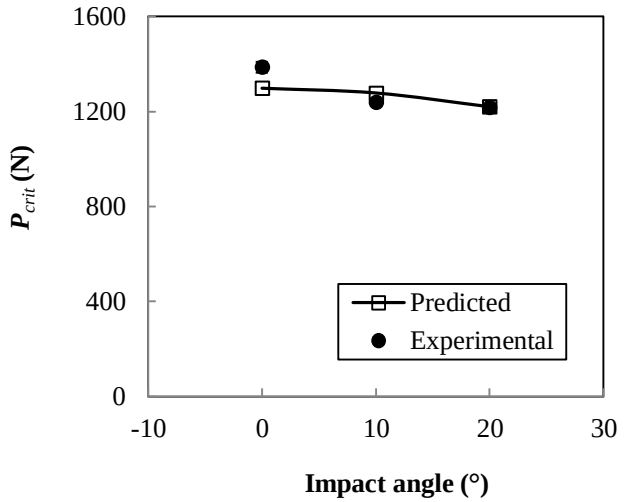

Figure 4.25 The variation of the damage threshold force, P_{crit} , with inclination angle showing both the experimental results and the predictions offered by the Sutherland and Soares model (solid line) [5].

4.2 Normal and Oblique Impact Response of Foam-Based Sandwich Structures

In this section, the results obtained from drop-weight impact tests at normal (0°) and oblique impact angles (10° and 20°) on four different polymer foam-based sandwich plates are presented. As discussed in Chapter III, the foam cores used in this research project were based on two densities of linear PVC core, having the commercial names of Airex R63.80 and Airex R63.140. These foams have nominal densities of 90 kg/m³ and 140 kg/m³ respectively. Tests were also undertaken on two types of

PET foam, these being Airex T92.100 and Airex T92.130 with nominal densities of 115 kg/m^3 and 135 kg/m^3 respectively.

4.2.1 Normal and Oblique Impact Response of Linear PVC (R63.80) Sandwich Structures

This section is divided into two parts: the first presents the findings from quasi-static indentation tests, whilst the second presents the findings from impact tests at energies up to 20 J, from initiation of damage up to perforation.

4.2.1.1 Theoretical predictions for the impact response of the linear PVC (R63.80) sandwich structures using an energy-balance model

4.2.1.1.1 Determination of the contact parameters

According to the literature, the indentation responses for sandwich structures differ significantly from monolithic laminates, with the former being dominated by the properties of the core materials. For a given force level, the indentation force of the sandwich structure is much higher than that for a monolithic laminate, since the foam undergoes crushing and densification during the indentation test, which gives a stiffening effect under the point of contact [11].

Typical load-indentation traces for the linear PVC (R63.80) sandwich panels subjected to static indentation tests at 0°, 10° and 20° inclination angles are shown in Figure 4.26. For the 0° case, the slope of the load-indentation curve is the steepest, with a maximum indentation of 0.23 mm, indicating direct contact between the indenter and the target (sandwich panel) ; whereas, for the 20° case, the slope is more shallow, with a maximum permanent depth of indentation being approximately

0.5 mm. The 10° case shows an intermediate behaviour in terms of the slope, with the maximum permanent depth of indentation being 0.26 mm.

Using a similar approach to that in Section 4.1.1.1, the contact stiffness, *C*, and the indentation exponent, *n*, was determined experimentally for all the sandwich structures studied. These values were obtained from a series of static indentation tests (with the use of a solid support) as well as static flexural testing, as described previously in Section 3.5, at a cross-head displacement rate of 1 mm/min. Static flexural tests were undertaken to determine the value of bending/shear stiffness, $K_{b/s}$, that is required in the energy-balance model.

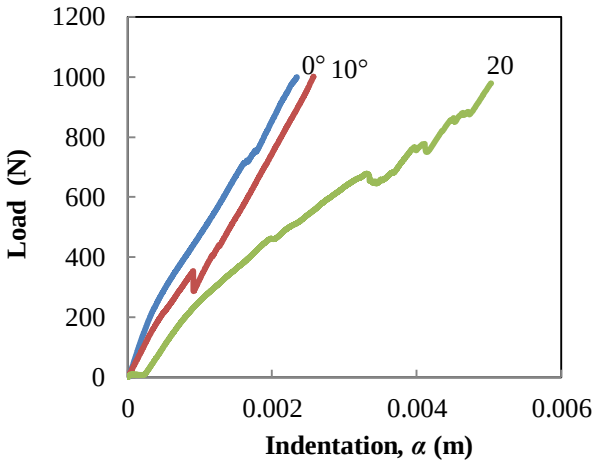

Figure 4.26 Typical load-indentation traces for the linear PVC (R63.80) sandwich foam panels following static indentation testing at a crosshead displacement rate of 1 mm/min and at normal, 10° and 20° inclination angles.

The contact stiffness, *C*, and the indentation exponent, *n*, were determined. As shown in Figure 4.27, the values of *C*, were found to decrease with inclination angle, giving the values of 4.88 x10^5 N/m^n (0°), 3.66 x10^5 N/m^n (10°) and 2.12 x 10^5 N/m^n (20°). These results show similar trends to those observed in the laminated composite system, in Figure 4.2 (a). However, the laminated composites exhibit superior contact stiffness, with the values being 22.9 x10^6 N/m^n, 7.59 x10^6 N/m^n and

7.5 x10^5 N/m^n at 0°, 10° and 20° inclination angles. This is expected, since it is well understood that the material properties directly influence the overall stiffness of the structure, as well as the contact stiffness of the component. This, in return, affects the dynamic response of the target under impact loading.

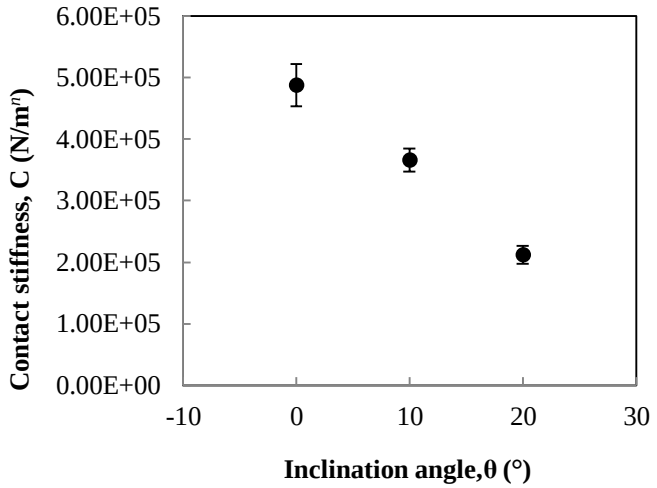

Figure 4.27 Average values of the contact stiffness, *C*, for the linear PVC R63.80 sandwich panels following static indentation loading at increasing inclination angles.

For the indentation exponent, *n*, this type of sandwich structure is close to 1.0 for both the 0° and the 10° impact cases, as shown in Figure 4.28; at a higher inclination angle of 20°, the *n* value is reduced to about 0.97. Compared with those of the laminated composites in Figure 4.2 (b), it is apparent that the values of *n* are much lower than those of the laminated composites. This is expected, since this type of material exhibits a poor resistance to indentation loading in comparison to an isotropic solid. In addition, these *n* values do not greatly differ at each inclination angle, in passing from 0° to 20, for both types of composite structures. These observations suggest that the indentation exponent, *n*, does not show any clear sensitivity to inclination angle.

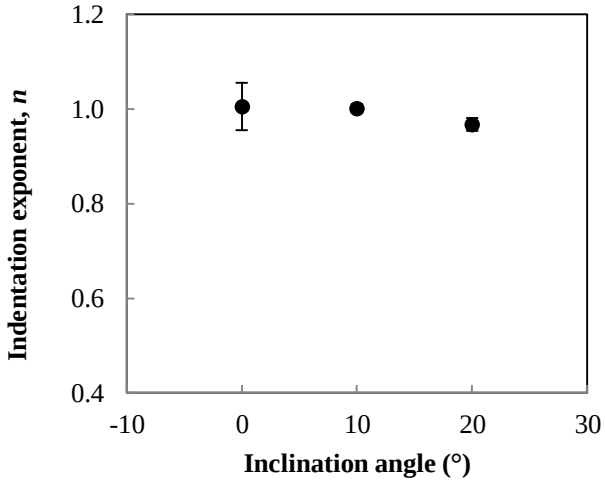

Figure 4.28 Average values of the indentation exponent, *n*, for the linear PVC R63.80 sandwich panels following static indentation loading at increasing inclination angles.

4.2.1.2 Experimental results following normal and oblique impact tests on linear PVC (R63.80) sandwich plates

The results following a series of drop-weight impact test on the linear PVC (R63.80) subjected to 0°, 10° and 20° inclination angles up to 20 J are presented and discussed in this section, with the main results listed in Tables 4.3 and 4.4.

A similar approach to the laminated composites in Section 4.1 has been adopted to discuss the impact response of the foam-based sandwich structures. In general, it has been reported that linear PVC foam-based sandwich structures exhibit a ductile behaviour [10], in comparison to that of the PET foam-based sandwich structures, which are reported to exhibit brittle failure, as reported by Hassan [13]. Therefore, the behaviour of both types of material when subjected to normal and oblique impact is discussed in this the section, from relatively low energies (2.5 J) up to perforation of the top skin (20 J). Examples of typical load-time traces are presented in Figures 4.29 and Figure 4.30 following impact at 10 J and 20 J.

Table 4.3 Experimental results following a series of normal and oblique impact tests on linear PVC (R63.80) sandwich structures at normal and oblique angles.

Impact angle (°)	**Impact energy (J)**	**P_{max} (N)**	**F_N (N)**	**Absorbed energy (J)**
0°	2.5	896 ± 48	896	0.8 ± 0.01
	5	1298 ± 80	1298	1 ± 0.01
	10	1931 ± 95	1931	3.5 ± 0.02
	15	2019 ± 135	2019	5.7 ± 0.02
	20	2221 ± 160	2221	8.5 ± 0.13
10°	2.5	907 ± 30	875	0.8 ± 0.06
	5	1313 ± 40	1266	1.4 ± 0.04
	10	1612 ± 60	1555	4 ± 0.01
	15	1820 ± 110	1755	6.9 ± 0.04
	20	2063 ± 140	1990	11.5 ± 0.59
20°	2.5	715 ± 50	686	2.1 ± 0.13
	5	1087 ± 110	1043	4.6 ± 0.05
	10	1292 ± 150	1240	8.2 ± 0.02
	15	1509 ± 110	1448	10 ± 0.71
	20	2030 ± 180	1948	11.8 ± 1.09

Table 4.4 Detail damage characteristics in the linear PVC (R63.80) sandwich structure following normal and oblique impact up to 20 J.

Impact angle (°)	**Impact energy (J)**	**Damage area (mm^2)**	**Max. depth of permanent indentation (mm)**
0°	2.5	66 ± 4	0.18 ± 0.01
	5	62 ± 5	0.10 ± 0.01
	10	176 ± 8	0.63 ± 0.03
	15	474 ± 6	1.99 ± 0.03
	20	760 ± 4	3.96 ± 0.02
10°	2.5	58 ± 3	0.17 ± 0.01
	5	88 ± 9	0.30 ± 0.03
	10	184 ± 10	0.54 ± 0.03
	15	448 ± 5	1.85 ± 0.02
	20	504 ± 45	3.40 ± 0.30
20°	2.5	60 ± 2	0.08 ± 0.00
	5	136 ± 9	0.15 ± 0.01
	10	240 ± 10	0.15 ± 0.01
	15	284 ± 19.5	0.21 ± 0.01
	20	316 ± 17.9	0.53 ± 0.03

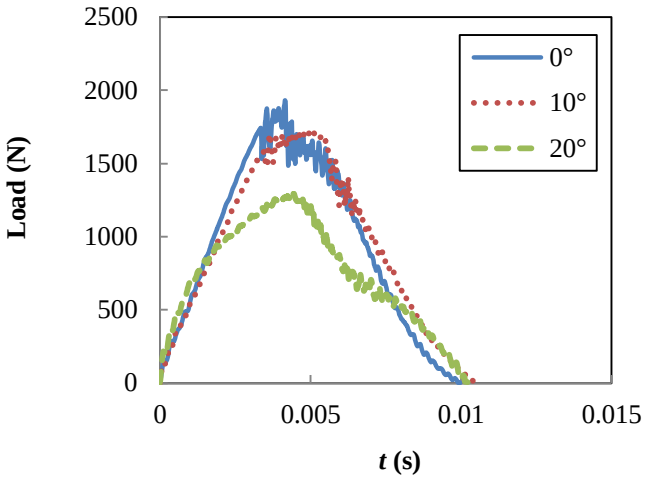

Figure 4.29 Load-time traces for the linear PVC R63.80 sandwich structures subjected to normal and oblique impacts at 10 J.

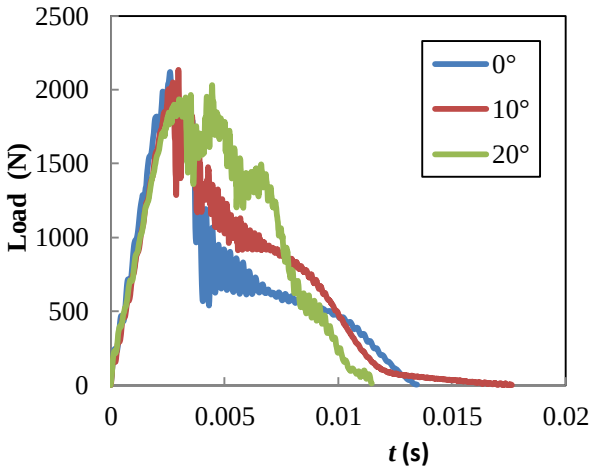

Figure 4.30 Load-time traces for the linear PVC R63.80 sandwich structures subjected to normal and oblique impacts at 20 J.

In general, all of the impact cases have a contact time of approximately 1 ms. It is apparent that the 0° impact response exhibits the highest force in comparison to the response at other inclination angles. This is expected, since it has been found that the contact stiffness is highest at this inclination angle (Figure 4.27); therefore the resultant dynamic force, when subjected to impact loading, is also higher compared to the values at other inclination angles.

In addition, both the 0° and 10° impact cases show a slight load drop in the load-time traces, suggesting the beginning of visible damage in the sandwich structures. However, the 20° impact shows relatively smooth curve during both loading and unloading regime, an indication of an elastic response. In addition, the maximum force, P_{max}, is the lowest overall. These observations are similar to those following normal and oblique impact tests on the laminated composites, as discussed in Section 4.1, where it has been observed that the force reduces in passing from 0° to 20°. Moreover, due to geometrical effects, at angles other than 0°, the measured force in the impact direction (F_s) reduces with the presence of other force components acting in the normal (F_N), as well as in the horizontal direction (F_H) to the impact surface [1].

Referring to Figure 4.30, at 20 J, which is the highest energy level considered for this sandwich structure, there is a more significant load drop in the load-time traces for all the inclination angles. Here, both 0° and 10° impacts exhibit large load drops. The contact time has also increased compared to the 10 J impacts, whereby the maximum contact time is close to 2 ms, which is double the time required for the 10 J case. This suggests significant permanent damage in the sandwich structures. This will be discussed in detail in a later section using evidence from optical micrographs of the cross-sections of the sandwich structures.

Typical load-displacement traces and the corresponding energy-time traces following normal impact on the linear PVC (R63.80) sandwich panels at selected energies are presented in Figure 4.31, Figure 4.32 and Figure 4.33.

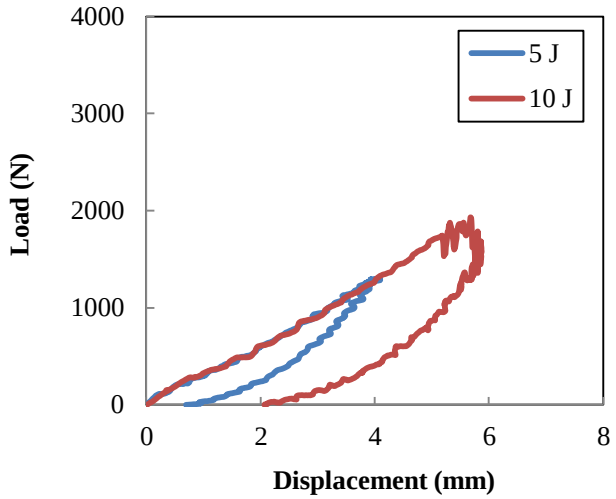

Figure 4.31 Load-displacement traces for the linear PVC (R63.80) sandwich panel following normal impact at 5 J and 10 J.

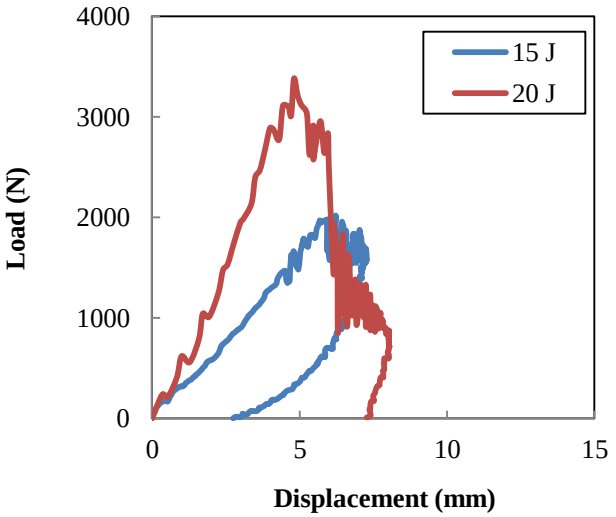

Figure 4.32 Load-displacement traces for the linear PVC (R63.80) sandwich panel following normal impact at 15 J and 20 J.

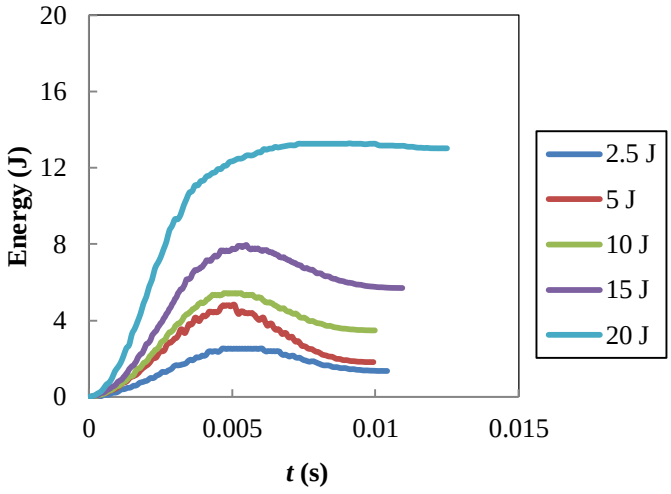

Figure 4.33 Energy-time traces following a normal impact on the linear PVC (R63.80) sandwich structures.

At low energy of 5 J in Figure 4.31, with increasing impact force and the residual displacement of 2.25 mm, the area under the load-displacement also increases, which is an indication of an increase in energy absorption, as evident in the corresponding energy-time traces in Figure 4.33 and the energy absorbed vs. impact energy in Figure 4.40 (page 139).

With increasing impact energy, i.e. at 10 J, the load-displacement traces show a small load drop, which is an indication of the damage threshold at this energy level. In addition, the area under the load-displacement area also increases, with the residual displacement of 2.2 mm.

At 15 J, there is a start of load-drop in the load-displacement traces following normal impact on the linear PVC (R63.80) sandwich structures, which possibly correspond to partial perforation of the indenter onto the top skin. Following a 20 J impact, as given in Figure 4.32, with significant increase in the peak force, there is a large load drop apparent in the load-displacement traces. Again, similar to the case of monolithic laminates, an indication of a severe permanent damage is possible, leaving greater residual displacement (approximately 7.3 mm). In addition, with a larger area under the load-displacement traces, an increase in the energy absorption capability of the sandwich structure is seen, as evident in Figure 4.33 from the plot of the energy-time traces, and in the energy absorbed vs. impact energy in Figure 4.40.

Figure 4.33 depicts the corresponding energy-time traces following normal impact on the linear PVC (R63.80) sandwich structures. At energies up to 15 J, significant rebound energy is present. These observations are associated with rebounding of the

indenter. At 20 J, where plastic deformation occurs, the majority of the imparted energy is absorbed by the panel; hence, leaving only a marginal amount of rebound energy.

Typical load-displacement traces and the corresponding energy-time traces following a 10° impact on the linear PVC (R63.80) sandwich structures are given in Figures 4.34- 4.36. Similar trend to those observed in the normal impact cases are apparent, at relatively low and high energy up to 20 J.

However, larger residual displacements are observed with increasing inclination angle, in passing from 0° to 10°. As an example, at 10 J, the residual displacement is approximately 2.2 mm following a normal impact whereas the value for the 10° impact case is approximately 3.2 mm.

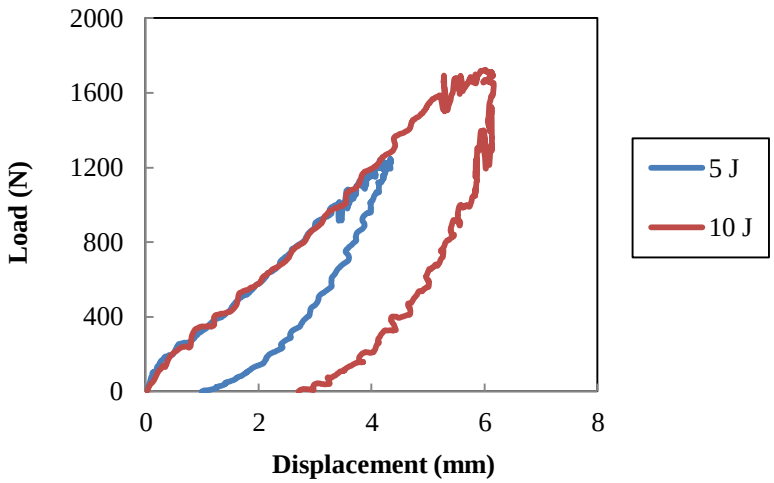

Figure 4.34 Load-displacement traces for the linear PVC (R63.80) sandwich panel following a 10° impact at 5 J and 10 J.

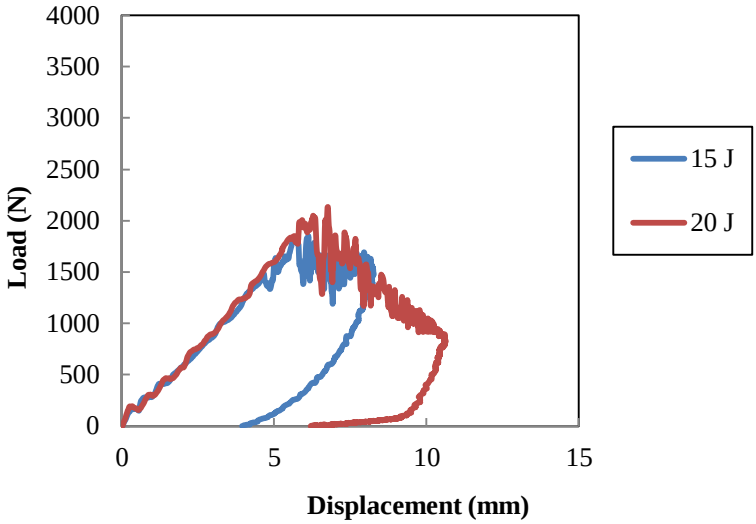

Figure 4.35 Load-displacement traces for the linear PVC (R63.80) sandwich panel following a 10° impact at 15 J and 20 J.

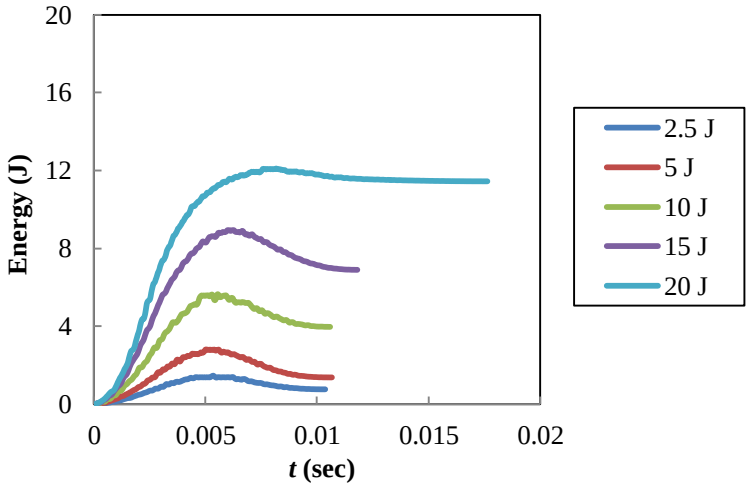

Figure 4.36 Energy-time traces following a 10° impact on the linear PVC (R63.80) sandwich structures.

At higher energy, particularly at 20 J, a significant load drop is apparent, an indication of severe damage in the sandwich structure. The residual displacement for this case is 6.5 mm. As with the normal impact case, the area under the load-displacement increases with an increase in the maximum impact force and residual displacement, suggesting an increase in the energy absorption characteristics of the sandwich structure, as evident in the plot of energy-time in Figure 4.36 and the absorbed energy vs. impact energy, in Figure 4.40.

Figure 4.36 depicts the corresponding energy-time traces following 10° impact on the linear PVC (R63.80) sandwich structures. A similar trend to that of the normal impact cases was observed. At energies up to 15 J, considerable rebound energy is present. These observations are associated with rebounding of the indenter. At 20 J, where plastic deformation occurs, the majority of the imparted energy is absorbed by the panel; hence, leaving only a marginal amount of rebound energy.

Typical load-displacement traces and the corresponding energy-time following a 20° impact at selected energies are presented in Figures 4.37 - 4.39. At relatively low energy, i.e. ≤ 10 J, the load-displacement traces show an almost smooth curve, suggesting a linear elastic response. However, in comparison to the results from 0° and 10° impact, the residual displacement is greatly increased. As an example, at 10 J, the residual displacement is approximately 9.7 mm, in comparison to only 2.2 mm (Figure 4.31), and 3.2 mm (Figure 4.34) for the 0° and 10° impact case respectively. With increasing impact energy, i.e. 20 J, with the start of large load drop in the load-displacement traces, an indication of permanent deformation in the sandwich structure, the residual displacement is reduced to only about 8.0 mm.

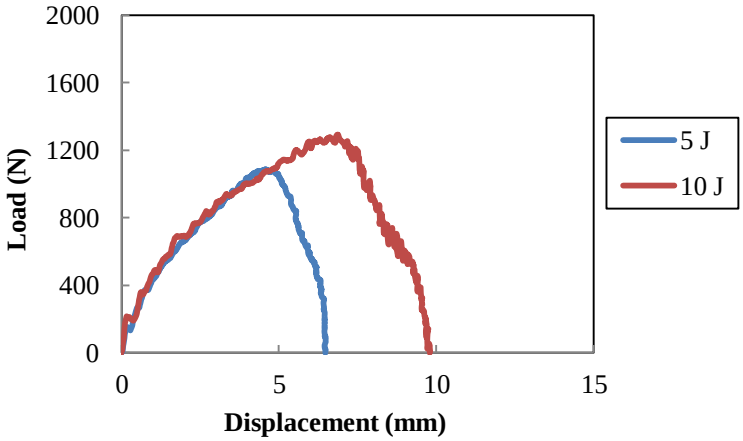

Figure 4.37 Load-displacement traces for the linear PVC (R63.80) sandwich panel following a 20° impact at 5 J and 10 J.

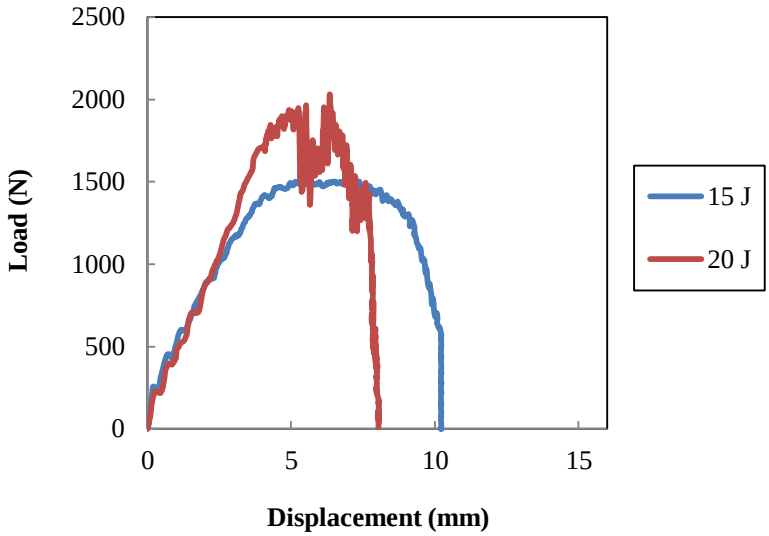

Figure 4.38 Load-displacement traces for the linear PVC (R63.80) sandwich panel following a 20° impact at 15 J and 20 J.

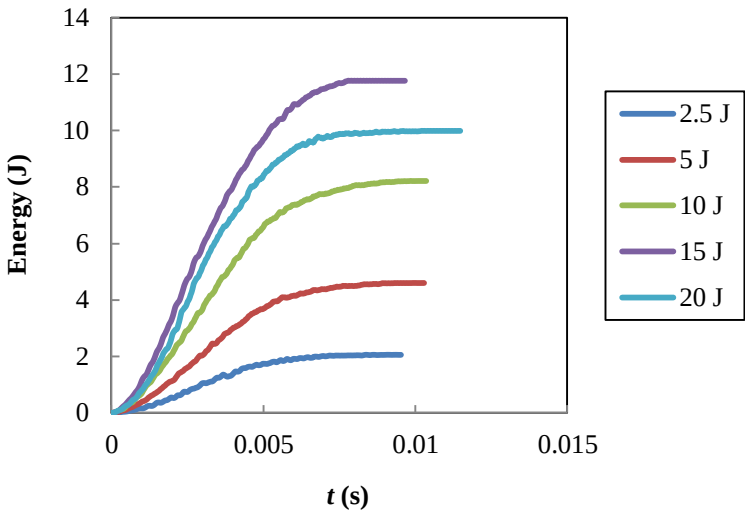

Figure 4.39 Energy-time traces following a 20° impact on the linear PVC (R63.80) sandwich structures.

The corresponding energy-time traces following a 20° impact at energies up to 20 J are given in Figure 4.39. From the results, as observed in the load-displacement traces, from the plot of energy-time, the majority of the impact energy is absorbed by the sandwich structure, as compared to the results for the 0° and the 10° impact case (Figure 4.33 and Figure 4.36), hence the rebound energy is marginal. Again, this observation is possibly due to the effect of geometry, with more kinetic energy transferred to the indenter at this high inclination angle; therefore, an increase in

absorbed energy is expected. Overall, similar to the trends in the monolithic laminate, it has been observed that the effect of obliquity is apparent on the indenter residual displacement, as a result of a force reaction, F_H, in the horizontal direction.

Figure 4.40 presents the energy absorption characteristics of the R63.80 sandwich structures, showing an increase in energy absorption with impact energy. As evident in the energy-time plots following normal impact (Figure 4.33), 10° impact (Figure 4.36) and 20° impact case (Figure 4.39), the energy absorbed increases with increase in impact energy.

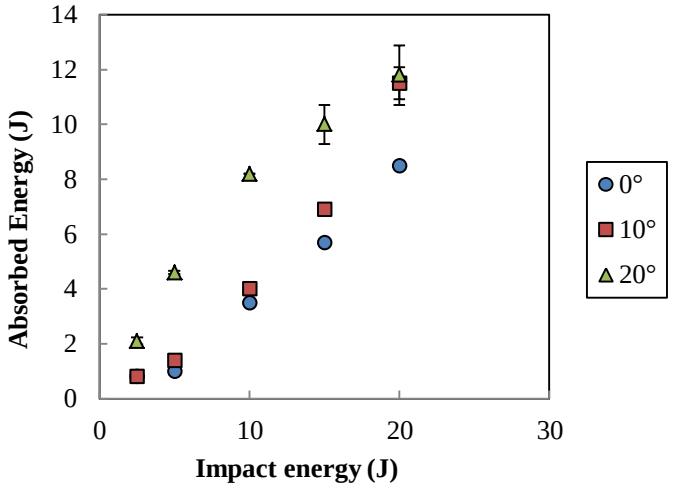

Figure 4.40 Absorbed energy against impact energy following normal and oblique impact on linear PVC (R63.80) sandwich structures.

In addition, the energy absorbed is highest for the obliquely-impacted sandwich structures, i.e. at 20°, as observed in the results for an 8-ply GFRP laminate (Figure 4.17). Again, these observations are possibly due to geometric effects, since it was argued that, for non-normal impact, particularly at high angles of obliquity, more kinetic energy is transferred from the indenter to the target, in comparison to that of the normal impact case [4].

The maximum impact force, P_{max}, and the corresponding normal force, F_N, following normal and oblique impact on the linear PVC (R63.80) sandwich structures are presented in Figure 4.41 and Figure 4.42.

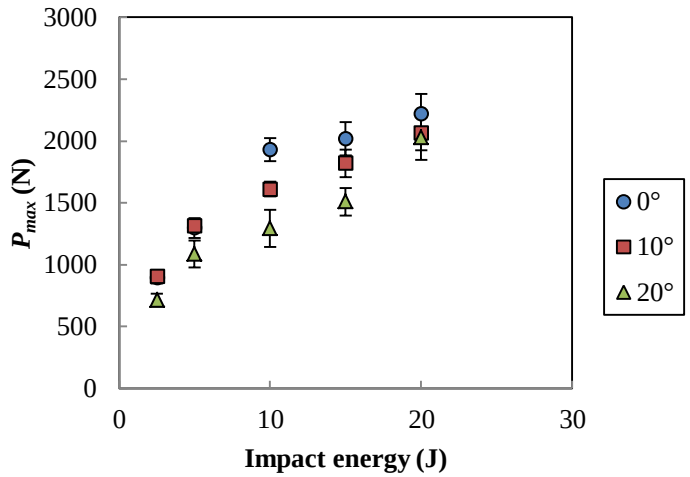

Figure 4.41 Maximum impact force against impact energy following normal and oblique impact on the linear PVC (R63.80) sandwich structures.

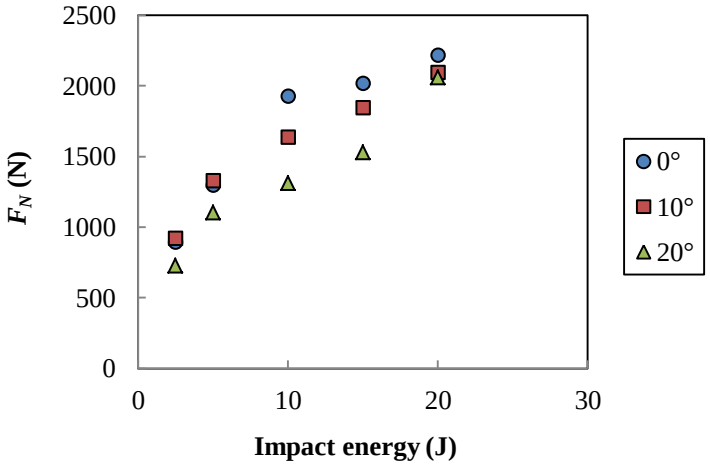

Figure 4.42 Calculated maximum normal force, F_N, against impact energy following normal and oblique impact on the linear PVC (R63.80) sandwich structures.

From Figure 4.41, the maximum impact force gradually increases with impact energy for the three inclination angles. In addition, for the 0° and 10° impact cases, the values show an increase with energy up to the onset of damage, i.e. 10 J.

Above this energy level, there is only a small increase in the maximum impact force with increasing energy up to 20 J, which plateaued at approximately 2200 N. The 20° impact, however, continued to increase, even at this energy level. This is expected, since this structure has not reached its maximum strength even at this energy level, with the maximum impact force being approximately 2000 N (20 J).

The corresponding calculated maximum normal force for three inclination angles is presented in Figure 4.42, showing similar trends to the maximum impact force. Again, the 20° impact exhibits the lowest maximum normal force.

Using the same concept as proposed by Yang and Cantwell [11], the onset of damage has been determined from visual observations on the test panels following normal and oblique impact subjected at energies up to 20 J, in which the start of damage is considered as the level of energy causing visible damage, typically in the form of delamination on the surface of the impacted panel.

Table 4.4 lists the measured damage area and the maximum depth of permanent indentation following normal and oblique impact on the linear PVC (R63.80) sandwich structures. The measured damage area is plotted against impact energy, as shown in Figure 4.43. Here, similar trends to those recorded in the maximum impact force are observed for both the 0° and the 10° impact cases, showing a gradual increase up to the onset of damage, at 10 J. Beyond this point, between 10 J and 15 J, a large increase in the measured damage area is apparent, which is approximately 300 mm^2, passing from 10 to 15 J for these two impact cases.

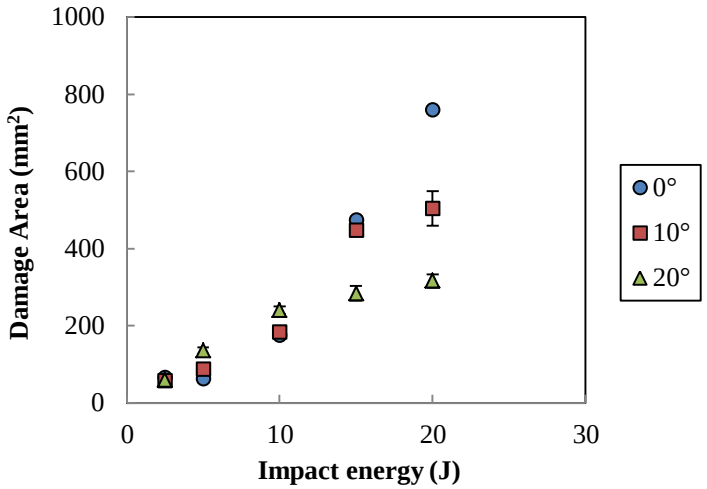

Figure 4.43 Damage area against impact energy following normal and oblique impact on the linear PVC (R63.80) sandwich structures.

Lastly, from 15 to 20 J, the increase in damage area measured on the impact surface of the indenter is similar to that observed from 10 to 15 J. As expected, due to lower contact stiffness, which affects the maximum impact force, at higher obliquity (20°), the corresponding damage area is also relatively small in comparison to the other two impact cases, with the trend showing a gradual increase in the size of the damage area up to 20 J. Again, the visible damage observed in the form of delamination in the upper skin is mainly attributed to shearing effects. These characteristics are also apparent when the results are compared with those of the laminated composites, as given in Figure 4.20. Clearly, greater damage area is observed in the linear PVC R63.80 sandwich structures relative to the 8-ply GFRP laminate, over the range of impact energies studied, regardless of whether the test was conducted at normal or other inclination angles.

Figure 4.44 shows a plot of the maximum depth of permanent indentation as a function of impact energy for the linear PVC (R63.80) sandwich structures subjected to normal and oblique impact. It appears that for the normal impact, maximum

permanent indentation increases dramatically with impact energy up to 20 Joules, with a maximum depth of permanent indentation of 3.96 mm, which is almost eight times the depth of the permanent indentation observed in the GFRP laminate, with the value of 0.50 mm at 20 J following a normal impact.

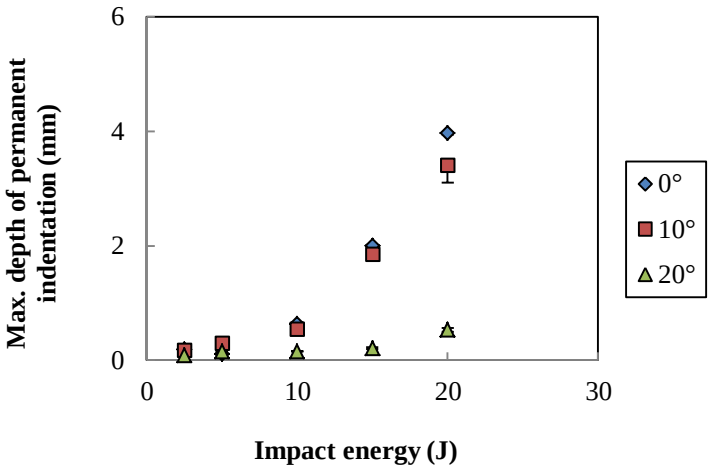

Figure 4.44 Maximum depth of permanent indentation vs. impact energy following normal and oblique impact on the linear PVC (R63.80) sandwich structures.

Similar trends to the 0° impact are observed in the plot for the 10° impact, at energies up to 20 J, with the maximum depth of the permanent indentation being approximately 3.40 mm. In comparison to the measured depth of permanent indentation present in the GFRP laminate, this value is about four times greater, at a similar energy level (20 J).

For the 20° impact case, it has been observed that the measured maximum depth of permanent indentation is much higher than that of the laminated composites, with the value being 0.53 mm, in comparison to only about 0.09 mm for the laminated composites, as listed in Table 4.4.

These observations suggest a reduction in the material overall stiffness due to the presence of a foam core, in comparison to that of the monolithic laminate. This is expected since, according to the literature, damage or failure in sandwich structures depends on the shear stiffness of the core, which is a dominant factor in the transfer of stress from top skin to the core then to the lower skin [13].

Figure 4.45 shows photographs of the impact surface following a 20-J impact on the linear PVC (R63.80) sandwich structure at an inclination angle of 0°, 10 and 20°. For the normal impact, as in Figure 4.45(a), the impact surface shows evidence of a small diameter indenter, with the shape being peanut-like, causing permanent indentation of the top skin. A similar damage pattern is observed for the 10° impact, as shown in Figure 4.45(b). The 20° impact surface shows a much smaller damage size, with the shape being more elliptical, due to an elliptic contact surface. In addition, a smaller amount of damage could also be attributed to lower contact stiffness, which results in the lower force magnitude acting on the target (sandwich structure), as shown in Figure 4.45(c).

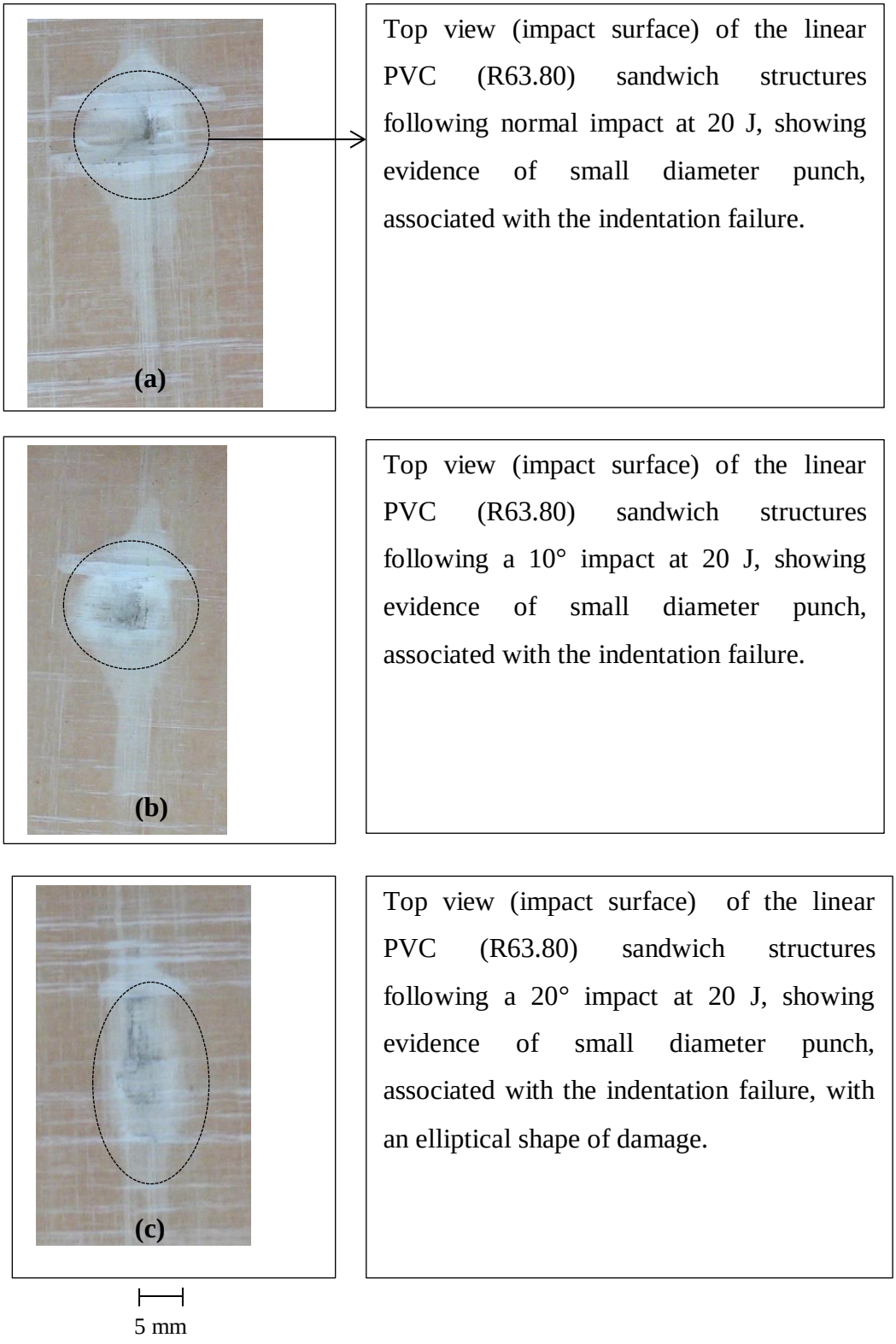

Figure 4.45 Photographs showing the impact surface following a 20 J impact on the linear PVC (R63.80) sandwich structures oriented at (a) 0°; (b) 10° and (c) 20°.

More detailed information about the failure behaviour of the three panels is gathered from the optical micrographs, showing the cross-sections of the impacted linear PVC R63.80 sandwich panels subjected to 20 J at normal, 10° and 20° impact angles, as given in Figure 4.46. In general, at 20 J, the sandwich structures subjected to both the 0° and 10° exhibit upper skin failure and core shear rupture.

Close examination of the micrographs shows that normal impact, as evident in Figure 4.46 (a) exhibits similar fracture behaviour on the top skin to that as in the 8-ply GFRP laminate, in Figure 4.23 (a). However, due to the thinner layer of the skin (4-ply on top skin in comparison to 8-ply), this lead to further damage in the foam core. The crack propagation path initiated at the point where fibre fracture occurs. At the same time, internal crack propagation is also observed, probably due to the internal stress created during impact loading. Further crack propagation is observed reaching to a maximum depth of permanent indentation of 3.96 mm from the top surface, which is almost a quarter of the total thickness of the sandwich panel, as evident in Figure 4.46 (a). The rough fracture surface indicates ductile failure.

With increasing inclination angle, at 10°, in Figure 4.46 (b) less severe damage is apparent in the core structure, indicating the influence of the shear stress. Moreover, the top skin fractures in a similar manner as in Figure 4.23 (b) of the 8-ply laminated composites, with full penetration of the top skin, due to lower stiffness of the materials with reducing number of plies (4-ply vs. 8-ply). For this case, the maximum depth of permanent indentation is slightly reduced to about 3.40 mm. These findings are consistent with the combination of compression, tensile and shear, as given in Figure 4.23 (b).

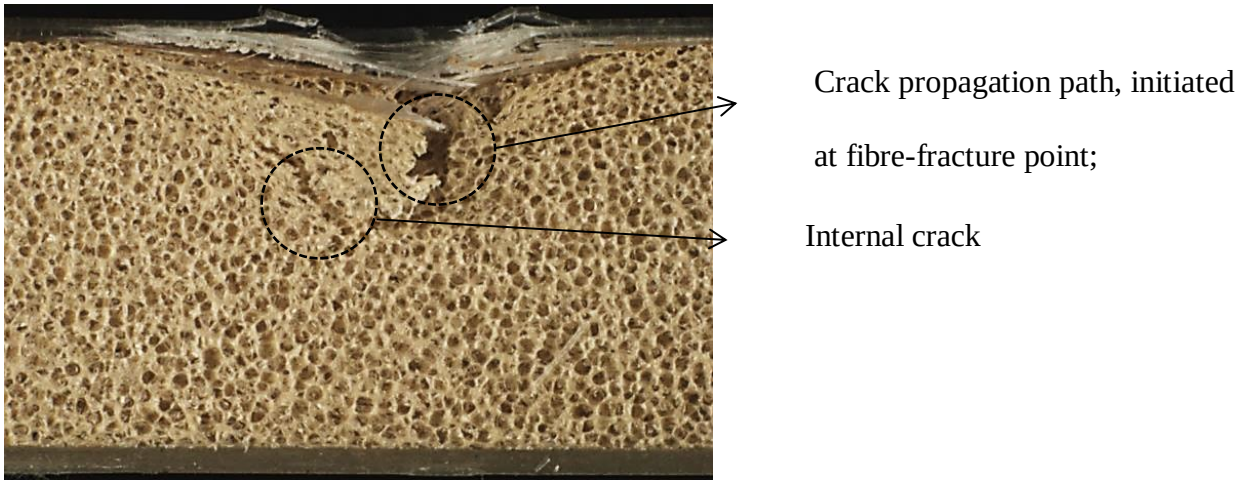

(a) 0°

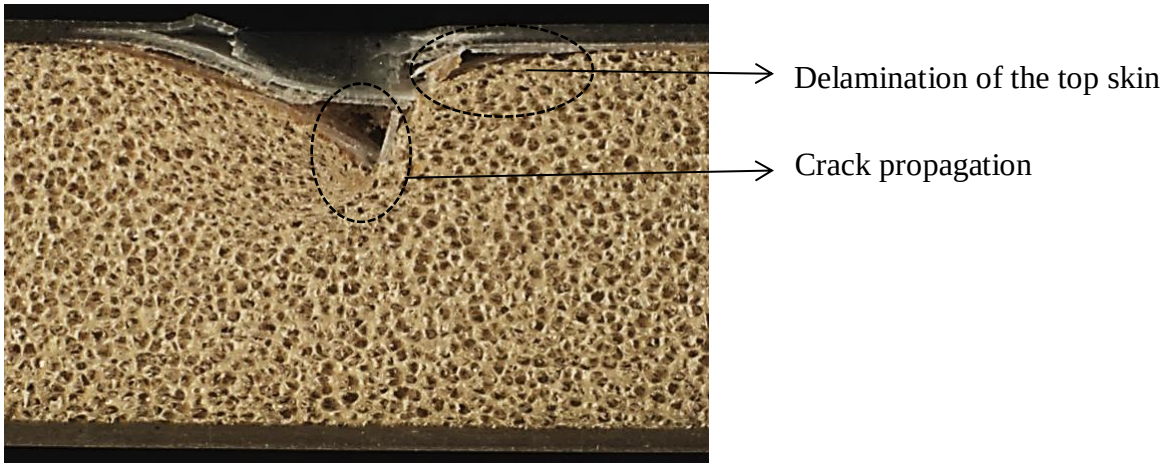

(b) 10°

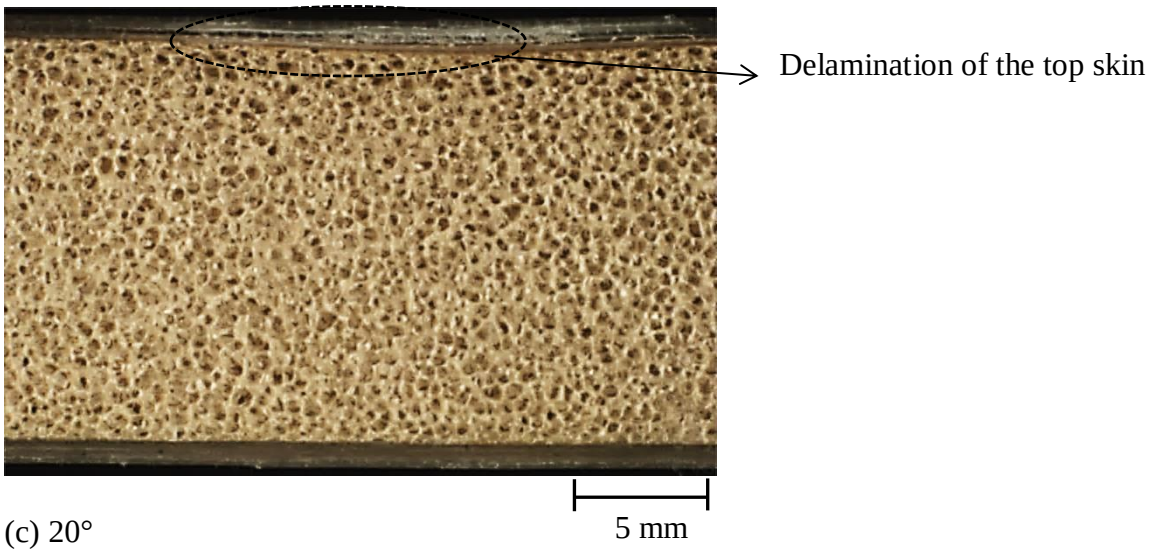

(c) 20°

Figure 4.46 Optical micrographs of the linear PVC (R63.80) sandwich panels showing cross-sections of the impacted surface following impact at 20 J with impact angles of (a) 0° ;(b) 10° and (c) 20°.

At the cross-section, for the 20° impact, there is only the presence of delamination in the upper skin, with no visible damage to the core, as observed in Figure 4.45 (c) and Figure 4.46 (c). In summary, it has been observed that the linear PVC (R63.80) sandwich structures exhibit similar trend to that observed in the monolithic laminate (8-ply GFRP laminate), when subjected to normal and oblique impact at energies up to 20 J. However, the force magnitudes are relatively much lower, with larger displacement, and much greater damage in the form of penetration in the upper skin and core shear rupture for both the 0° and 10° impact cases, whilst the 20° impact caused relatively small delaminations in the upper skin with a marginal depth of permanent indentation, which is less than 1 mm.

4.2.1.3 Comparison between experimental and theoretical results

The maximum impact force obtained experimentally, as well as the predictions offered by the energy-balance model for the linear PVC R63.80 sandwich plates subjected to normal and oblique impact are presented in Figure 4.47.

Up to the onset of damage, which is approximately at 10 J, it appears that there is good agreement between the experimental values and the predictions, with the maximum difference of about 15%, 10% and 20% following impacts at 0°, 10° and 20°, respectively.

Above this threshold, the model tends to over-predict the maximum impact force, with the maximum difference being approximately 30%, 20% and 30 % for inclination angles of 0°, 10° and 20°, respectively, as was observed earlier for the GFRP laminate.

These observations suggest that it is possible to use an energy-balance model to predict the impact response at normal and non-normal (oblique) angles, particularly at low energies, i.e. (< 10 J) with the parameters determined experimentally from a series of quasi-static tests.

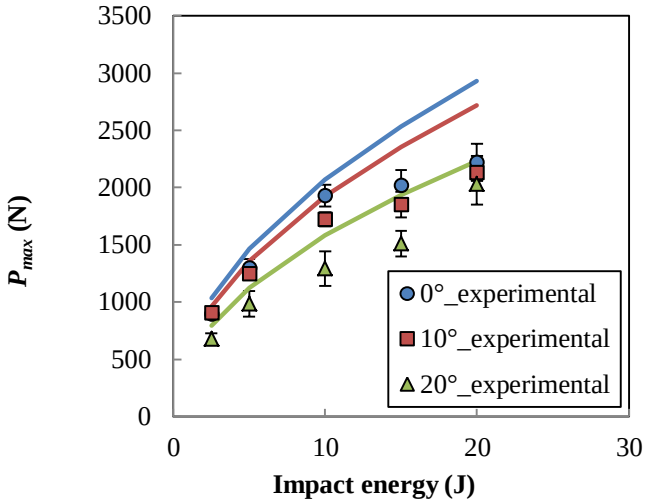

Figure 4.47 Experimental and predicted maximum impact force (solid line) for the linear PVC R63.80 sandwich plates subjected to normal and oblique impact.

4.2.2 Normal and oblique impact response of linear PVC (R63.140) sandwich panels

A similar approach to that used for the linear PVC (R63.80) sandwich structures was adopted to present the findings for the highest density foam core sandwich structures, the linear PVC (R63.140), with a nominal density of 140 kg/m^3. It was expected that, with a higher foam density, the contact stiffness, impact properties and damage tolerance would be improved, as well as the energy-absorption characteristics for impact at normal and other inclination angles.

4.2.2.1 Theoretical predictions for impact response of the linear PVC (R63.140) sandwich structures at normal and oblique angles using the energy-balance model.

4.2.2.1.1 Determination of contact parameters

In a similar manner to that adopted for the linear PVC (R63.80) sandwich structures, in order to obtain the contact parameters, the load-indentation curves for the linear PVC (R63.140) sandwich structures was first obtained, as presented in Figure 4.48.

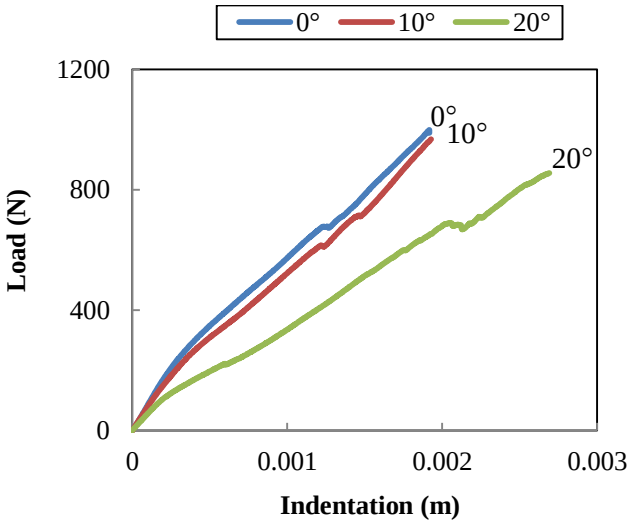

Figure 4.48 Typical load-indentation traces for the linear PVC (R63.140) sandwich foam panels during static indentation testing at a crosshead displacement rate of 1 mm/min and at normal, 10° and 20° inclination angles.

In comparison to the plots for its lower density counterpart (R63.80) in Figure 4.26, the trends are quite similar, with the 0° case exhibiting the highest slope of the load-indentation plot; the 10° case show a similar trend with a slightly lower value. Finally, the 20° impact case exhibits the lowest stiffness, with a maximum indentation of approximately 0.3 mm. Moreover, this suggests an increase in the contact stiffness, *C*, values, regardless of whether the test was tested at 0°, 10° or 20°.

Referring to Figure 4.49, from the plot of contact stiffness, *C*, *vs*. inclination angle, similar trends as reported for the linear PVC (R63.80) sandwich structures are noted, with there being much higher values of *C* for the range of inclination angles studied. For example, for θ = 0°, the contact stiffness for the linear PVC (R63.140) is two times greater than that of the lower density foam core sandwich structures; at 10°, the *C* value is about 2.3 times better than that of the R63.80 sandwich structures and for θ = 20°, the *C* value is about 1.5 times higher than that of the linear density R63.80 sandwich structure.

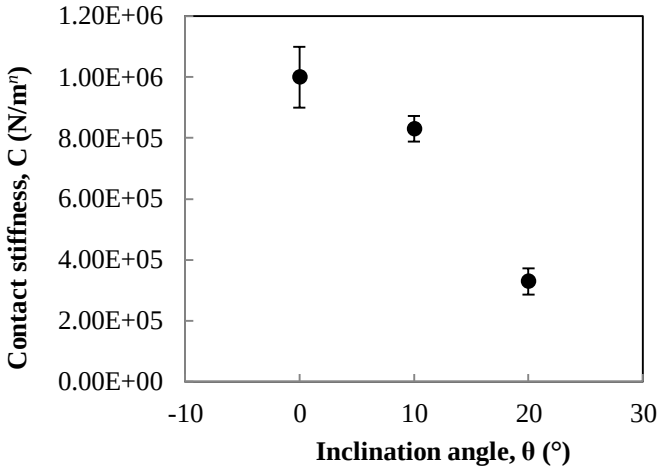

Figure 4.49 Average values of contact stiffness, *C*, for the linear PVC R63.140 sandwich panels during static indentation loading at increasing inclination angles.

The indentation exponent, *n*, values are plotted against inclination angle for the linear PVC (R63.140) in Figure 4.50. In general, similar trends to those of the linear PVC (R63.80) sandwich structures are observed, with the *n* value reducing in passing from 0° to 20° inclination angles.

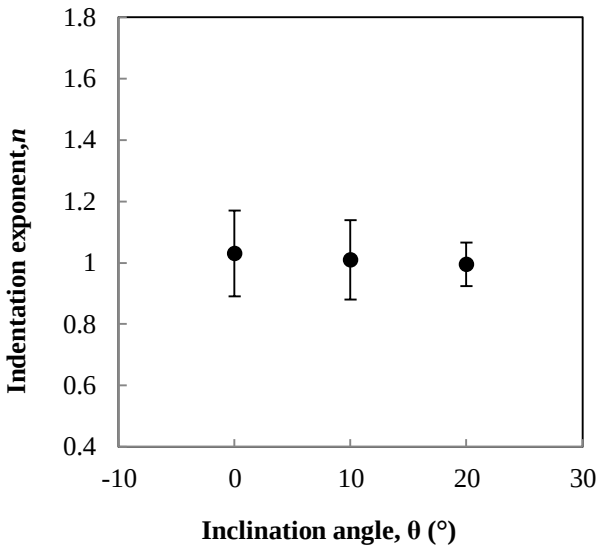

Figure 4.50 Average value of contact parameter, '*n*', for the linear PVC R63.140 sandwich panels following static indentation loading at increasing inclination angles.

The contact properties are listed and summarised in Table 4.5 and Table 4.6. It is evident that the core density has a significant effect on the contact properties of the materials studied, when the contact stiffness and indentation exponent, *n*, values of monolithic laminate (8-ply GFRP laminate), linear PVC (R63.80) and the linear PVC (R63.140) sandwich structures are compared. Regardless of whether the panel is subjected to normal (0°) or oblique inclination angles, the higher density core linear PVC (R63.140) sandwich structures exhibit superior contact stiffness than the lower density linear PVC (R63.80) sandwich structures. However, the rigid monolithic laminate, which is the 8-ply GFRP laminate, exhibits the higher contact stiffness overall.

The contact properties obtained via the experimental tests at 0° inclination angles are compared with those from an earlier work [6] on a similar type of sandwich structure. As given in Tables 4.5 and 4.6, respectively, the value of *C* and *n* are lower than the current values. This is expected, since the differences in boundary

conditions (fully-clamped *vs.* simply supported) during such tests will affect the contact parameters, with the difference typically being approximately 20% [8].

Table 4.5 Contact stiffness of the composites and the linear PVC sandwich structures following static indentation test at 0°, 10° and 20°.

Material system	**Foam core density (kg/m^3)**	**Contact stiffness, *C* x10^6 (N/mm^n)**	
		This study	**Ref [6]**
8-ply GFRP Laminate	-	0° : 22.9±0.15 10°: 7.59±0.10 20°: 0.75±0.05	-NIL-
Linear PVC (R63.80)	90	0° : 0.49±0.03 10°: 0.37±0.02 20°: 0.21±0.01	0.13 (0°)
Linear PVC (R63.140)	140	0° :1.00±0.10 10°: 0.83±0.04 20°: 0.33±0.04	0.2 (0°)

Table 4.6 Indentation exponent, *n*, of the composites and linear PVC sandwich structures following static indentation test at 0°, 10° and 20°.

Material system	**Foam core density (kg/m^3)**	**Indentation exponent, *n***	
		This study	**Ref [6]**
8-ply GFRP Laminate	-	0° : 1.18±0.05 10°: 1.15±0.05 20°: 1.08±0.02	-NIL-
Linear PVC (R63.80)	90	0° : 1.01±0.05 10°: 1.00±0.03 20°: 0.97±0.02	0.85 (0°)
Linear PVC (R63.140)	140	0° : 1.03±0.05 10°: 1.01±0.03 20°: 1.00±0.02	0.90 (0°)

Note:* Static Indentation tests were conducted using a 10-mm hemispherical indenter with a simply supported boundary condition on test panels with dimensions of 200 mm x 20 mm x13 mm.

4.2.2.2 Experimental results following normal and oblique impact tests on linear PVC (R63.140) sandwich plates

The experimental results obtained from a series of drop-weight impact tests at normal and oblique angles on the linear PVC R63.140 sandwich panels are presented in this section. Figure 4.51 and Figure 4.52 show typical load-time plots of the linear

PVC R63.140 sandwich panels subjected to normal and oblique impact at 10° and 20° at 10 and 20 J, respectively. It is apparent that, for both normal and 10° impact, the traces exhibit a load drop above 10 J, which is the damage threshold energy. Indeed, the 10° case shows a relatively large load drop.

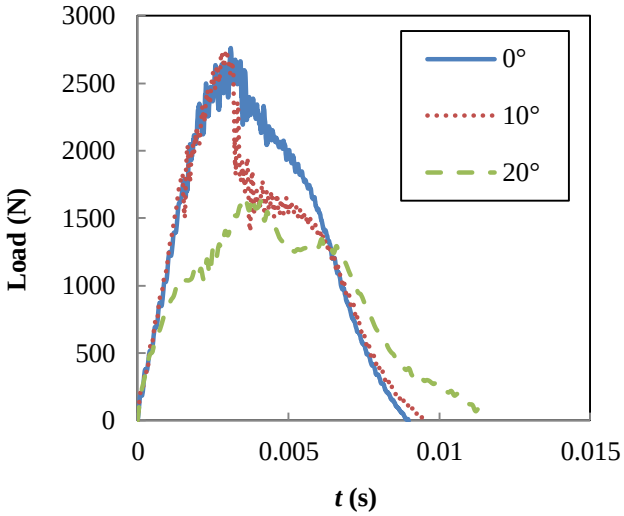

Figure 4.51 Load-time traces for the linear PVC R63.140 sandwich panels subjected to normal and oblique impact at 10 J.

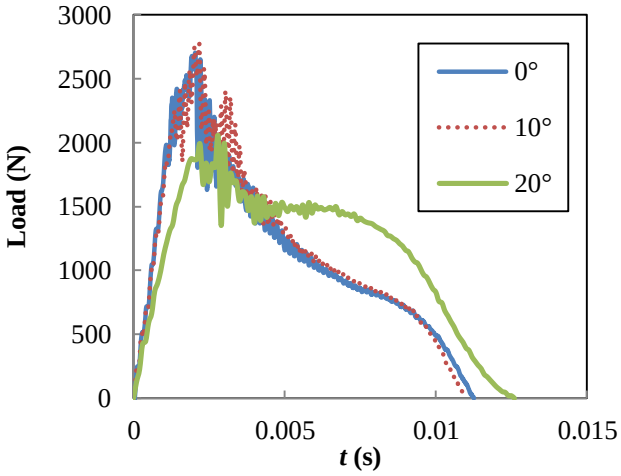

Figure 4.52 Load-time traces for the linear PVC R63.140 sandwich panels subjected to normal and oblique impact at 20 J.

With increasing energy, i.e. at 20 J, both the normal and 10° impact cases resulted in a large load drop. Unlike the behaviour at 10 J, for the 20° impact, there is a load

drop at this energy level, as observed in Figure 4.52, which suggests permanent indentation or severe damage in the sandwich structures. Overall, the trends are similar to those seen in the lower density foam-based (R63.80) sandwich structures, as can be seen in Figure 4.30, where a much shorter total contact time and higher force are apparent.

The load-displacement traces and the corresponding energy-time traces following normal impact on the linear PVC (R63.140) sandwich panels at selected energies are presented in Figure 4.53, Figure 4.54 and Figure 4.55. At a relatively low energy level, i.e. 5 J, the load-displacement traces show a similar trend to that of the linear PVC (R63.80) sandwich structures, with higher peak force and residual displacement of approximately 2.20 mm following a 5 J impact. At this energy level, the material responds elastically, with relatively smooth loading and unloading curve in the load-displacement traces.

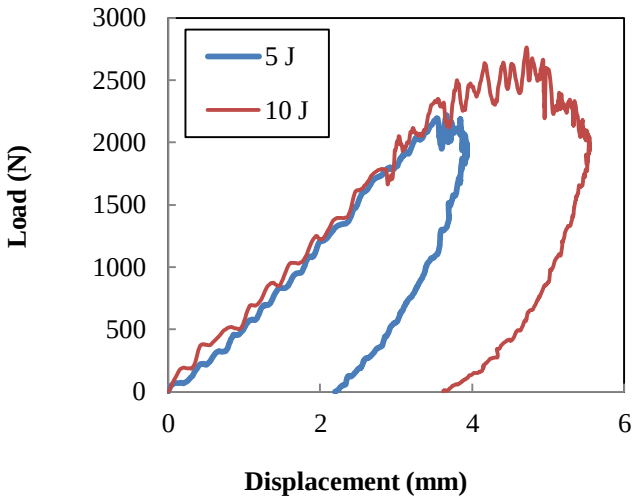

Figure 4.53 Load-displacement traces for the linear PVC (R63.140) sandwich panel following normal impact at 5 J and 10 J.

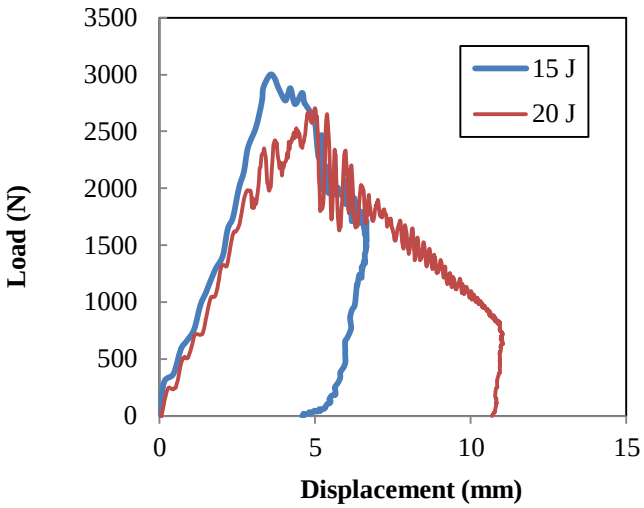

Figure 4.54 Load-displacement traces for the linear PVC (R63.140) sandwich panel following a normal impact at 15 J and 20 J.

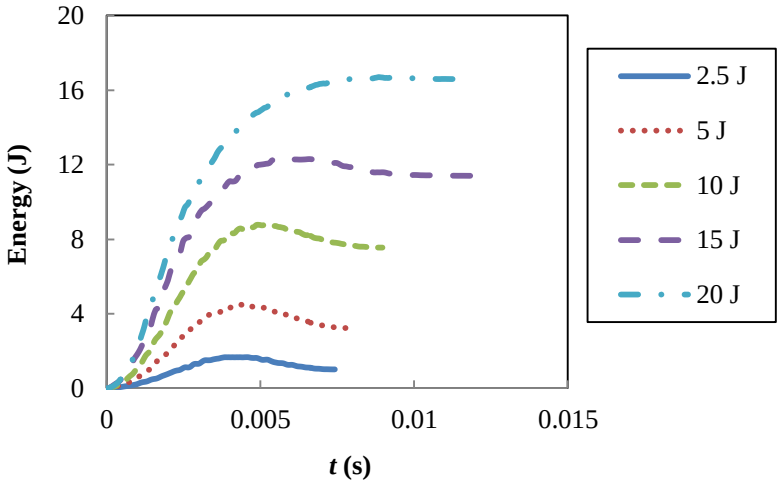

Figure 4.55 Typical energy-time traces for the linear PVC (R63.140) sandwich structures following normal impact.

With increasing impact energy, at 10 J, there is a much higher force value in comparison to that of the impact at 5 J, with an increase in the maximum displacement of 5.5 mm and the residual displacement being approximately 3.61 mm. In addition, a larger area of load-displacement traces suggests an increase in the energy absorbed, as evident in the corresponding energy-time traces in Figure 4.55 and the plot of absorbed energy vs. impact energy in Figure 4.62 (page 162).

Following a 20 J impact, as given in Figure 4.54, the peak force increases significantly in comparison to that of the 10 J case, with a large load drop apparent in the load-displacement traces. Again, similar to the case of monolithic laminate, an indication of severe permanent damage is possible, leaving greater residual displacement, which is approximately 10.69 mm. In addition, with a larger area under the load-displacement traces, an increase in the energy absorption capability of the sandwich structure is seen, as evident in Figure 4.62.

Figure 4.55 depicts the corresponding energy-time traces at varying impact energies for the linear PVC (R63.140) sandwich structures subjected to normal impact. At energies up to 15 J, a small amount of energy is present in the form of a rebound. With increasing impact energy, i.e. at 20 J, where plastic deformation occurs, an increase in the absorbed energy is apparent and rebound energy is only marginal.

Typical load-displacement traces following a 10° impact on the linear PVC (R63.140) sandwich structures are given in Figure 4.56 and Figure 4.57. At relatively low energies, i.e. 5 J, similar trends to those observed in the normal impact cases are apparent. In addition, an increase in the residual displacement in passing from 0° to 10° is observed. The residual displacement following a normal impact is approximately 2.2 mm whereas the value for the 10° impact case is approximately 2.4 mm, with a difference of about 8.3%. The material response at this point is classified as elastic with no severe damage, with relatively smooth loading and unloading curve, suggesting the presence of rebound energy is apparent at this point.

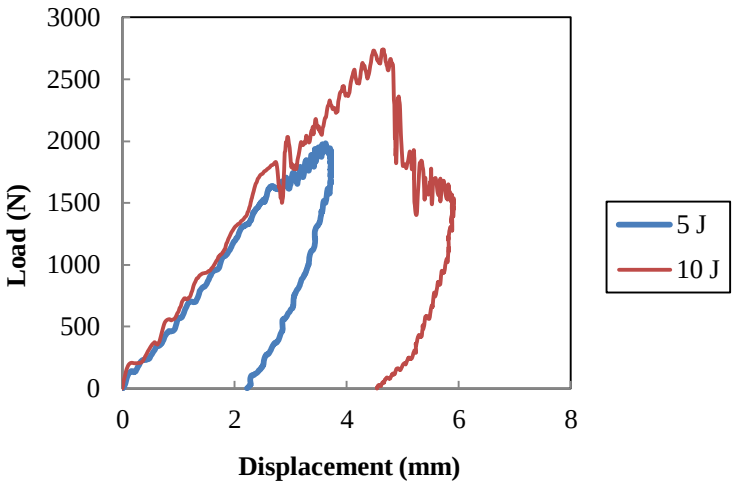

Figure 4.56 Load-displacement traces for the linear PVC (R63.140) sandwich panel following a 10° impact at 5 J and 10 J.

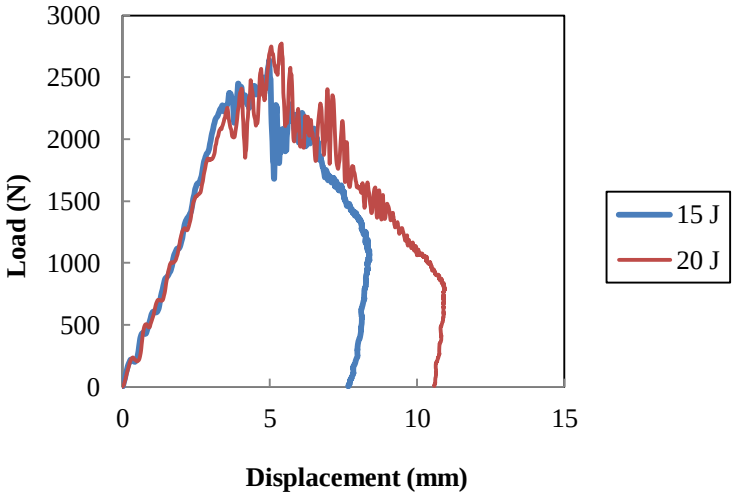

Figure 4.57 Load-displacement traces for the linear PVC (R63.140) sandwich panel following a 10° impact at 15 J and 20 J.

With increasing impact energy, at 10 J, there is a much higher force value in comparison to that of the impact at 5 J, with an increase in the residual displacement to approximately 3.61 mm. In addition, a larger area of load-displacement traces suggests an increase in the energy absorbed, as evident in the corresponding energy-time traces in Figure 4.58 and the plot of absorbed energy vs. impact energy in Figure 4.62.

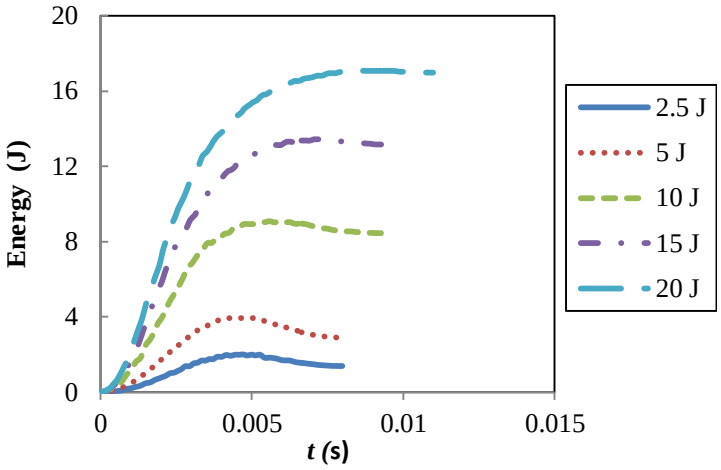

Figure 4.58 Typical energy-time traces for the linear PVC (R63.140) sandwich structures following a 10° impact.

At higher energy, as given in Figure 4.57, i.e. at 20 J, significant load drop is apparent, which is an indication of severe damage in the sandwich structure. The residual displacement at this energy level is 10.59 mm. Again, from the area under the load-displacement traces, it is anticipated that an increase in absorbed energy may be possible, as evident in the plot of absorbed energy vs. impact energy in Figure 4.62.

Figure 4.58 depicts the corresponding energy-time traces at varying impact energies for the linear PVC (R63.140) sandwich structures subjected to a 10° impact. At energies up to 20 J, a similar trend to that observed in the normal impact cases is observed, in which less than fifty percent of the imparted energy is being absorbed by the target. This is associated with rebounding of the indenter following a linear elastic response. At increasing energy, i.e. at 20 J, where plastic deformation occurs, an increase in the absorbed energy is apparent; this is approximately sixty percent of the imparted energy; hence, there is a reduction in amount of energy associated with a rebound.

The load-displacement traces following a 20° impact on the linear PVC (R63.140) sandwich structures at selected energies are presented in Figure 4.59 and Figure 4.60. Similar trends are seen to those observed in the lower-density sandwich structures. At relatively low energy, i.e. ≤ 10 J, the load-displacement traces show a non-linearity in the load-displacement traces, with a small load drop prior to the first peak force. As an example, at 10 J, the residual displacement is approximately 7.9 mm, in comparison to 9.8 mm for the linear PVC (R63.80) sandwich structures.

At a higher energy level, i.e. 20 J, with the start of a large load drop in the load-displacement traces, which indicates permanent deformation in the structure, the residual displacement increased to a maximum of 18.0 mm.

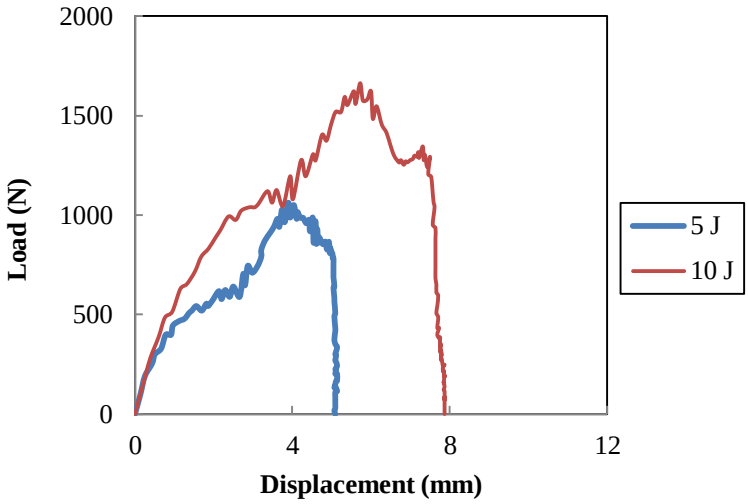

Figure 4.59 Load-displacement traces for the linear PVC (R63.140) sandwich panel following a 20° impact at 5 J and 10 J.

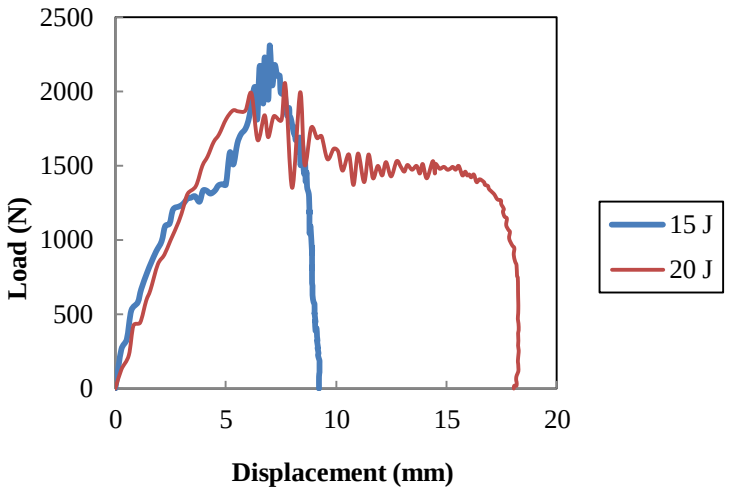

Figure 4.60 Load-displacement traces for the linear PVC (R63.140) sandwich panel following a 20° impact at 15 J and 20 J.

The corresponding energy-time traces following a 20° impact at energies up to 20 J are given in Figure 4.61. From the results, regardless of whether the test was conducted at low or high energy level, the absorbed energy is greater than the rebound energy, which is more than fifty percent of the imparted energy.

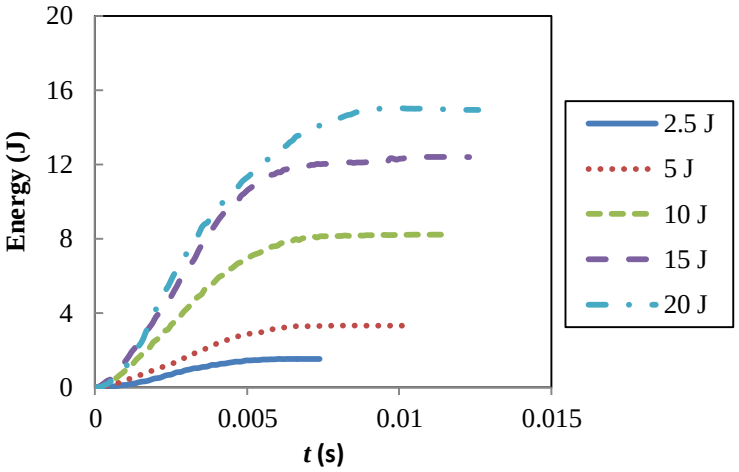

Figure 4.61 Energy-time traces for the linear PVC (R63.140) sandwich structures following a 20° impact.

Again, this is possibly due to the effect of geometry, with more kinetic energy transferred to the indenter at this high inclination angle; therefore, an increase in absorbed energy is expected.

The effect of obliquity on the energy absorption is shown in the linear PVC (R63.140) sandwich structures, in Figure 4.62. In general, there is an increase in the absorbed energy with increasing impact energy, for all the impact cases. However, in contrast to the trend observed in the monolithic laminate and the lower-density linear PVC (R63.80) sandwich structures, clearly the energy absorbed is highest following normal impact, while the 10° impact exhibits energy absorption characteristics that are close to those of the normal impact cases at increasing energies. As an example, at the highest impact energy of 20 J, the absorbed energy is 16.7 J, 16.0 J and 12.4 J following 0°, 10° and 20° impact.

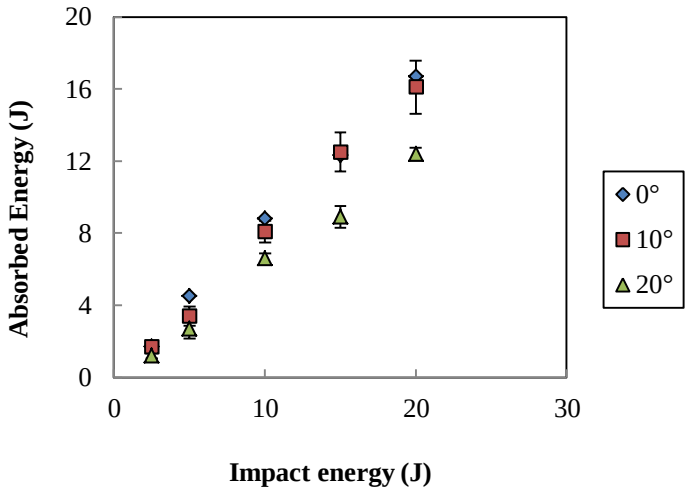

Figure 4.62 Absorbed energy against inclination angle following normal and oblique impact on the linear PVC (R63.140) sandwich structures.

The maximum impact force, P_{max}, and the corresponding maximum normal force, F_N, are plotted against impact energy in Figure 4.63 and Figure 4.64 respectively. In

general, it is apparent that a normal impact results in the highest maximum impact force, which increased with impact energy up to approximately 15 J. Above this threshold energy, there is a decrease in the maximum impact force for the case of normal impact loading. The 10° impact exhibited an increase in the maximum impact force with impact energy up to 10 J, beyond which the maximum impact force decreased. The 20° impact showed similar trends with the threshold energy occurring at approximately 15 J.

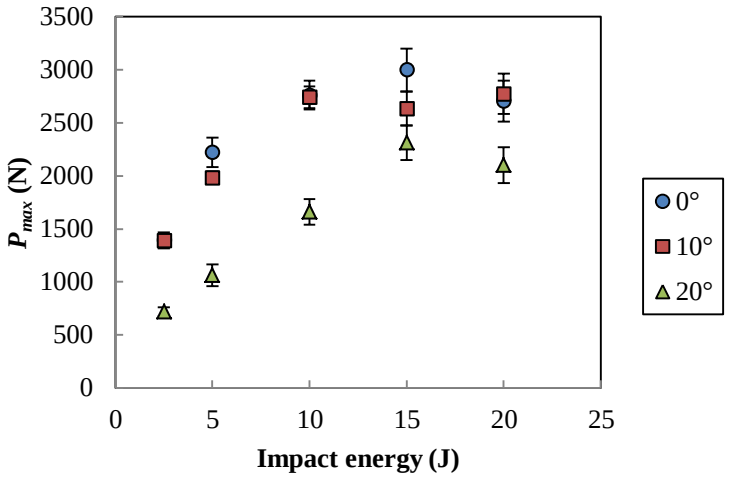

Figure 4.63 Maximum impact force against impact energy for the linear PVC R63.140 sandwich panels subjected to normal and oblique impact.

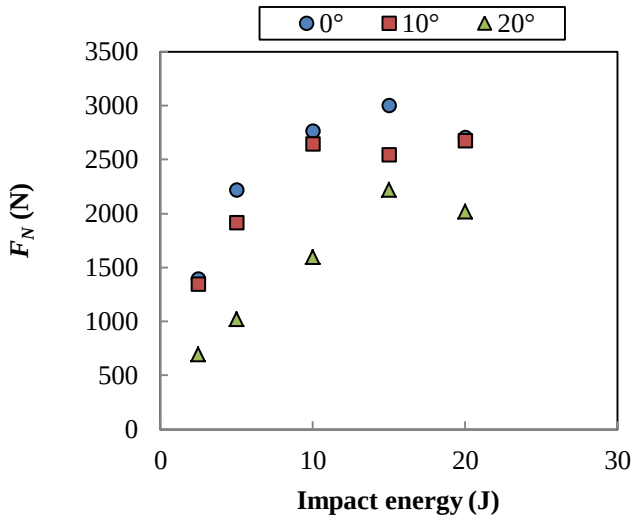

Figure 4.64 Calculated maximum normal forces, F_N, for the linear PVC R63.140 sandwich panels subjected to normal and oblique impact.

In addition, at any given energy level, P_{max} is much higher compared to that of the linear PVC (R63.80) sandwich structures, regardless of whether the test was conducted at normal or other inclination angles. The lists of results are given in Table 4.3 and Table 4.7 following impact on the linear PVC (R63.80) sandwich structures and the linear PVC (R63.140) sandwich structures, respectively.

Table 4.7 Experimental results following a series of normal and oblique impact tests on the linear PVC R63.140 sandwich structures at normal and oblique angles.

Impact angle (°)	**Impact energy (J)**	P_{max} **(N)**	F_N **(N)**	**Damage area (mm^2)**	**Absorbed energy (J)**
0	2.5	1394 ± 75	1394	60 ± 1	1.7 ± 0.2
	5	2220 ± 138	2220	144 ± 1	4.5 ± 1.0
	10	2762 ± 135	2762	314 ± 1	8.8 ± 1.0
	15	2998 ± 201	2998	348 ± 4	12.3 ± 0.9
	20	2705 ± 195	2705	420 ± 2	16.7 ± 0.1
10	2.5	1391 ± 46	1342	84 ± 4	1.7 ± 0.3
	5	1983 ± 59	1912	172 ± 2	3.4 ± 0.5
	10	2742 ± 101	2644	280 ±	8.1 ± 0.6
	15	2635 ± 159	2541	432 ± 3	12.5 ± 1.1
	20	2774 ± 189	2675	496 ± 6	16.1 ± 1.5
20	2.5	719 ± 43	690	80 ± 3	1.2 ± 0.1
	5	1062 ± 101	1019	92 ± 1	2.7 ± 0.5
	10	1662 ± 121	1595	260 ± 2	6.6 ± 0.3
	15	2312 ± 162	2218	326 ± 3	8.9 ± 0.6
	20	2100 ± 168	2015	340 ± 3	12.4 ± 0.4

From the plot of the calculated maximum normal force, F_N, against impact energy, as observed with other types of composite structures tested under similar inclination angles, it is the normal impact that exhibits the highest value of the maximum normal force, which is in agreement with the previous work by Madjidi *et al*. [1].

Figure 4.65 depicts the measured damaged area vs. impact energy following normal and oblique impact on the linear PVC (R63.140) sandwich structures. For the normal impact case, in general, damage area increases almost linearly with impact energy, at

energies up to approximately 10 J. Beyond this point, the values show a plateau up to the maximum energy of 20 J. Overall, the maximum damage area is smaller than that of the 10° impact case.

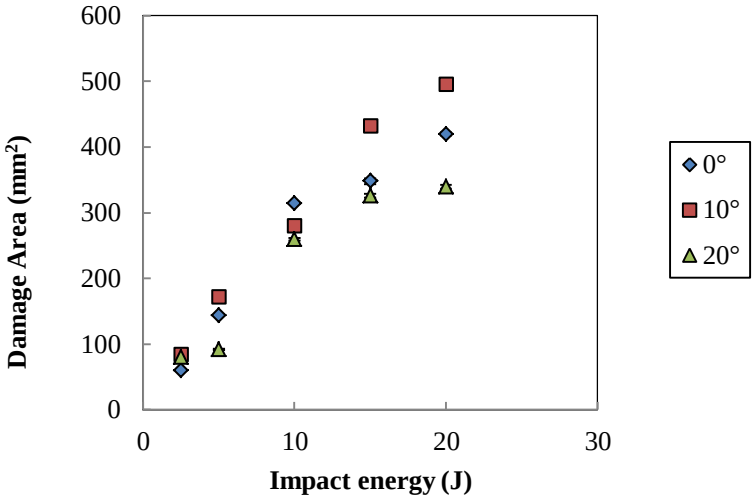

Figure 4.65 Damage area against impact energy following normal impact on the linear PVC (R63.140) sandwich structures.

For impact at 10°, the damage area increases linearly with increasing impact energy, at energies up to 20 J. However, from the plot, it is apparent that the damage area is larger than that of the normal impact case at energies greater than 10 J. This observation is possibly due to greater combined effects of tension-compression and shear stresses in the sandwich structures at the higher impact energies.

For the 20° impact, at low energy levels, i.e. up to 15 J, there is a linear increase in the measured damage area with increasing impact energy. Beyond this, the value plateaus at approximately 20 J.

Figure 4.66 shows a plot of the maximum permanent indentation as a function of impact energy for the linear PVC (R63.140) sandwich structures subjected to normal and oblique impact. It appears that for the normal impact, maximum permanent

indentation increases linearly, particularly for the 0° and 10° impact cases, with impact energy up to 20 J. The measured maximum depth of permanent indentation following a 20 J impact is 4.16 mm, showing a marginal increase of 4.8%, in comparison to that of the linear PVC (R63.80) sandwich structures, with the value of 3.96 mm.

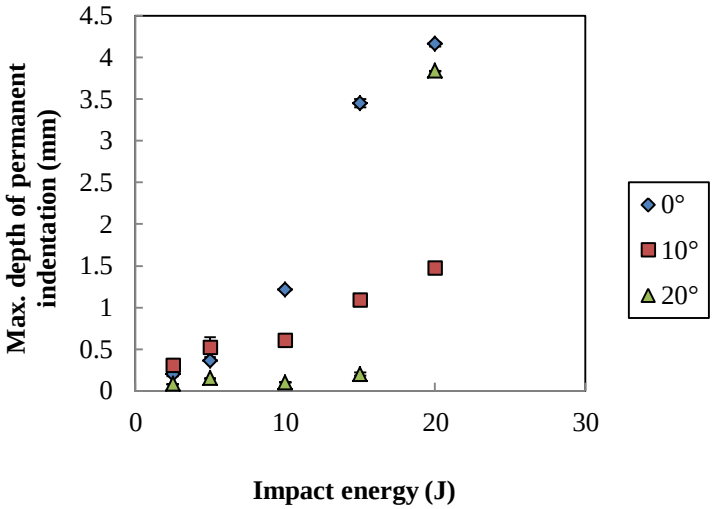

Figure 4.66 Max. depth of permanent indentation vs. impact energy following normal and oblique impact on the linear PVC (R63.140) sandwich structure.

Similar trends to the 0° impact are observed in the plot for the 10° impact, at energies up to 20 J, with the maximum depth of the permanent indentation being approximately 3.47 mm. Again, a slight increase is found when compared with that of the linear PVC (R63.80) sandwich structures, with the measured depth of 3.40 mm).

For the 20° impact case, at energies up to 15 J, there is only marginal depth of the permanent indentation depth measured. However, at higher energy, i.e. 20 J, this value increased dramatically, possibly due to the propagation and progression of permanent deformation in the sandwich structures. The maximum depth of

permanent indentation for this sandwich structure at the energy level is 3.84 mm, which is almost seven times greater than that of the lower-density linear PVC (R63.80) sandwich structures.

Again, these observations are expected since, damage in sandwich structures depends on the shear stiffness of the core, which is a dominant factor in the transfer of stress from top skin to the core, to the lower skin [13].

Photographs showing the impact surfaces of the linear PVC (R63.140) sandwich structure subjected to 20 J are given in Figure 4.67. It is apparent that both normal and 10° impact resulted in a "peanut-like" shape of the damage, with some degree of penetration of the top skin. Here, the measured maximum depth of the permanent indentations (from the top surface) is approximately 4.2 mm and 3.5 mm for the 0° and 10° impact respectively. In addition, the sandwich structure subjected to a 20° impact also exhibited some degree of penetration, with the maximum depth of permanent indentation being close to 3.8 mm. In terms of the pattern or shape of the damage zone, the 0° and 10° panels are similar to those of the lower-density linear PVC (R63.80) sandwich structures. In addition, the 20° case exhibits a damage pattern that is more elliptical, relative to those of the other impact cases. These cases could possibly be due to an elliptical contact surface between the indenter and the target (panel) particularly at 20°, as highlighted in earlier work on oblique impact [7]; however evidence of indenter penetration on the top skin is apparent for this case.

(a) Typical "peanut-like" shaped delaminated area on the impact surface of a linear PVC (R63.140) sandwich structure following a normal impact at 20 J, showing evidence of permanent indentation or penetration of the indenter into the top skin. The measured depth of permanent indentation is approximately 4.2 mm.

(a) Typical "peanut-like" shaped delaminated area on the impact surface of a linear PVC (R63.140) sandwich structure following a normal impact at 20 J, showing evidence of permanent indentation or penetration of the indenter into the top skin. The measured depth of permanent indentation is approximately 4.2 mm.

(c) An elliptical delaminated area showing penetration of the indenter on the top skin of a linear PVC (R63.140) sandwich structures following a 20 J impact at 20°, with measured depth of permanent indentation of approximately 3.84 mm.

Figure 4.67 Photographs showing the top skin of the linear PVC (R63.140) sandwich structures following a 20 J impact at (a) 0° ; (b) 10° ; (c) 20° inclination angles.

Figure 4.68 shows cross-sections of the linear PVC (R63.140) sandwich structures following a 20-J impact at 0°, 10° and 20° of inclination. In general, a similar trend was observed to that of the lower density linear PVC (R63.80) sandwich structures, where damage area reduces with increasing inclination angle. The failure behaviour is in the form of debonding of the skin-core interface, leading to matrix cracking and fibre fracture (top skin), as well as core shear rupture.

(a) Normal Impact

(b) 10° impact

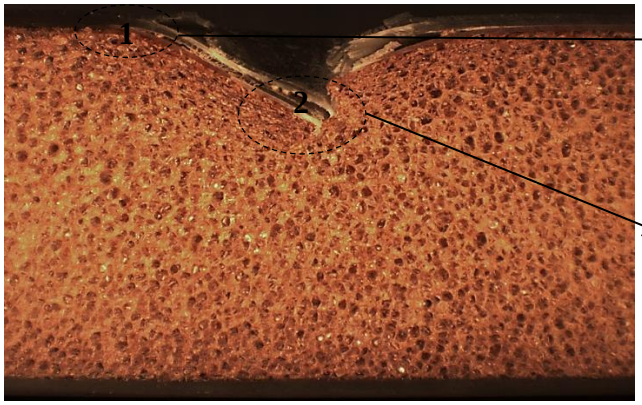

(c) 20° impact

Figure 4.68 Optical micrographs showing failure in the linear PVC (R63.140) sandwich structures following (a) normal impact; (b) 10° impact and (c) 20° impact (20 J).

Apart from the inclination angle, the core density contributes to the damage behaviour of these structures. This is clearly seen in the optical micrograph of the higher density linear PVC (R63.140) sandwich structure following normal impact, as given in Figure 4.68 (a). Here, with higher core density, the panel exhibits more prominent damage area, with greater depth of permanent indentation, localised to the point of impact. These observations confirm that higher core density causes higher contact stiffness that leads to higher force magnitude.

At 10°, as given in Figure 4.68 (b), while the damage area is comparable to that of the lower density sandwich panel as in Figure 4.46 (b), damage is more localized, with a much greater depth of permanent indentation as well as larger core shear rupture. At an inclination angle of 20°, significant damage is observed in the panel with a higher density core, further confirming the influence of the core density on the failure behaviour of these structures, as evident in Figure 4.68 (c).

4.2.2.3 Comparison of experimental and theoretical results

As shown in Figure 4.69, the predicted values of P_{max} are compared with the experimental results, plotted against impact energy. In general, the predicted values agree well with the experimental results, particularly up to the onset of damage, i.e. at 10 J. Up to this energy level, the maximum difference between the predicted values and the experimental values is approximately 10%, for the three inclination angles.

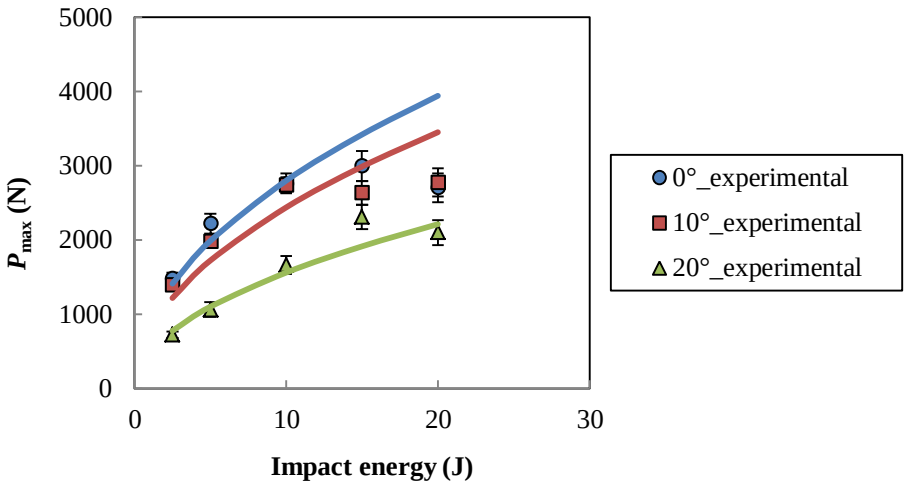

Figure 4.69 Experimental and predicted maximum impact force (solid lines) for the linear PVC R63.140 sandwich plates subjected to normal and oblique impact.

At much higher energy levels, i.e. 20 J, the energy-balance model tends to over-predict P_{max}, especially for the 0° and 10° impact cases, with a maximum difference of approximately 46% and 24% for each case respectively. However, at a higher inclination angle of 20°, this value is over-predicted by only about 5%. Overall, again, the energy balance model is able to accurately predict well the impact response for these types of composite structures, particularly at low energy levels.

4.2.3 Normal and oblique impact tests on PET (T92.100) sandwich plates

In this section, the results following normal and oblique impact on the PET sandwich structures with a nominal density of 105 kg/m^3 (T92.100) are discussed using a similar approach as in Sections 4.2.1 and 4.2.2 (linear PVC sandwich structures), at energies of up to 20 J.

4.2.3.1 Theoretical predictions for impact response of the PET (T92.100) sandwich structures at normal and oblique angles using the energy-balance model

4.2.3.1.1 Determination of contact parameters

In this section, a similar approach to those of the linear PVC sandwich structures is adopted in quantifying the contact parameters from a series of experimental tests.

Typical load-indentation traces following static indentation tests on the PET (T92.100) sandwich structures are given in Figure 4.70. Here, it is evident that the plot following a normal inclination angle exhibits the highest slope of the load-indentation, which suggests higher contact stiffness, in comparison to the non-normal cases. As expected, at the highest inclination of 20°, the load-indentation response exhibits greater indentation, i.e. close to 0.03 m, with the steepest slope.

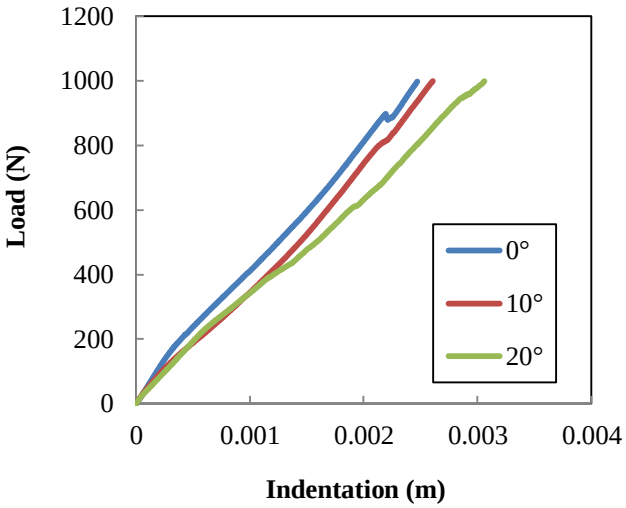

Figure 4.70 Typical load-indentation traces following static indentation test on the PET (T92.100) sandwich structures at 0°,10° and 20° inclination angles.

The average values of the contact stiffness, *C*, and indentation exponent, *n*, following a series of quasi-static indentation tests on the PET (T92.100) sandwich structures are shown in Figure 4.71 and Figure 4.72.

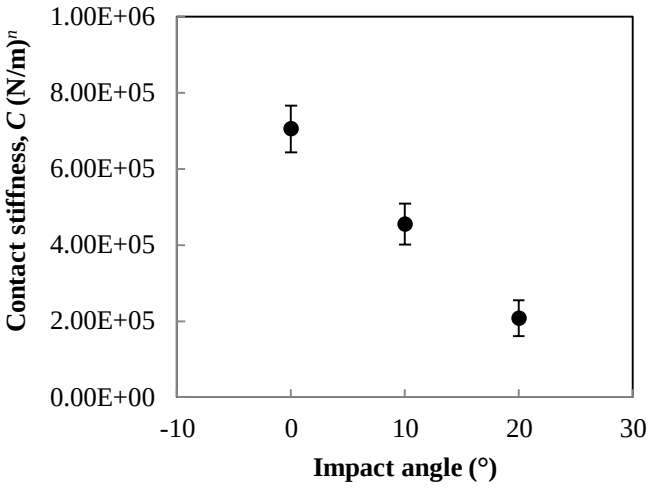

Figure 4.71 Average values of contact stiffness, *C*, for the PET (T92.100) sandwich panels during static indentation loading at increasing inclination angles.

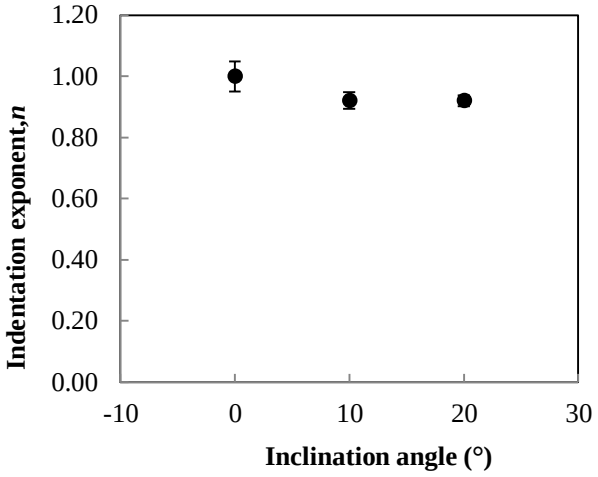

Figure 4.72 Average value of indentation exponent, '*n*', for the PET (T92.100) sandwich panels during static indentation loading at increasing inclination angles.

Similar observations are noted for these sandwich structures, whereby it is apparent that the contact stiffness is highest for the 0° inclination angle and the value is reduced passing from 0° to 20°. However, the indentation exponent for the three cases does not differ significantly with increase in inclination angle. The values are listed in Table 4.8 and Table 4.9.

Table 4.8 Contact stiffness, *C*, of the PET sandwich structures following static indentation tests.

Material system	**Nominal density (kg/m^3)**	**Contact stiffness, *C* (x10^5) (N/m)^n**
PET (T92.130)	135	0°: 8.05 ± 0.02 10°: 7.88 ± 0.03 20°: 4.45 ± 0.04
PET (T92.100)	115	0° : 7.05 ± 0.06 10°: 4.55 ± 0.05 20° : 2.07 ± 0.05

Table 4.9 Indentation exponent, *n*, of the PET sandwich structures following static indentation tests.

Material system	**Nominal density (kg/m^3)**	**Indentation exponent, *n*,**
PET (T92.130)	135	0°: 1.04 ± 0.05 10°: 0.92 ± 0.03 20°: 0.82 ± 0.02
PET (T92.100)	115	0° : 1.00 ± 0.05 10°: 0.92 ± 0.03 20° : 0.92 ± 0.02

4.2.3.2 Experimental results following normal and oblique impact tests on PET (T92.100) sandwich plates.

Unlike the linear PVC foam, which is well known to exhibit ductile behaviour, the PET foam core is a rigid polymeric material; therefore such material is expected to show more brittle-like failure when subjected to impact loading, particularly at higher energies. Hence, for the PET (T92) sandwich structures, similar observations may be sought when subjected to quasi-static and/or dynamic loading via drop weight impact test. Limited papers have discussed the experimental as well as

numerical findings on the PET-based sandwich structures subjected to normal [15] and oblique impact response [16].

Two sections in this chapter are dedicated to studying the normal and oblique impact response of the PET sandwich structures in the low velocity impact range.

In this section, impacts up to 20 J are presented and discussed, using a similar approach to that employed for the linear PVC sandwich structures, highlighting the main results and discussions, in terms of the load-time, P_{max} vs. impact energy, F_N vs impact energy, damage area vs. impact energy, max. depth of permanent indentation as well as the absorbed energy vs. impact energy.

However, investigations of the failure at the cross-sections are not included in this section. In addition, an extension of this work is presented in the later section (Section 4.3), where perforation behaviour of these sandwich structures is further investigated at much higher energies, of up to 40 J.

The main results following normal and oblique impact at energies up to 20 J on the high-density PET (T92.100) sandwich structures are listed in Table 4.10.

Table 4.10 Experimental results following a series of normal and oblique impact tests on the PET (T92.100) sandwich structures.

Impact angle (°)	Impact energy (J)	P_{max} (N)	F_N (N)	Damage area (mm^2)	Absorbed Energy (J)
0	2.5	1328 ± 60	1328	53 ± 2	1.6 ± 0.1
	5	1987 ± 139	1987	260 ± 4	1.8 ± 0.1
	10	2414 ± 164	2414	317 ± 1	3.9 ± 0.0
	15	2424 ± 175	2424	416 ± 3	7.0 ± 0.4
	20	2462 ± 187	2462	327 ± 3	15.9 ± 0.1
10	2.5	1299 ± 23	1253	33 ± 1	1.3 ± 0.1
	5	1629 ± 49	1571	182 ± 5	3.7 ± 0.1
	10	2084 ± 92	2010	191 ± 3	8.7 ± 0.1
	15	2210 ± 180	2131	408 ± 2	10.3 ± 0.8
	20	2908 ± 194	2805	348 ± 1	13.0 ± 0.0
20	2.5	698 ± 68	670	30 ± 3	1.1 ± 0.4
	5	1212 ± 148	1163	182 ± 3	3.5 ± 0.3
	10	1571 ± 201	1507	102 ± 2	5.1 ± 0.1
	15	1794 ± 227	1721	307 ± 1	6.8 ± 0.0
	20	2249 ± 224	2158	301 ± 2	13.3 ± 0.1

Examples of typical load-time traces for impact at 10 and 20 J are presented in Figures 4.73 and Figure 4.74. In Figure 4.73, both the normal and 10° impact traces exhibit sudden (large) load drops, whilst the 20° impact case showed a relatively small reduction in load. With increasing impact energy (20 J), as given in Figure 4.74, it is apparent that all of the panels undergo large load drop and longer total contact time , which is close to 3 ms.

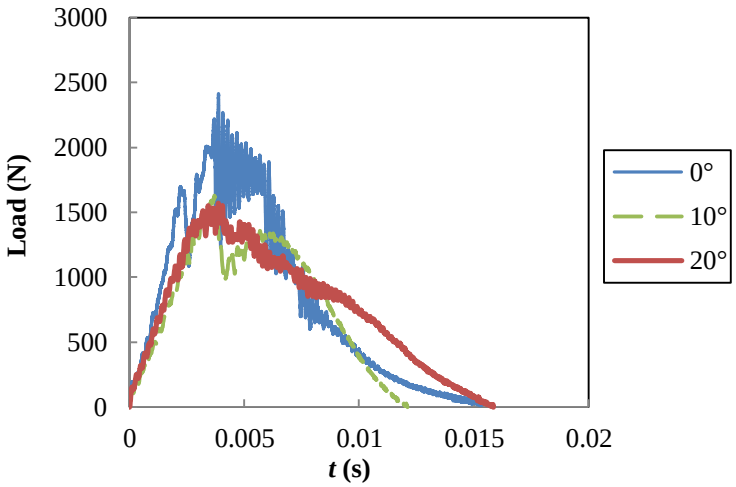

Figure 4.73 Load-time traces for the PET (T92.100) sandwich panels subjected to normal and oblique impact at 10 J.

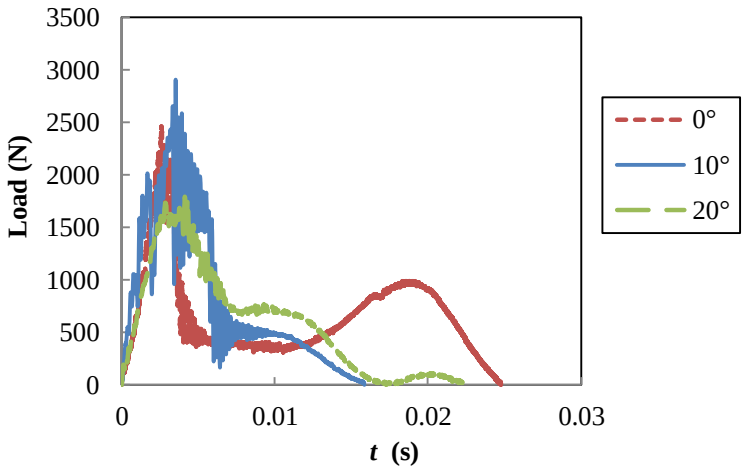

Figure 4.74 Load-time traces for the PET (T92.100) sandwich panels subjected to normal and oblique impact at 20 J.

Figure 4.75 presents P_{max} plotted against impact energy for the response at normal and oblique angles. In general, the values following normal impact (θ: 0°) increase with energy up to 10 J. Beyond this energy level, there is a decrease in the maximum impact force. In Figure 4.76, it is apparent that for both the 10° and 20° impact cases, the maximum normal force increases with impact energy up to approximately 20 J. Again, as with other types of composite structure, normal impact resulted in the highest maximum normal force.

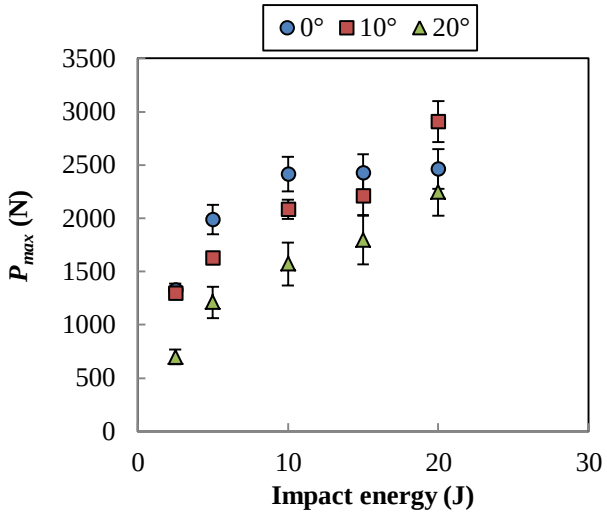

Figure 4.75 Maximum impact force against impact energy for the PET (T92.100) sandwich panels subjected to normal and oblique impact.

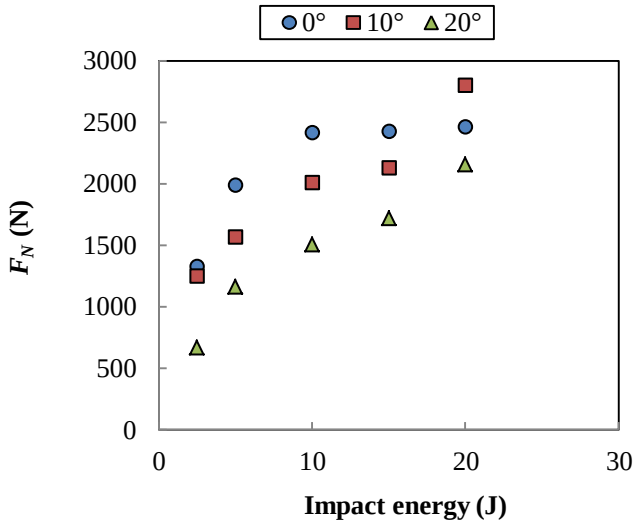

Figure 4.76 Calculated maximum normal force, F_N, against impact energy for the PET (T92.100) sandwich panels subjected to normal and oblique impact.

The variation of damage area with impact energy for the three impact angles is presented in Figure 4.77. For all the impact cases, there is an increase in damage area up to approximately 15 J, with the largest damage areas being approximately 416 mm^2, 408 mm^2 and 307 mm^2 following impact at 0°, 10° and 20° respectively.

Beyond this energy level, the value is reduced at energies up to 20 J, for all the impact cases. This trend is different compared to that in the linear PVC sandwich

structures, where damage area increased with impact energy up to 20 J, regardless of whether the test was conducted at normal or oblique angles. This could be due to more concentrated force acting on the contact surface of the PET foam based sandwich structures, causing some degree of indentation of the indenter, rather than spreading the damage in the form of delamination on the top skin, as observed in the linear PVC sandwich structures.

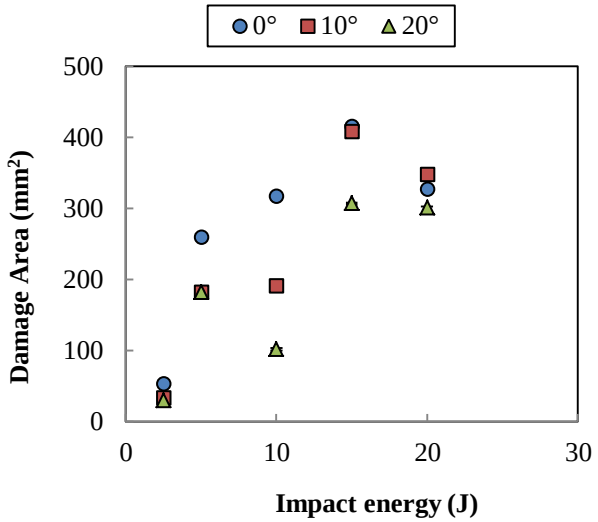

Figure 4.77 Damage area against impact energy for the PET (T92.100) sandwich panels subjected to normal and oblique impact.

These observations have been quantified and are apparent from the results of the measured depth of maximum permanent indentation in the sandwich panels subjected to normal and oblique impact at energies up to 20 J are given in Figure 4.78. In general, both the 0° and 20° impact show similar trend, with the maximum depth of permanent indentation increases with impact energy up to 15 J, with the largest depth of permanent indentation of 5.61 mm and 2.62 mm for the 0° and the 20° case, respectively. This is corresponding to the trend in the damage area. Beyond this, the value decreases at the maximum impact energy of 20 J. As for the

10° impact, there is a linear increase in the plot of the maximum depth of permanent indentation, reaching a maximum at 20 J with the value of approximately 4.18 mm.

The energy absorption behaviour of the PET (T92.100) sandwich panels is shown in Figure 4.79, showing the values for impact at normal, 10° and 20°. Here, the energy absorption characteristics do not show a clear trend with inclination angle, particularly at lower impact energies (up to approximately 5 J).

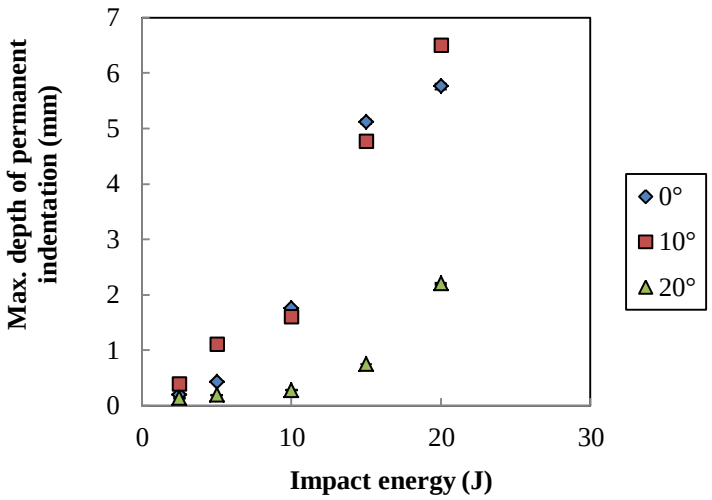

Figure 4.78 Maximum depth of permanent indentation following normal and oblique impact on the PET (T92.100) sandwich structures.

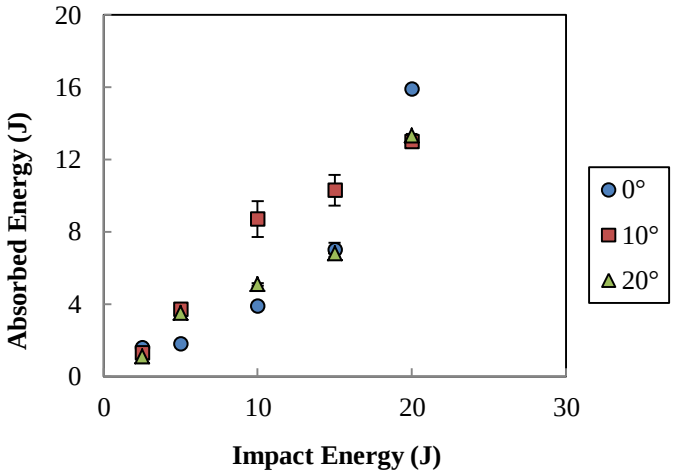

Figure 4.79 The energy absorbed vs. impact energy for the PET (T92.100) sandwich panels subjected to normal and oblique impact.

At higher energies, where partial perforation occurs in the sandwich panel subjected to normal impact, it is apparent that the corresponding energy absorption for the normal impact is highest.

Here, the energy absorption characteristics do not show a clear trend with inclination angle, particularly at lower impact energies (up to approximately 5 J). At higher energies, where partial perforation occurs in the sandwich panel subjected to normal impact, it is apparent that the corresponding energy absorption for the normal impact is highest.

4.2.3.2.1 Comparison of experimental and theoretical results

The experimental and predicted values following normal and oblique impact on the T92.100 sandwich structures are shown in Figure 4.80. Similar trends to those observed in the results for the linear PVC sandwich structures are apparent, in which the experimental and predicted values show good agreement at energies up to about 10 J, particularly for the 0° and 10° impact cases.

Beyond this energy level, the model tends to over-predict the maximum impact force, i.e. at 0° impact, the value is over-predicted by approximately 30% at higher impact energies, whereas the 10° impact showed an over-prediction more than 20% relative to the experimental results. For the 20° impact case, the experimental and predicted values shows good agreement, with the average difference being approximately 10%.

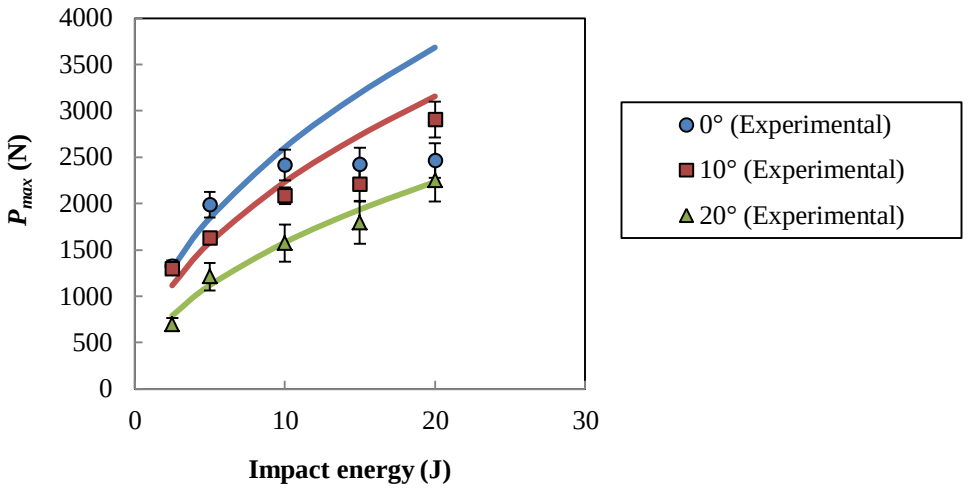

Figure 4.80 Experimental and predicted maximum impact force (solid line) for the PET (T92.100) sandwich plates subjected to normal and oblique impact.

4.2.4 Normal and oblique impact tests on PET (T92.130) sandwich plates

In this section, the results obtained from a series of experimental tests on the higher density (nominal density = 135 kg/m^3) PET-based sandwich structures are presented and discussed relative to the other types of composite structure. A similar approach to that of the lower density PET (T92.100) sandwich structures are employed in discussing the findings.

4.2.4.1 Theoretical predictions for the impact response of the PET (T92.130) sandwich structures at normal and oblique angles using the energy-balance model

4.2.4.1.1 Determination of the contact parameters

Typical load-indentation curves obtained from a series of quasi-static indentation tests on the PET (T92.130) sandwich structures are presented in Figure 4.81. Clearly, the response at the normal inclination angle possess exhibits the highest stiffness, from the slope of the load-indentation traces; whereas the response at the highest inclination angle, of 20° exhibits the lowest stiffness.

From Figure 4.81, the contact parameters were obtained using the same approach as adopted in previous section in this chapter, as given in Figure 4.82, showing the plot of the average values of the contact stiffness as a function of inclination angle, *C*, and the indentation exponent, *n*, as a function of inclination angle, as shown in Figure 4.83. These values are also listed in Table 4.8 and Table 4.9 respectively.

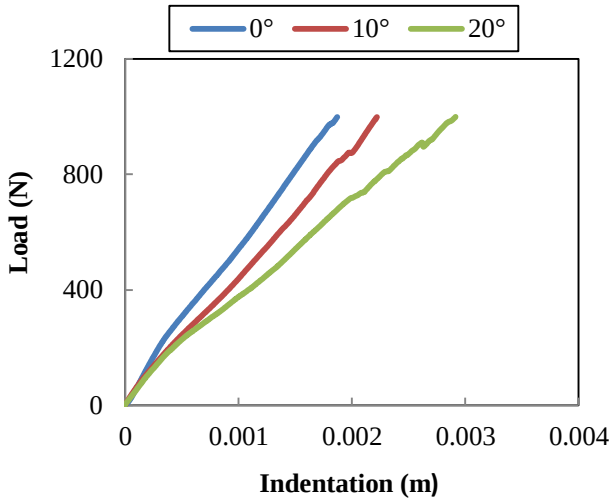

Figure 4.81 Typical load-indentation traces for the PET (T92.130) sandwich foam panels during static indentation testing at a crosshead displacement rate of 1 mm/min and at normal, 10° and 20° inclination angles.

Referring to Figure 4.82, it is evident that the contact stiffness, *C*, values of the PET (T92.130) are much higher, in comparison to the lower density foam-based sandwich structures. These findings are similar to the linear PVC sandwich structures, highlighting the effect of core density on the contact properties of a sandwich structures. In addition, the contact stiffness, *C*, also decreases with increase in inclination angle, showing the effect of obliquity on the parameter.

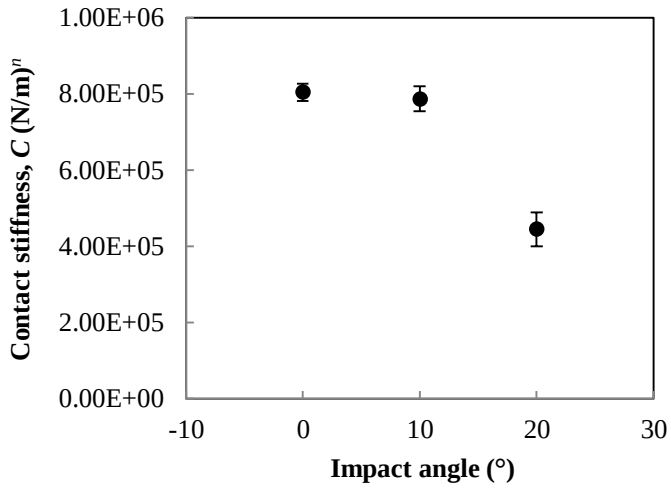

Figure 4.82 Average values of contact stiffness, *C*, for the PET (T92.130) sandwich panels during static indentation loading at increasing inclination angles.

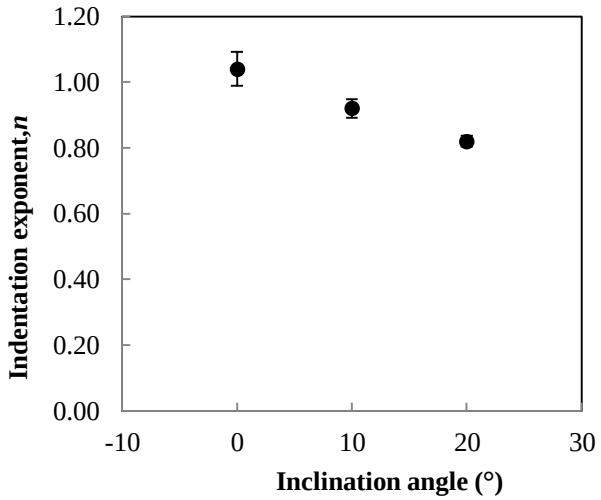

Figure 4.83 Average value of indentation exponent, '*n*', for the PET (T92.130) sandwich panels during static indentation loading at increasing inclination angles.

In terms of the indentation exponent, *n*, as given Figure 4.83 and Table 4.9, again, the trend is also similar with other types of composite structures (laminated composites and linear PVC sandwich structures), with the value of *n* decreasing with increasing inclination angle. In addition, the value of *n* is close to 1, suggesting an ideally elastic response of sandwich structures, when loaded up to 1 kN.

However, the effect of core density is not clear when the '*n*' values are compared for the two grades of the PET -based sandwich structure. These observations are similar to those reported by Akil [6] in quantifying the indentation exponent of several types of polymeric foam-based sandwich structures.

4.2.4.2 Experimental results following normal and oblique impact tests on PET (T92.130) sandwich plates.

The main results following normal and oblique impact at energies up to 20 J on the high density PET (T92.130) sandwich structures are listed in Table 4.11. These include the maximum impact force, P_{max}, the corresponding normal force, F_N, damage area and the absorbed energy.

Typical examples of load-time traces following impact at normal and oblique angles are shown in Figure 4.84 and Figure 4.85. At 10 J, as given in Figure 4.84, the load-time traces for the different impact angles are given, with the normal impact generating the highest impact force.

With increasing impact energy, at 20 J, there is a significant load drop observed in the load-time traces, as shown in Figure 4.85. For the 20° impact, from the load-time trace, it can be seen that there is only marginal load drop observed at the various energy level. This suggests an elastic response of the sandwich structures at this energy level, with the panel remaining undamaged.

Table 4.11 Experimental results following a series of normal and oblique impact tests on the PET (T92.130) sandwich structures.

Impact angle (°)	**Impact energy (J)**	P_{max} **(N)**	F_N **(N)**	**Damage area (mm^2)**	**Absorbed energy (J)**
0	2.5	1567 ± 75	1654	65 ± 4	1.6 ± 0.0
	5	1944 ± 156	1958	142 ± 0	2.3 ± 0.0
	10	2714 ± 189	2492	382 ± 7	7.3 ± 0.1
	15	2744 ± 208	2492	578 ± 1	10.9 ± 0.1
	20	2866 ± 263	2597	484 ± 1	18.7 ± 0.2
10	2.5	1576 ± 28	1515	60 ± 1	1.2 ± 0.1
	5	2010 ± 71	1673	132 ± 3	4.4 ± 0.1
	10	2260 ± 100	2352	332 ± 5	8.5 ± 0.0
	15	2247 ± 214	1973	450 ± 3	12.3 ± 0.4
	20	2361 ± 196	2029	603 ± 8	17.2 ± 0.0
20	2.5	756 ± 74	725	56 ± 0	1.2 ± 0.0
	5	1088 ± 133	1044	129 ± 0	4.8 ± 0.0
	10	1516 ± 223	1454	229 ± 0	7.3 ± 0.4
	15	1741 ± 249	1670	198 ± 6	9.8 ± 0.1
	20	1923 ± 246	1845	369 ± 0	14.2 ± 0.3

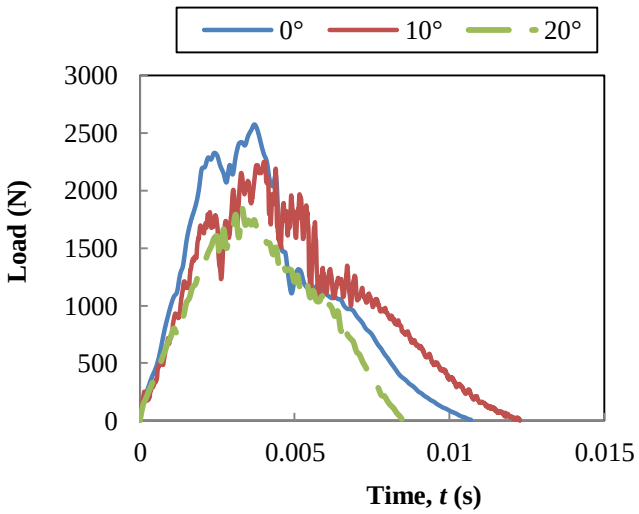

Figure 4.84 Typical load-time traces for the PET (T92.130) subjected to a 10 J impact at normal, 10° and 20° inclination angles.

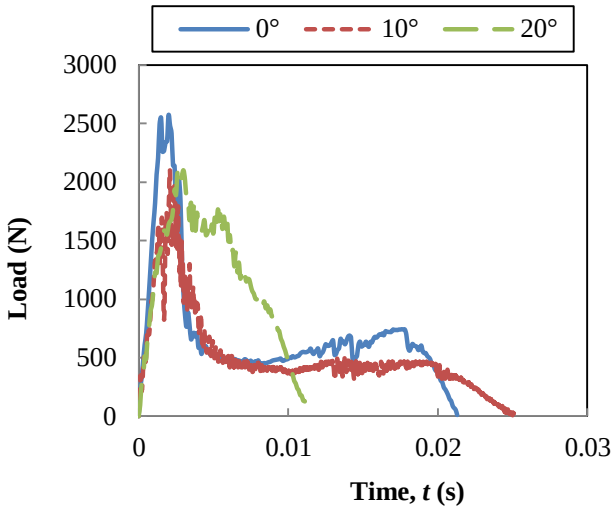

Figure 4.85 Typical load-time traces for the PET (T92.130) subjected to a 20 J impact at normal, 10° and 20° inclination angles.

Figure 4.86 presents the maximum impact force plotted against impact energy for both the normal and oblique impact response of these panels at energies up to 20 J. Overall, both the normal and 10° impact results show a gradual increase in the maximum impact force with impact energy up to threshold energy of approximately 10 J.

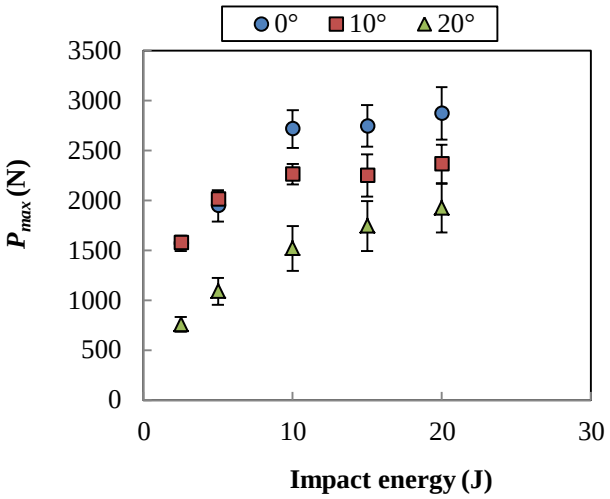

Figure 4.86 Maximum impact force against impact energy for the PET (T92.130) sandwich panels subjected to normal and oblique impact.

Above this threshold, there is a plateau in the P_{max} for both the 0° and 10° impact cases, followed by a small increase at approximately 20 J. Clearly, the 20° impact case shows an increase in the P_{max} values with increasing impact energy, with much lower force values.

The corresponding normal forces F_N, were calculated and the values are presented in Figure 4.87. Here, as with other types of composite structure, it is clear that the 0° impact exhibits the highest normal force, F_N. In addition, the 20° impact again offers the lowest force magnitude in the normal direction.

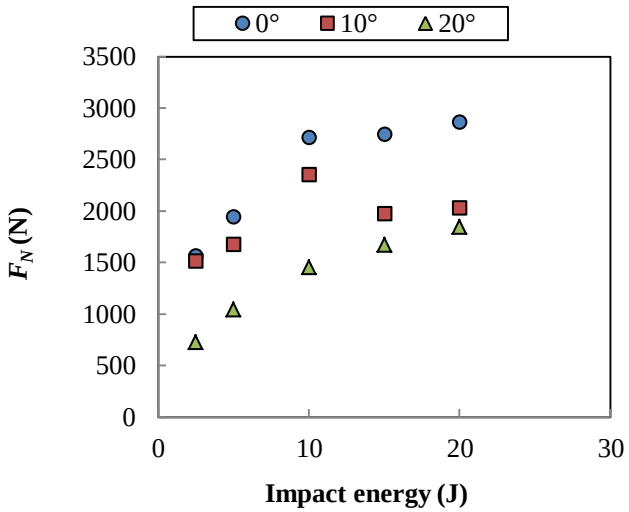

Figure 4.87 Maximum normal force, F_N, against impact energy for the PET (T92.130) sandwich panels subjected to normal and oblique impact.

Figure 4.88 presents variation of damage area with impact energy for panels subjected to normal and oblique impact. Here, similar to the observations on the linear PVC sandwich structures, the sandwich structure subjected to a 10° impact exhibit the greatest level of damage, whereas the 20° impact generated the least amount of damage for energies up to 20 J. Again, these could possibly be due to the combination of tensile, compression and shearing stresses on the sandwich structures

at 10°, in comparison to tensile and compression stresses for the normal impact case or the pure shear for the panel subjected to a 20° impact.

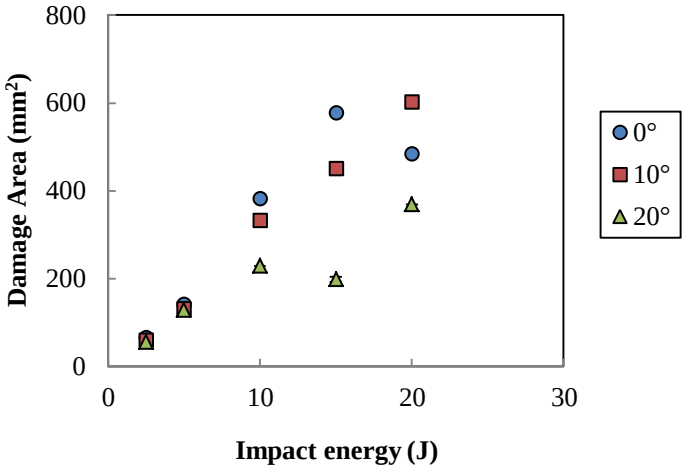

Figure 4.88 Damage area against impact energy for the PET (T92.130) sandwich panels subjected to normal and oblique impact.

These observations have been quantified and are apparent from the results of the measured depth of maximum permanent indentation in the sandwich panels subjected to normal and oblique impact at energies up to 20 J as given in Figure 4.89. In general, both the 0° and the 10° impact cases exhibit similar trends, showing a linear increase in the measured maximum depth of permanent indentation, up to a maximum of 20 J. In addition, the maximum depth of permanent indentation is largest for the 10° case, with the measured depth of approximately 6.5 mm, with the value of approximately 6.50 mm, in comparison to a maximum depth of 5.76 mm for the normal impact case. As with other types of composite structures, the 20° impact exhibit much smaller depth of permanent indentation, with the maximum depth of approximately 2.20 mm.

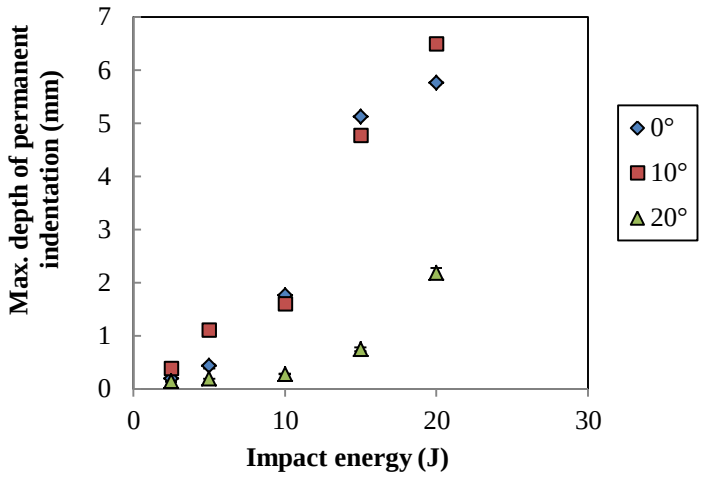

Figure 4.89 Maximum depth of permanent indentation following normal and oblique impact on the PET (T92.130) sandwich structures.

The energy absorbed following normal and oblique impact on the PET (T92.130) sandwich panels is given in Figure 4.90. Here, the effect of obliquity is not clear, whereby, at lower energies (<5 J), there is only a marginal difference between the results from normal and the oblique impact cases.

At intermediate energy levels, i.e. between 10 and 15 J, the 10° impact exhibits much higher energy absorption, relative to the normal impact. Interestingly, at higher energies, i.e. at 20 J, where partial perforation of the hemispherical indenter was observed for all the three impact cases, the effect of obliquity on the energy absorption is not clear.

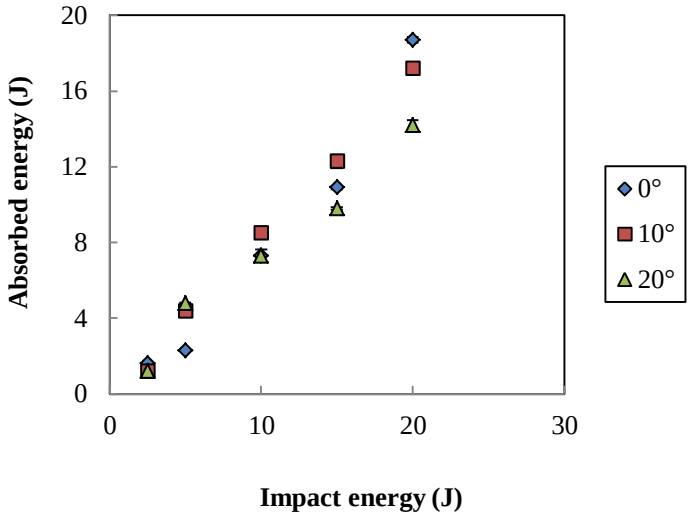

Figure 4.90 Absorbed energy against impact energy for the PET (T92.130) sandwich panels subjected to normal and oblique impact.

In summary, both grades of the PET (T92.100 and T92.130) exhibit similar trends to those observed in the high density linear PVC (R63.140) sandwich structures, in terms of the P_{max}, corresponding F_N, damage area and absorbed energy as a function of impact energy. However, the main difference between the linear PVC and the PET are apparent in the load-time traces, in which greater load drop are observed in the PET sandwich structures, particularly at higher impact energies, i.e. 20 J. These could be attributed to the material's behaviour, which is known to be brittle, therefore undergo more dramatic load drop at high impact loading

4.2.4.2.1 Comparison of experimental and theoretical results

The experimental results are compared with the predictions from an energy-balance model in Figure 4.91, following normal and oblique impact on the T92.130 sandwich structures at energies up to 20 J. Overall, similar observations to those of the lower density PET (T92.100) sandwich structures are observed; where the experimental

values and the predicted values show good agreement up to 10 J (onset of damage for 0° and 10° impact). Beyond this energy level, the model tends to over-predict the maximum impact force. For example, the normal impact results are over-predicted by approximately 25% at 15 J and about 38 % at 20 J, whereas for the 10° impact, the difference between the predicted and the experiments are much higher, being about 60% at higher energy levels. However, better agreement between the experimental data and the predicted values are noted for the 20° impact case, since the sandwich structures do not suffer significant damage and the model assumes elastic response [13].

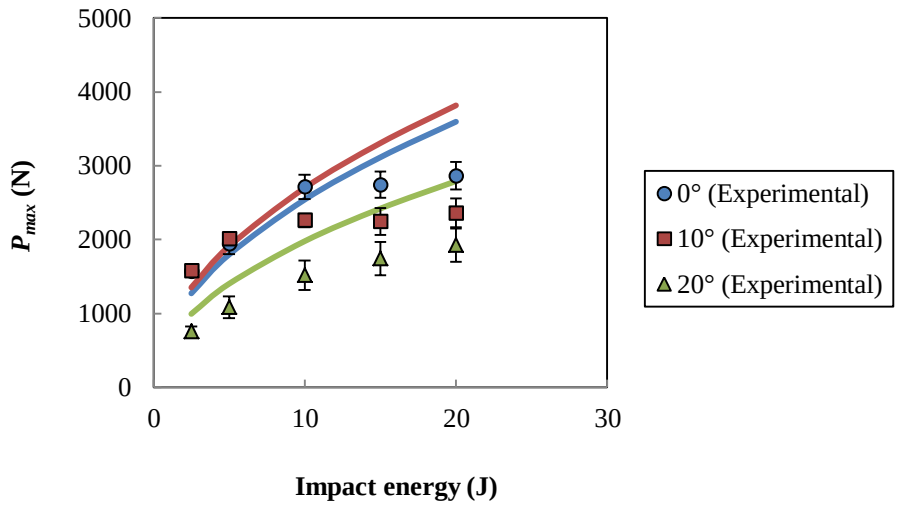

Figure 4.91 Experimental and predicted maximum impact force (solid line) for the PET (T92.130) sandwich plates subjected to normal and oblique impact.

4.3 Perforation behaviour of PET Sandwich Foam Structures under Impact Loading at Normal and Oblique Angles

This section considers the perforation behaviour of the PET (T92.100 and T92.130) sandwich panels under both quasi-static as well as impact loading up to 40 J using three different inclination angles; these being 0°, 10° and 20°. Typical load-displacement traces for both types of loading conditions are shown and the

corresponding perforation energies, based on the area under the plots, are calculated. Correlations are made in terms of the fracture pattern for sandwich panels subjected to quasi-static and dynamic loading. Predictions of the top skin failure threshold and the energy absorbed for sandwich panels are also presented with reference to previous work in a similar area of study [6].

4.3.1 Perforation behaviour of PET (T92.100) sandwich foam structures

Examples of load-time traces following a 40 J impact tests on the PET (T92.100) sandwich structures, at 0°, 10° and 20° inclination angles, are given in Figure 4.92. In general, unlike the case for impact up to 20 J, here, the plots maybe divided into three main regions; the first peak (1), which is associated with failure or fracture of the top skin/skin, the second peak (3), which is associated with the failure of the lower skin, and the region in between the two peaks (2), which indicates the average force of the sandwich structures. Clearly, the normal impact response exhibits a much higher force in comparison to that of the non-normal impact cases.

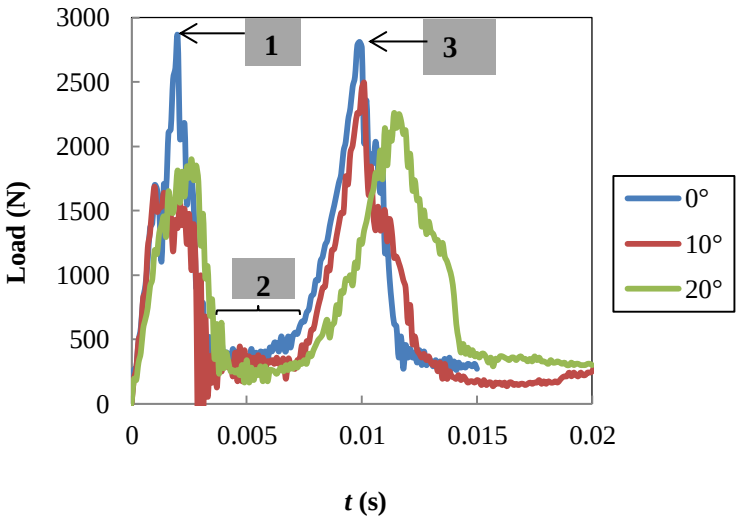

Figure 4.92 Typical load-time traces following dynamic perforation test (impact test) on the PET (T92.100) sandwich structures with 0° and 20° inclination angles.

In addition to the response following impact testing, quasi-static perforation tests have also been conducted to assess the correlation between both types of loading conditions, subjected to the three inclination angles. For example, Figure 4.93 to Figure 4.95 give typical load-displacement traces following quasi-static perforation tests and impact loading on the PET T92.100 sandwich panels at 0°, 10° and 20° inclination angles.

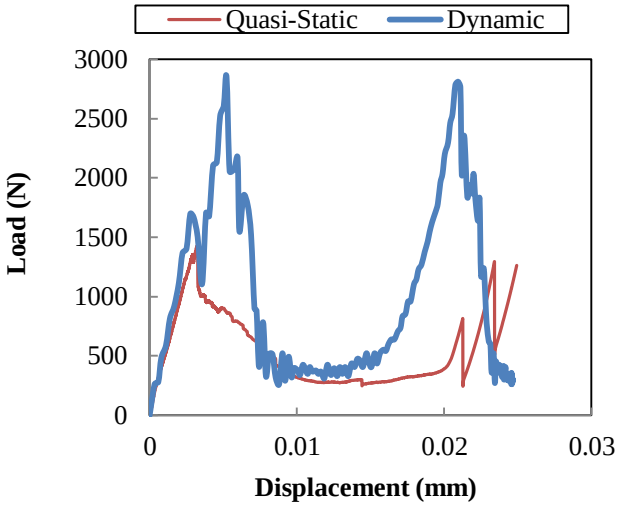

Figure 4.93 Load-displacement traces following quasi-static and impact loading on the PET (T92.100) sandwich structures at a normal impact angle.

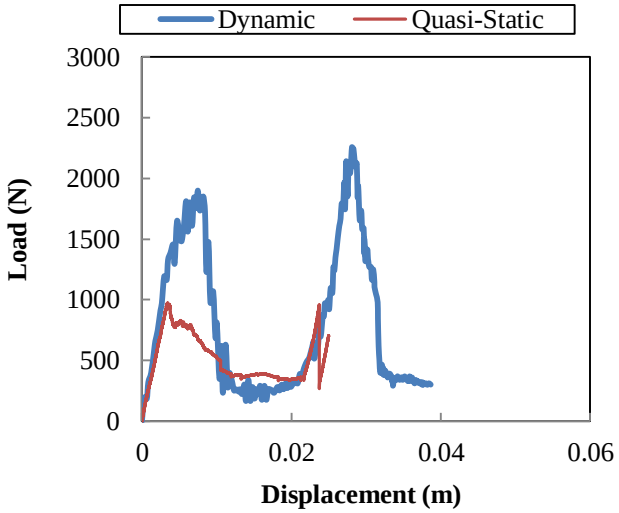

Figure 4.94 Load-displacement traces following quasi-static and impact loading on the PET (T92.100) sandwich structures at a 10° impact angle.

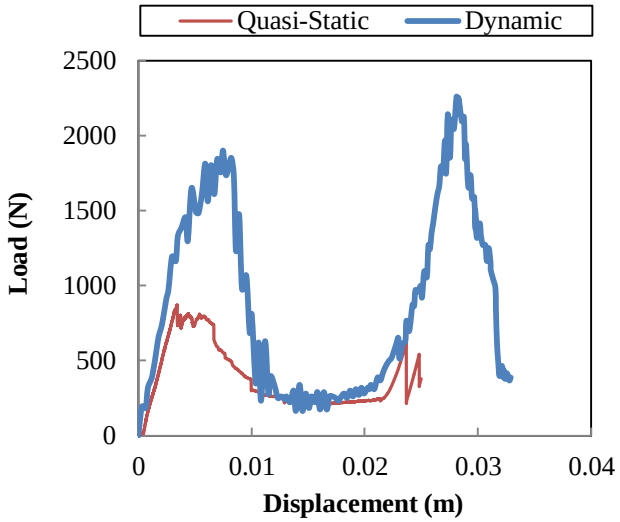

Figure 4.95 Load-displacement traces following quasi-static and impact loading on the PET (T92.100) sandwich structures at a 20° impact angle.

Under both types of loading condition, similar trends are observed, consisting of three main regions. The first region exhibits an initial peak, which corresponds to fracture of the top skin. Following this, in the second region, the load gradually drops and remains constant, which corresponds to the point where the indenter is perforating the foam core. This force is greatly dependent on the fracture properties of the core [12, 13]. Lastly, the third region is a final peak, which is associated with failure of the lower composite skin [12].

From the load-displacement traces, it is apparent that the dynamic load required to cause a given deflection was higher than the load required to cause the same deformation under quasi-static loading, regardless of whether the test was conducted at normal, as shown in Figure 4.93, or at oblique angles, as given in Figure 4.94 and Figure 4.95. Here, 0° loading resulted in a higher initial first peak force, a higher average force as well as a higher second peak force. These observations are

attributed to inertial effects and the material's strain- rate sensitivity [15], as given in Table 4.12.

Table 4.12 Comparison between the results following quasi-static and impact loading on PET (T92.100) sandwich structures at normal and oblique angles.

Type of Loading	**Impact angle (°)**	**1st Peak (N)**	**2nd Peak (N)**	**Average Force (N)**	**Perforation Energy (J)**	**Dynamic enhancement factor, Φ**
Quasi-Static	0°	1425 ± 29	1296 ± 45	302±9	13.7±0.2	1.8
Dynamic		2850±114	2811±141	372±7	25.2±3	
Quasi-Static	10°	1110±28	1128 ± 39	311±6	15.5±0.4	2.15
Dynamic		1687±59	2492 ± 63	337 ±6	33.3±1.4	
Quasi-Static	20°	972±21	958 ± 41	456±16	12.7±0.6	2.4
Dynamic		1812±72	2249±108	298±6	28.8±2.4	

Similarly, the perforation energies under impact loading are higher than the quasi-static values for all the inclination angles considered. In addition, it has been observed that the perforation energy increases with inclination angle, which is in agreement with the work by Zhou *et al.* [16].

Referring to an earlier study by Wen *et al.* [17], the *dynamic enhancement factor, Φ,* which is "*defined as the ratio of the dynamic perforation energy for a panel to the energy absorbed up the fracture of the lower skin of an identical panel under quasi-static loading",* has been considered. This parameter is shown to increase with inclination angle, as listed in Table 4.12.

Figure 4.96 presents the cross-sections resulting following a series of quasi-static tests on PET (T92.100) foam core sandwich panels supported at inclination angles of 0°, 10° and 20°. As shown in Figure 4.96 (a), it is evident that the panel loaded quasi-statically at 0° exhibited both a cylindrical shear zone in the foam core and a

tensile cone crack in the top skin. Interestingly, up to a displacement of 25 mm, the indenter did not fully perforate the panel under static loading. In Figure 4.96 (b), at 10°, it is apparent that the penetrating surface is larger with the shape now being more elliptical and finally at 20°, evidence of significant rear surface damage is apparent, as shown in Figure 4.96 (c).

Figure 4.97 shows the cross-sections following impact perforation tests on similar structures. In Figure 4.97 (a), the cross-section of the panel subjected to normal impact is shown. Similar failure patterns relative to the panel loaded quasi-statically are apparent, including tensile failure of the top skin and shearing of the foam core. In addition, the lower skin has undergone full perforation and therefore significant tensile fracture of the lower skin is apparent.

These observations can be quantified using a simple geometric analysis, where the ratio of the surface area of an elliptical oblique cylinder to that of a right cylinder in which the indenter creates an elliptical entrance hole on the top surface of the target, can be expressed by the following expression :-

$$\frac{\sqrt{\frac{1}{2}(r^2 + R^2)}}{r\ \cos(I)} - 1 \qquad 4.2$$

Where *r*: radius of the right cylinder; *R*: long radius of the elliptical oblique cylinder, *I*: angle between the right cylinder and the elliptical oblique cylinder.

(a)

(b)

(c)

Figure 4.96 Optical micrographs showing the cross-sections of the PET (T92.100) sandwich structures following quasi-static loading at inclination angles of (a) 0°; (b) 10° and (c) 20°.

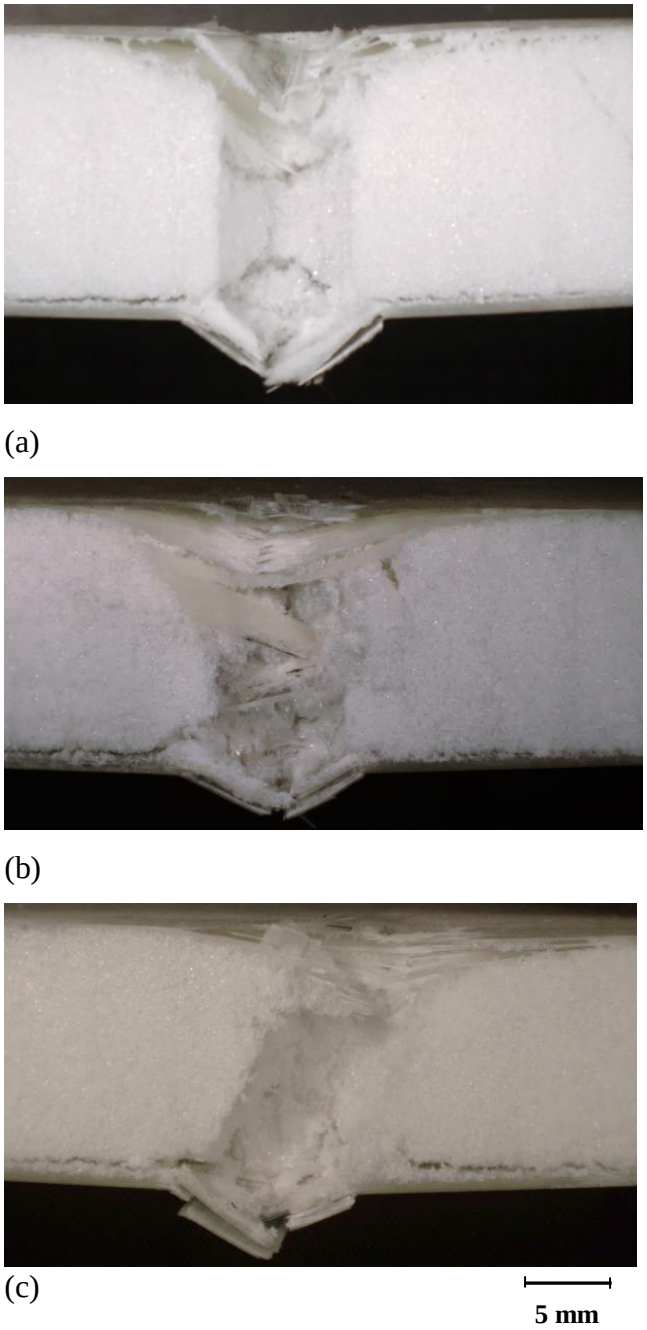

Figure 4.97 Optical micrographs showing the cross-sections of the PET (T92.100) sandwich structures following impact perforation tests (40 J) at inclination angles of (a) 0°; (b) 10° and (c) 20°.

In this work, two cases are considered i.e. inclination angles of 10° and 20° relative to the normal (θ: 0°). Therefore, considering that *r* is 6 mm, *R* is taken as *r cos* (θ), the ratio of the surface area of an elliptic oblique cylinder to that of the right cylinder is given in Table 4.13.

Table 4.13 The percentage increase in surface area and volume of an elliptical oblique cylinder relative to that of a right cylinder using a simple geometric analysis [10].

I	10°	20°
r	6 mm	6 mm
R	r cos (10°)	r cos (20°)
Surface area increase in percentage (%)	1.54	6.42
Volume increase in percentage (%)	2.33	9.89

Similarly, the ratio of the volume of an elliptical oblique cylinder to that of a right cylinder can also be quantified using the following expression:-

$$\frac{1}{\cos(I)} - 1 \qquad 4.3$$

Using this approach, these two important parameters have been calculated and are presented in Table 4.13. It is apparent that with an increase in inclination angle, larger surface area is created during perforation of the sandwich panels. For the case of 10°, there is an increase of 1.54 % in terms of the surface area and 2.33 % in the volume. For the case of 20° loading, the increase in surface area is 6.42 % and 9.89 % by volume. These observations further explain the reasons for the increase in the perforation energy, in passing from a normal impact to an oblique angle of 20°, as previously discussed.

4.3.2 Perforation behaviour of the PET (T92.130) sandwich foam structures

A similar approach to that of the lower density PET (T92.100) sandwich structures are adopted to assess the perforation behaviour of the PET (T92.130) sandwich

structures, for impacts up to approximately 40 J. Again, in addition to the dynamic perforation, the quasi-static response at the three inclination angles is considered.

Typical load-time traces following dynamic perforation tests on the PET (T92.130) sandwich structures at 0°, 10° and 20° inclination angles are presented in Figure 4.98.

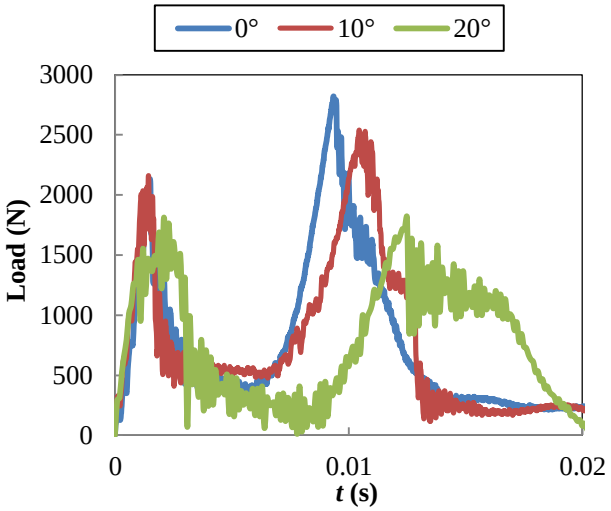

Figure 4.98 Typical load-time traces following dynamic perforation (impact at 40 J) on the PET (T92.130) sandwich structures.

In general, the normal impact response exhibits the highest force magnitude in comparison to the other inclination angles. In addition, similar to the case for the PET (T92.100) sandwich structures, three regions are also apparent, these being a first peak force, an average peak force and a second peak. The values of these three parameters are listed in Table 4.14.

Table 4.14 Comparison of the results following quasi-static and impact tests on the PET (T92.130) sandwich structures at normal and oblique angles.

Type of Loading	**Impact angle (°)**	**1st Peak (N)**	**2nd Peak (N)**	**Average Force (N)**	**Perforation Energy (J)**	**Dynamic enhancement factor, Φ**
Quasi-Static	0°	1530± 31	1443± 50	408±12	16.1±0.2	1.95
Dynamic		2133 ± 107	2821 ± 127	481 ± 10	31.4±1.0	
Quasi-Static	10°	1192 ± 30	1805 ± 62	414 ± 21	16.5±0.4	2.27
Dynamic		2162 ± 112	2540 ± 135	457 ± 18	37.5±0.4	
Quasi-Static	20°	1112 ± 24	1573 ± 67	523 ± 18	19.6±0.7	1.82
Dynamic		2065 ± 74	1890 ± 87	314 ± 8	35.8±1.1	

In Figure 4.99 (a), load-displacement traces following both quasi-static and impact loading at a normal angle are presented, whereas the results for 10° impact are given in Figure 4.99 (b). From the dynamic test, it is apparent that following both 0° and 10° loading, the initial peak forces are lower than the second peak. In addition, impact loading results in a greater impact force than at quasi-static rates.

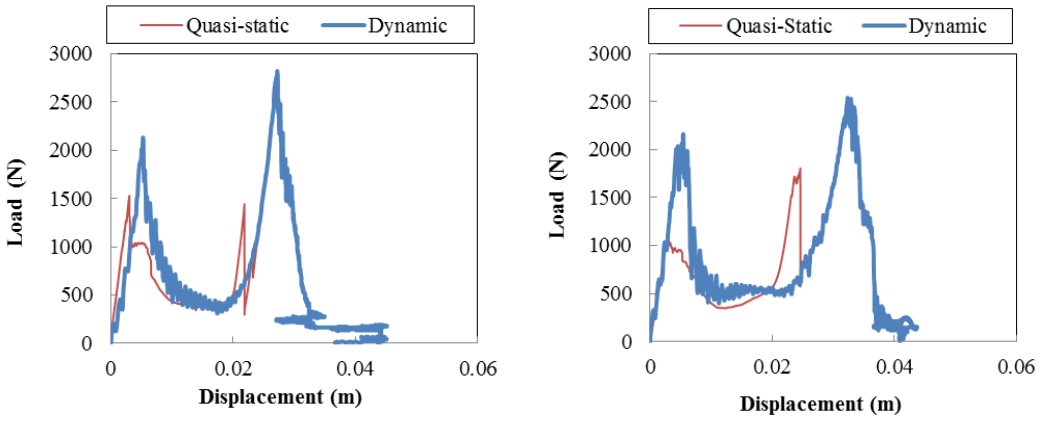

(a) (b)

Figure 4.99 (a) Load-displacement traces following quasi-static and impact loading on the PET (T92.130) sandwich structures at a normal angle, (b) Load-displacement traces following quasi-static and impact loading on the PET (T92.130) sandwich structures at 10°.

At 20°, as given in Figure 4.100, it is evident that the load-displacement traces following dynamic and quasi-static loading are similar, with the latter showing a lower contact force in terms of both the initial peak force and the second peak force. Interestingly, the valley between the two peaks, which is associated with perforation of the foam, indicates that quasi-static loading yields a higher value. This may be due to greater amounts of damage being suffered in the panel subjected to impact loading, particularly in terms of the failure of the core at this impact energy.

As shown in Table 4.14, the perforation energy increases with inclination angle, regardless of whether the panel was loaded quasi-statically or dynamically. In terms of the dynamic enhancement factor, i.e. the ratio between the perforation energy associated with dynamic loading to the value obtained quasi-statically, there was an increase in passing from 0° to 10°. Interestingly, the value is lowest for the 20° case.

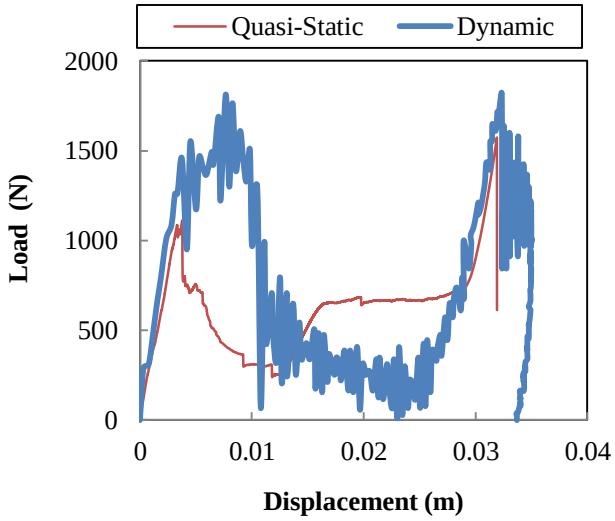

Figure 4.100 Load-displacement traces following quasi-static and impact loading on the PET (T92.130) sandwich structures at 20°.

Figure 4.101 and Figure 4.102 show load-displacement traces following quasi-static tests on the PET (T92.100) and the PET (T92.130) core sandwich panels subjected to

0°, 10° and 20° inclination angles. Here, it is evident that the normal impact resulted in the highest value of the contact force, followed by the 10° case and lastly the 20° event.

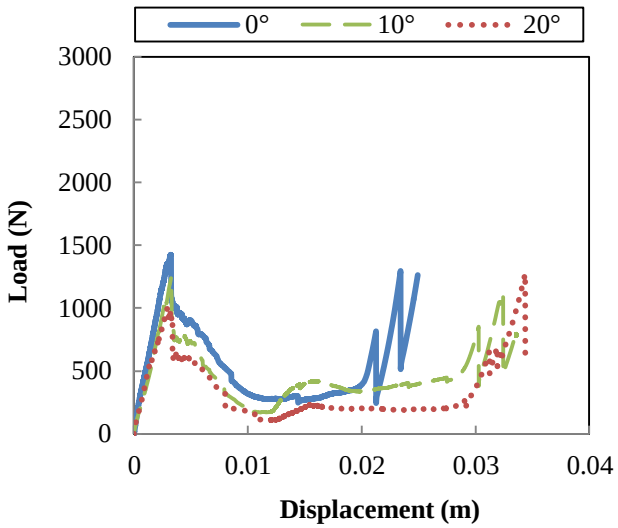

Figure 4.101 Load-displacement traces following quasi-static perforation on the PET (T92.100) sandwich panels tested at 0°, 10°, and 20° inclination angles.

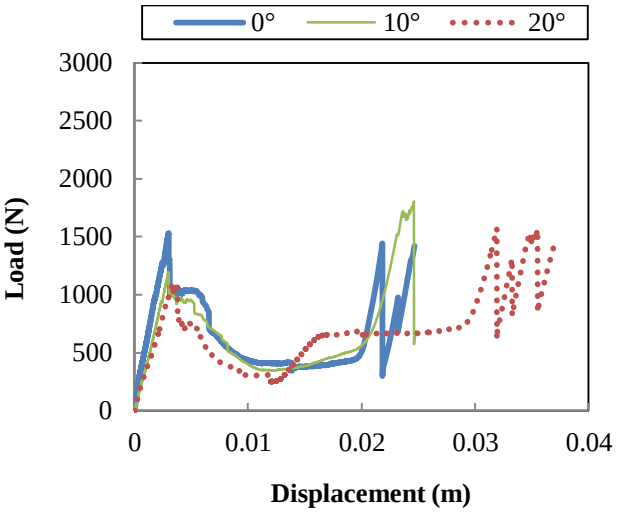

Figure 4.102 Load-displacement traces following quasi-static perforation on the PET (T92.130) sandwich panels tested to 0°, 10°, and 20° inclination angles.

Cross-sections of the PET (T92.130) foam core sandwich panels following quasi-static loading are given in Figure 4.103. Here, as evident in Figure 4.103 (a), the

panel suffered both top skin failure, as well as core failure, taking the shape of the hemispherical indenter, as well as shear failure in the core close to the lower skin.

In Figure 4.103 (b), top skin failures as well as core shear failure and rupture are evident, with the foam core suffering greater amounts of rupture in this case. Finally, quasi-static loading at 20°, Figure 4.103 (c), resulted in both top skin and core shear failure, with the fracture being in the form of an ellipse, as predicted by an FEM model in an earlier study on similar structures [16].

Cross-sections of panels following impact loading are presented in Figure 4.104. In Figure 4.104 (a), it is apparent that the panel suffered both top skin failure, core rupture as well as lower skin failure in the form of a cylinder.

For the case of 10° impact, similar failure modes are observed, with the entrance hole taking the form of an elliptic cylinder, as shown in Figure 4.104 (b). Finally at 20°, significant perforation damage is evident in the image shown in Figure 4.104 (c). Damage in the form of core shear rupture, taking the shape of an oblique elliptical cylinder, as described earlier [16].

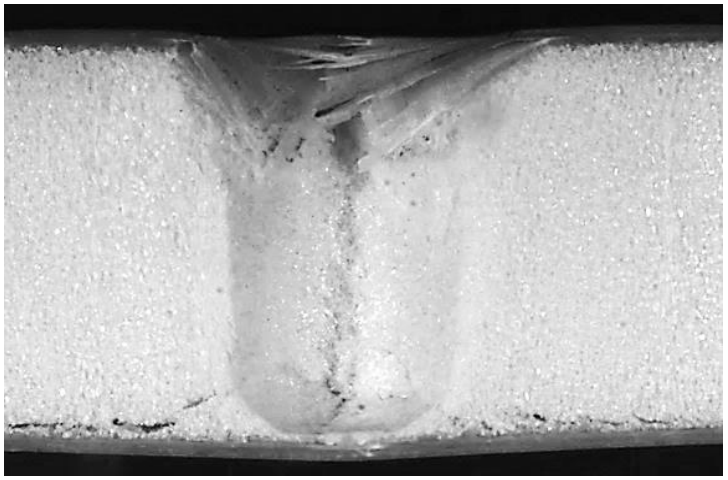

(a)

(b)

(c)

Figure 4.103 Optical micrographs showing cross-sections of the PET (T92.130) sandwich structures following quasi-static loading tested at (a) 0°; (b) 10° and (c) 20° inclination angles.

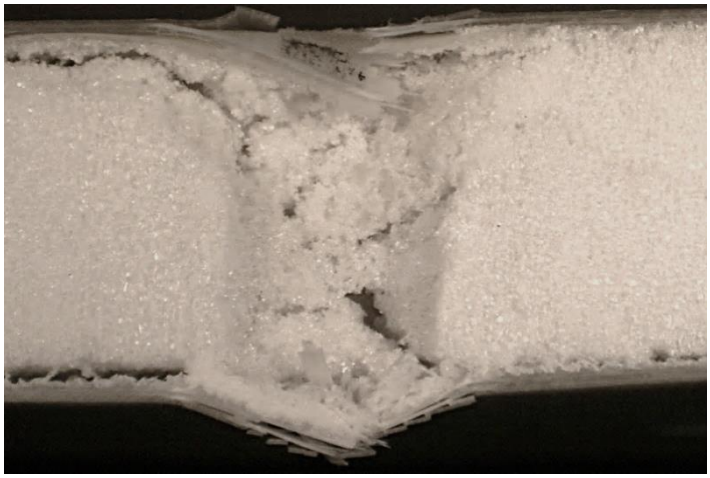

(a)

(b)

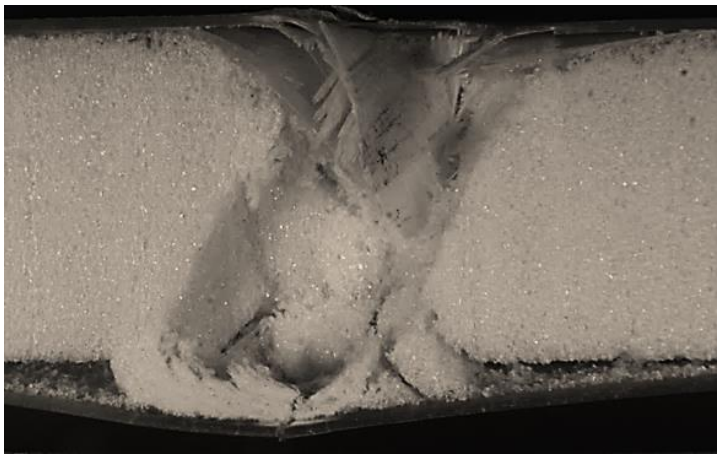

(c)

Figure 4.104 Optical micrographs showing cross-sections of the PET (T92.130) sandwich structures following impact tested at 0°, 10° and 20° of inclination angles.

Figure 4.105 and Figure 4.106 present the perforation energy as a function of impact angle following both quasi-static and impact loading on both types of PET core sandwich panel. Here, it is apparent that the higher density foam core sandwich panels exhibit greater perforation energy at each inclination/impact angle. In addition, there is an increase in the perforation energy in passing from 0° to 10° inclination, for both types of the foam core sandwich panel. Interestingly, the values showed a reduction when passing from 10° to 20°, under both loading conditions.

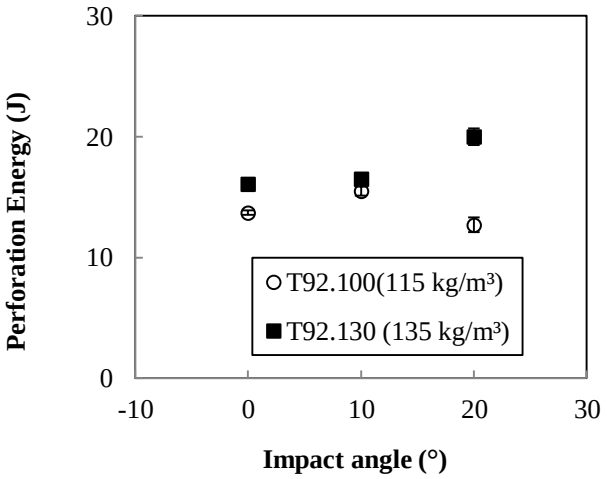

Figure 4.105 Perforation energy vs inclination angle following quasi-static loading on the PET (T92.100 and T92.130) sandwich panels.

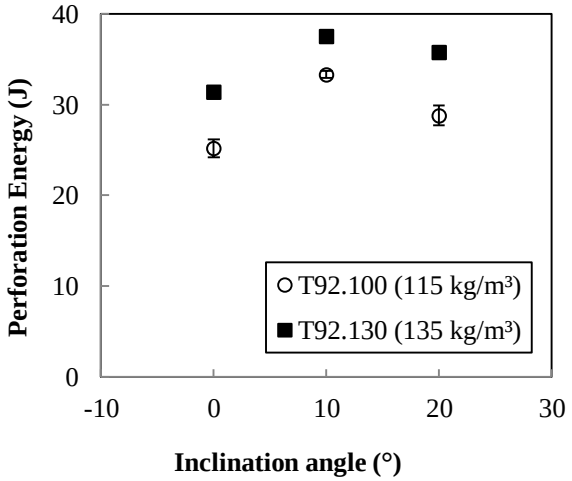

Figure 4.106 Perforation energy vs. inclination angle following impact loading on the PET (T92.100 and T92.130) sandwich panels.

4.4 Summary

The results and discussion on the normal and oblique impact response of the laminated composites and sandwich structures considered in the study have been presented in three sections. In summary, the main results are as listed in Tables 4.15 to 4.22, with an emphasis on the effect of obliquity. Additional information about the effect of core density is also included for the sandwich structures.

i. Contact properties

Tables 4.15 and 4.16 present the results obtained for the contact stiffness, *C*, and indentation exponent, *n*, for sandwich structures with different foam core densities subjected to normal and oblique impact at inclination angles of 0°, 10° and 20°, respectively. The contact parameters, i.e. contact stiffness, *C*, and indentation exponent, *n*, of the composite structures (GFRP laminate) sandwich structures decrease in passing from 0° to 20°. This shows that the effect of obliquity is significant when considering the contact parameters for the sandwich structures.

In addition, referring to Table 4.15, clearly, the contact stiffness for the sandwich structures are dominated by the foam core densities, showing an increase with the increase in foam core density, regardless of whether the test was conducted at 0° or at oblique angles. However, this trend may slightly vary, depending on the type of foam core, i.e. linear PVC (ductile) or PET based-foam core (brittle) since they behave differently. Moreover, from Table 4.16, it appears that there is no clear trend of the effect of core density on the indentation exponent, *n*.

Table 4.15 Contact stiffness, *C*, for the composites and sandwich structures following static indentation tests at different inclination angles.

Material system	**Foam core density (kg/m^3)**	**Contact stiffness, C x10^6 (N/mm^n)**
8-ply GFRP Laminate	-	0° : 22.9 ± 0.15 10°: 7.59 ± 0.10 20°: 0.75 ± 0.05
Linear PVC (R63.140)	140	0° :1.00 ± 0.10 10°: 0.83 ± 0.04 20°: 0.33 ± 0.04
PET (T92.130)	135	0° :0.81 ± 0.05 10°: 0.79 ± 0.08 20°: 0.46 ± 0.10
PET (T92.100)	105	0° :0.45 ± 0.06 10°: 0.26 ± 0.05 20°: 0.26 ± 0.05
Linear PVC (R63.80)	90	0° : 0.49 ± 0.03 10°: 0.37 ± 0.02 20°: 0.21 ± 0.01

Table 4.16 Indentation exponent, *n*, of the composites and sandwich structures following static indentation tests at different inclination angles.

Material system	**Foam core density (kg/m^3)**	**Indentation exponent**, *n*
8-ply GFRP Laminate	-	0° : 1.18 ± 0.05 10°: 1.15 ± 0.05 20°: 1.08 ± 0.02
Linear PVC (R63.140)	140	0° : 1.03 ± 0.05 10°: 1.01 ± 0.03 20°: 1.00 ± 0.02
PET (T92.130)	135	0° : 1.04 ± 0.05 10°: 0.92 ± 0.03 20°: 0.92 ± 0.02
PET (T92.100)	105	0° : 1.00 ± 0.05 10°: 0.92 ± 0.03 20°: 0.92 ± 0.02
Linear PVC (R63.80)	90	0° : 1.01 ± 0.05 10°: 1.00 ± 0.03 20°: 0.97 ± 0.02

ii. Maximum impact force, P_{max}, and the corresponding normal force, F_N.

The maximum impact forces and the corresponding normal forces following normal and oblique impact on the laminated composites and sandwich structures are listed in Table 4.17. It is apparent that the laminated composites exhibit the highest value of the maximum impact force, which is almost double those for the sandwich structures, with the highest core density (linear PVC R63.140 sandwich structures).

Also, it can be seen from Table 4.17 that changing the inclination angle produces a similar trend to that obtained for the contact parameters, i.e. increasing the

inclination angle results in a decrease in the maximum impact force, P_{max}, and the corresponding normal force, F_N.

In addition, the effect of core density on the impact response of both types of sandwich structures (linear PVC and PET sandwich structures) is clear, regardless of whether the test was conducted at normal angle (0°) or an inclined angle. The highest density core sandwich structures show the highest value of the maximum impact force, at each of the inclination angle. Clearly, this suggests that the effect of core density is the dominant factor for impact up to 20 J.

Table 4.17 P_{max} and the corresponding F_N of the composite and sandwich structures following normal and oblique impact with varying foam core densities.

Material system	**Foam core density (kg/m^3)**	P_{max} **(N)**	F_N **(N)**
8-ply GFRP Laminate	-	0° : 5521 ± 552 10°: 5000 ± 500 20°: 3560 ± 326	5521 4822 3416
Linear PVC (R63.140)	140	0° : 2998 ±201 10°: 2774 ± 189 20°: 2312 ± 162	2998 2675 2218
PET (T92.130)	135	0° :2866 ± 263 10°:2361 ± 196 20°: 1923 ± 246	2597 2029 1845
PET (T92.100)	105	0° : 2462 ± 187 10°: 2908 ± 194 20°: 2249 ± 224	2462 2805 2158
Linear PVC (R63.80)	90	0° : 2221 ± 160 10°: 2063 ± 140 20°: 2030 ± 180	2221 1990 1948

iii. Energy-balance model

An energy-balance model has been successfully applied to predict the impact response of the laminated composites and sandwich structures, following impact at both normal and non-normal angles. The results are given in Table 4.18. The maximum impact force, P_{max}, is obtained at different energy level for the normal and oblique impact cases. For the monolithic laminate, it can be seen that the energy-balance model, over-predicts the experimental results. The difference varies from 7% to 14% for the normal impact case and 8% to 44 % for the oblique impact cases. This suggests that the model agrees well with the normal impact results.

For the sandwich structures, the energy-balance model predictions are in good agreement with the experimental results up to the threshold energy level. The difference ranges between ± 13%. Whereas, at the maximum energy level, it can be seen that the energy-balance model prediction overestimates the experimental values for all the structures considered. The difference ranges from 5% to 52%.

Table 4.18 Summary of main experimental and predicted results using an energy-balance model following normal and oblique impact on composite structures.(Note: Values in parenthesis are ratio between the predicted against the experimental P_{max})

Material system	Impact energy (J)	Experimental P_{max} (N)			Predicted P_{max} (N)		
		0°	10°	20°	0°	10°	20°
8-ply GFRP laminate	8.5	2982±239	3109±250	2208±52	3256 (1.09)	3522 (1.13)	2382 (1.08)
	14	4379±347	3579±284	2620±111	4598 (1.07)	4997 (1.40)	3221 (1.23)
	20	5129±390	4667±354	2758±251	5878 (1.14)	6389 (1.37)	3976 (1.44)
Linear PVC (R63.140) sandwich structures	5	2220±138	1983±59	1062±101	1988 (0.90)	1723 (0.87)	1100 (1.04)
	10	2762±135	2742±101	1662±121	2800 (1.01)	2439 (0.89)	1560 (0.94)
	20	2705±195	2774±189	2100±168	3945 (1.46)	3452 (1.24)	2213 (1.05)
PET (T92.130) sandwich structures	5	1944±156	2010±71	1088±133	1911 (0.98)	1799 (0.90)	1403 (1.29)
	10	2714±189	2260±100	1516±223	2701 (1.0)	2543 (1.13)	1980 (1.31)
	20	2866±263	2361±196	1923±246	3818 (1.33)	3597 (1.52)	2792 (1.45)
PET (T92.100) sandwich structures	5	1987±139	1629±49	1212±148	1841 (0.93)	1580 (0.97)	1118 (0.92)
	10	2414±164	2084±92	1571±201	2604 (1.08)	2233 (1.07)	1580 (1.01)
	20	2462±187	2908±194	2249±224	3683 (1.50)	3156 (1.09)	2234 (0.99)
Linear PVC (R63.80) sandwich	5	1298±80	1313±40	1087±110	1464 (1.13)	1359 (1.04)	1123 (1.03)
	10	1931±95	1313±40	1087±110	1464 (1.13)	1359 (1.04)	1123 (1.03)
	20	2221±160	2063±140	2030±180	2930 (1.32)	2718 (1.32)	2234 (1.10)

iv. Damage characteristics and absorbed energy

Overall, for the 8-ply GFRP laminate, for impact at energies up to 28 J (maximum impact energy), damage on the rear surface took the form of a peanut-like shape for both 0° and 10° inclination angles. In addition, evidence of matrix cracking and fibre

fracture are apparent at the cross-sections of the panels subjected to both 0° and 10°, whereas for the panels subjected to 20° impact exhibit only barely visible damage in the form of localized delamination.

A similar trend has been observed in the lower density linear PVC (R63.80) sandwich structures, where evidence of a similar form of damage on upper skin was obtained from visual observations of the impact surface. In addition, evidence of core shear rupture following a 20 J impact (maximum impact energy) was observed in the panels subjected to normal and 10° impact, whereas the 20° panel remain intact up to these energy levels. However, other types of foam-based sandwich structures having much higher core density, consisting of the linear PVC (R63.140) sandwich structures, the PET (T92.130) sandwich structures and the lower density PET (T92.100) having nominal densities of 140, 135 and 105 respectively suffered greater damage, at energies up to 20 J. Evidence of both top skin failure in the form of matrix cracking and fibre fracture as well as core shear rupture are apparent from visual observations as well as cross-sectional analysis of the panels, regardless of whether the panel was subjected to normal or oblique angles. The corresponding maximum depth of permanent indentation at each inclination angle is given in column 5 of Table 4.19.

It is a general belief that increasing the inclination angle results in a decrease in damage area for monolithic composite laminate, whilst the absorbed energy increases with increasing inclination angle [1-4]. Results from the present work as presented in column 3 and 4 of Table 4.19 indicates that this is true for laminated composites and the lower density linear PVC (R63.80) foam core sandwich

structures. Although this is not generally true for sandwich structures with higher density foam core i.e. linear PVC (R63.140), PET (T92.130) and PET (T92.100).

As an example, referring to Table 4.19, it is apparent that for the laminated composites and the linear PVC (R63.80) sandwich structures, at the maximum impact energies of 28 J and 20 J, the damage area reduced with inclination angle, in passing from 0° to 20°. In addition, the absorbed energy increases with increasing inclination angle. These findings suggest the effect of obliquity on the damage progression and the absorbed energy for the monolithic composites and the lower density sandwich structures.

However, for other types of sandwich structures, consisting of the linear PVC (R63.140), PET (T92.130) and the PET (T92.100) sandwich structures with much higher nominal densities of 140 kg/m^3, 135 kg/m^3 and 105 kg/m^3 respectively, the trend is not absolutely in agreement with those available in the open literature. For these structures, it appears that the maximum damage area always occurs at 10° and the less onerous damage always occur at 20°. This suggests the combination effect of tensile, compression and shear for impact at 10° in comparison to pure shearing for the 20° impact case. Interestingly, the absorbed energy reduces with increase in inclination angle for these types of structures.

Table 4.19 Comparisons of the damage areas and the corresponding absorbed energy and the max. depth of permanent indentation following normal and oblique impact on laminated composites and sandwich structures at the threshold energy (14 J and 10 J) as well as maximum impact energy (28 J and 20 J).

Material system	Inclination angle	Up to maximum impact energy		
		Damage Area (mm^2)	Absorbed Energy (J)	Max. depth of permanent indentation (mm)
GFRP Laminate	0°	816 ± 62	17.5 ± 2.4	1.69 ± 0.01
	10°	776 ± 90	20.9±3.5	1.43 ± 0.13
	20°	314 ±25	24.6±2.1	0.1 ± 0.0
Linear PVC (R63.140) sandwich structures	0°	420 ± 2	16.7±0.1	4.2 ± 0.0
	10°	496 ± 6	16.1 ± 1.5	3.9 ± 0.0
	20°	340 ± 3	12.4 ± 0.4	3.8 ± 0.0
PET (T92.130) sandwich structures	0°	484 ± 1	18.7 ± 0.2	5.76 ± 0.02
	10°	603 ± 8	17.2 ± 0.0	6.5 ± 0.1
	20°	369 ± 0	14.2 ±0.3	2.2 ±0.0
PET (T92.100) sandwich structures	0°	327 ± 3	15.9 ± 0.1	5.8 ± 0.1
	10°	348 ± 1	13.0 ± 0.0	6.5 ± 0.0
	20°	301 ± 2	13.3 ± 0.1	2.2 ± 0.0
Linear PVC (R63.80) sandwich structures	0°	760 ± 4	8.5 ± 0.1	4.0 ± 0.02
	10°	504 ± 45	11.5 ± 0.6	3.40 ± 0.3
	20°	316 ± 18	11.8 ± 1.1	0.53 ±0.0

v. Perforation behaviour of the sandwich structures subjected to quasi-static and dynamic loading at normal and oblique angles.

The main results following quasi-static perforation tests are given in Table 4.20, for both types of the PET (T92) sandwich structures; these being the first peak, the second peak and the average force as well as the corresponding perforation energy.

The first peak, which is associated with failure of the top skin, reduced with increase in inclination angle, in passing from 0° to 20°. Similar trends are observed for the second peak which is associated with the failure of the lower skin. However, in terms of the average force, which corresponds to densification of the foam core, the value

show an increase with inclination angle, for both types of PET-based sandwich structures.

Under dynamic loading, as given in Table 4.21, that is when subjected to impact at 40 J, similar trends to those of the quasi-static perforation results are evident , where it has been observed that both the first and the second peak reduced with increasing inclination angle, in passing from 0° to 20°. However, in terms of the average force, when compared to the results from the quasi-static test, it is seen that these values reduced in passing from 0° to 20° inclination angle.

Table 4.20 Comparison of results following quasi-static perforation tests on the PET sandwich structures at normal and oblique angles.

Type of foam core sandwich structures	**Impact angle (°)**	**1st Peak (N)**	**2nd Peak (N)**	**Average Force (N)**
T92.130	0	1530 ± 31	1443± 50	408 ±12
	10	1192 ± 30	1805 ± 62	414 ± 21
	20	1112 ± 24	1573 ± 67	523 ± 18
T92.100	0	1425 ± 29	1296 ± 45	302 ± 9
	10	1110 ± 28	1128 ± 39	311 ± 6
	20	972 ± 21	958 ± 41	456 ± 16

Table 4.21 Comparison of the results following dynamic perforation tests on the PET sandwich structures at normal and oblique angles.

Type of foam core sandwich structures	**Impact angle (°)**	**1st Peak (N)**	**2nd Peak (N)**	**Average Force (N)**

T92.130	0	2133 ± 107	2821 ± 127	481 ± 10
	10	2162 ± 112	2540 ± 135	665 ± 18
	20	2065 ± 74	1890 ± 87	314 ± 8
T92.100	0	2850 ± 114	2811 ± 141	372 ± 7
	10	1687 ± 59	2492 ± 63	337 ± 6
	20	1812 ± 72	2249 ± 108	298 ± 6

In addition, regardless of whether the test was conducted at normal or other inclination angles, the maximum force magnitude increases significantly, as summarised in Table 4.22, under dynamic loading in comparison to quasi-static test. Again, these findings highlight the effect of strain-rate on sandwich structures having glass-fibre reinforced epoxy as the skin materials. Indeed, it has been reported previously that such materials are strain-rate sensitive [16].

Table 4.22 Comparison of the ratio between the dynamic and quasi-static results following perforation tests on the PET-based sandwich structures.

Type of foam core sandwich structures	**Impact angle (°)**	**1st peak**	**2nd peak**
		Ratio between dynamic and quasi-static loading	**Ratio between dynamic and quasi-static loading**
T92.130	0	1.4	2.0
	10	1.8	1.4
	20	1.9	1.2
T92.100	0	2.0	1.8
	10	1.0	1.0
	20	2.0	2.4

Moreover, further examinations of the cross-sections of the sandwich structures and the predicted results using a simple geometric analysis, have demonstrated that perforation at oblique angles allow more materials to be perforated i.e. the volume

and surface area increased by approximately 2.3% and 1.5% when subjected to 10° of inclination angle compared to that of the normal angle. In addition, at higher inclination angle of 20°, the increased in volume and surface area is close to 9.9 % and 6.4%, respectively.

4.5 References

[1] Madjidi, S., Arnold, W. S., & Marshall, I. H. (1996). Damage tolerance of CSM laminate subject to low velocity oblique impacts. Composite structures, 34(1), 101-116.

[2] Ghaffari, S., Tan, T. M., & Awerbuch, J. (1990, November). An experimental and analytical investigation on the oblique impact of graphite/epoxy laminate. In 22nd International SAMPE Technical Conference, November.

[3] Bouadi, H., Marple Jr, L. R., & Marshall, A. P. (1992). Normal and oblique impact damage on thick-section composite laminate. Recent Advances in the Structural Dynamic Modelling of Composite Rotor Blades and Thick Composites. ASME, 30, 157-169.

[4] Hazell, P. J., Appleby-Thomas, G. J., & Kister, G. (2010). Impact, penetration, and perforation of a bonded carbon-fibre-reinforced plastic composite panel by a high-velocity steel sphere: an experimental study. The Journal of Strain Analysis for Engineering Design, 45(6), 439-450.

[5] Sutherland, L. S., & Soares, C. G. (2005). Contact indentation of marine composites. Composite structures, 70(3), 287-294.

[6] Akil, H. (2002). The impact response of composite sandwich structures. Liverpool: Thesis Ph.D., 2002.

[7] Hill, R., Storakers, B. and Zdunek, A. (1989). A Theoretical Study of the Brinell Hardness Test. Proceedings of the Royal Society A: Mathematical, Physical and Engineering Sciences, 423(1865), pp.301-330.

[8] Tan, C. Y., & Akil, H. M. (2012). Impact response of fibre metal laminate sandwich composite structure with polypropylene honeycomb core. Composites Part B: Engineering, 43(3), 1433-1438.

[9] Abrate, S. (1991). Impact on laminated composite materials. Applied Mechanics Reviews, 44(4), 155-190.

[10] Foo, C. C., Seah, L. K., & Chai, G. B. (2011). A modified energy-balance model to predict low-velocity impact response for sandwich composites. Composite Structures, 93(5), 1385-1393.

[11] Yang, F. J., & Cantwell, W. J. (2010). Impact damage initiation in composite materials. Composites Science and Technology, 70(2), 336-342.

[12] Lee, L. J., Huang, K. Y., & Fann, Y. J. (1993). Dynamic Responses of Composite Sandwich Plate Impacted by a Rigid Ball*. Journal of Composite Materials, 27(13), 1238-1256.

[13] Hassan, M. Z. (2012). The low velocity impact response of sandwich structures (Doctoral dissertation, The University of Liverpool).

[14] Chai, G. B., & Zhu, S. (2011). A review of low-velocity impact on sandwich structures. Proceedings of the Institution of Mechanical Engineers, Part L: Journal of Materials Design and Applications, 225(4), 207-230.

[15] Hassan, M. Z., & Cantwell, W. J. (2012). The influence of core properties on the perforation resistance of sandwich structures–An experimental study. Composites Part B: Engineering, 43(8), 3231-3238.

[16] Zhou, J., Hassan, M. Z., Guan, Z., & Cantwell, W. J. (2012). The low velocity impact response of foam-based sandwich panels. Composites science and Technology, 72(14), 1781-1790.

[17] Wen, H. M., Reddy, T. Y., Reid, S. R., & Soden, P. D. (1997). Indentation, penetration and perforation of composite laminate and sandwich panels under quasi-static and indenter loading. Key Engineering Materials, 141, 501-552.

CHAPTER V: CONCLUSIONS

This chapter summarises the key contributions of the research work. In addition, suggestions for continuing the work outlined in this study are presented.

5.0 Conclusions

Following this research study, several conclusions can be drawn and these are outlined as follows:-

5.1 Characterization tests

For the composite structures, i.e. the monolithic laminates and the sandwich structures, experimental results revealed that both the inclination angle and the core density have an effect on the contact parameters, such as the contact stiffness, *C*, and the indentation exponent, *n*. As the inclination angle increases, the contact parameter decreases, whereas increasing the core density of the sandwich structures results in increase in the contact stiffness. As an example, the monolithic laminate exhibits the largest reduction in the contact stiffness, i.e. in passing from 0° to 10° there is a 70% reduction as compared to that of the sandwich structures, with reductions in the range of 17 % and 43%.

However, in contrast to the contact stiffness, *C*, when the core density increases, results indicate that the indentation exponent, *n*, decreases with increase in inclination angle. This effect is more apparent for the PET-based sandwich structures, between 0 and 10°. Here, the effect of core density does not show any significant difference for the different types of sandwich structures considered.

5.2 Energy-balance model

Both the experimental and predicted results following normal and oblique impact on the sandwich structures using an energy-balance model are in good agreement up to the threshold energy (i.e. 10 J), for all the cases considered, except for the PET T92.130 and linear PVC (R63.80), both at 20°. It has been established that for both the monolithic laminate and the sandwich structures, the energy balance model is adequate up to the threshold energy where the materials behave elastically. Above this threshold energy, the energy balance model is not sufficient enough to predict the maximum impact force, P_{max}.

5.3 Impact response and damage

This section fulfils the primary aim of this thesis, i.e. the establishment of the effect of obliquity on the impact response of monolithic laminate and sandwich structures for angle ranging from 0° and 20°. It has been established that the monolithic laminates exhibited the highest maximum impact force and normal force, as compared to the sandwich structures. In addition, it is shown that an increase in the inclination angle for both composite types results in a reduction in both the maximum impact force and the normal force. As the inclination angle increases, the percentage reduction in maximum impact force, i.e., from 0° to 10°, the percentage range from 7% to 9%, whereas from 10° to 20°, there is a greater reduction, about 10 to 31%. In addition, it has been shown that for sandwich structures, the higher the core density, the higher the maximum impact force and normal force.

At 20 J, greater levels of damage were observed in the sandwich structures with a higher density foam core (i.e. linear PVC R63.140, PET T92.130 and PET T92.100) in comparison to that of the laminated composites and the lower density linear PVC

(R63.80) sandwich structures; regardless of whether the panels were subjected to normal or oblique angles.

In addition, it has been established from the tests on the monolithic laminates and the linear PVC (R63.80) sandwich structures that the energy absorbed increases with increasing inclination angle and the damage area reduces with inclination angle; whereas for higher foam core density sandwich structures, the 10° impact produces the maximum level of damage, whilst the absorbed energy decreases with increasing inclination angle.

5.4 Perforation behaviour

From the perforation tests on the PET sandwich structures subjected to quasi-static or dynamic loading, it can be deduced that for both loading cases, increasing the inclination angle leads to a reduction in the first and second peak forces. Whereas, the average force increases with increasing inclination angle for quasi-static loading and reduces with increasing inclination angle for dynamic loading.

Also irrespective of the angle of obliquity, the effect of strain rate on the PET sandwich structures (having glass fibre reinforced epoxy as the skin materials) is very significant, as evident in the load-displacement traces following dynamic perforation (impact tests) and the quasi-static perforation tests. Here, it has been observed that the dynamic load required to cause the given deflection was higher than the load required to cause the same deformation under quasi-static loading. In addition, the dynamic enhancement factor, Φ, which is the ratio of the dynamic perforation energy for a panel to the energy absorbed up the fracture of the lower skin of an identical panel under quasi-static loading, also revealed the strain rate effect.

Finally, it can be established that for impact up to intermediate energies (i.e. 20 J) damage is more severe for the normal impact cases. However, at the perforation level (i.e. up to 40 J) clearly it is the oblique impact case that caused greater perforation as compared to the normal impact case.

5.5 Further work

It is well agreed that impact in composites and sandwich problems is a 3D problem. Moreover, oblique impact is of greater complexity. Very limited information has been reported about the low-velocity oblique impact response of composites and sandwich structures, hence, extended work should be carried out both experimentally as well as using numerical models. Some of the key aspects to be considered are briefly pointed out as follows:-

i. Impact angle

Further experimental and numerical work should be conducted at higher impact angles such as 30°, 45° and 60° to provide a more comprehensive investigation for impact at low-velocity range.

ii. Impacter geometry

It has been established that impacter geometry such as impacter shape and diameter such as conical, hemispherical with a variation of impact diameter and mass greatly influence the impact response at normal angle. Therefore, a more detailed knowledge of the effect of varying this key parameter will contribute to a comprehensive understanding of oblique impact behaviour.

iii. Target material

Experimental and numerical work using a wider range of composite materials varying in type, shape, structure etc. subjected to oblique impact will provide better insight about the oblique impact behaviour.

iv. Environmental conditions

Further investigation into the influence of environmental conditions such as in water, and at elevated temperatures will give an insight to the field of impact engineering as well as more closely representing actual impact scenarios and conditions.